# Politecnico di Torino

Corso di Laurea Magistrale in Nanotechnologies for ICTs

Tesi di Laurea Magistrale

# Thermal management of ultraviolet LEDs and VCSELs: computer-aided multiphysics optimization

**Relatore:**
Prof. Michele Goano

**Correlatori:**
Prof. Åsa Haglund
Dott. Alberto Tibaldi
Prof. Francesco Bertazzi
Dott. Pierluigi Debernardi

**Candidato:**
Giulia Cardinali

Anno Accademico 2018/2019

[This page intentionally left blank]

# Abstract

AlGaN alloys have emerged as the most promising semiconductor compounds for deep-ultraviolet (DUV) applications. Indeed, electronic bandgap engineering can be performed by changing the alloy composition, enabling the production of semiconductor light sources covering most of UVA, UVB and UVC spectra. The main interest in pushing the emission wavelength toward such short wavelengths relies on the wide variety of applications ranging from the biomedical field, for dermatological therapy (i.e. psoriasis, vitiligo), to UV curing (mainly UVA and UVB), to plant illumination systems for green-houses (UVB), and water/surface purification and disinfection (UVC and below). The main limitation of a realistic implementation of deep-UV emitting devices relies in the thermal management. Several studies have reported an output power conversion efficiency for blue-VCSELs and UVB-LEDs lower than the 10%, meaning that all the input power that is not converted into optical power is dissipated into heat. Even more challenging is the implementation of UV-emitting vertical-cavity surface-emitting lasers (VCSELs). In fact, the poor refractive index difference and hole transport properties prevents the use of AlGaN distributed Bragg reflectors (DBRs). On the other hand, VCSELs based on dielectric DBRs exhibit mediocre heat conduction properties, leading to dramatic increases of the cavity temperature. In fact, no emission below 340 nm is reported for a VCSEL. Thus, it is straightforward to notice how thermal management is a crucial issue for the development of UV-emitting devices. In this master thesis, the thermal characteristics of UV-emitting thin-film flip-chip LEDs and VCSELs are studied by analysing different device geometries, in order to enhance the thermal dissipation through the structure and study the thermal effects in terms of cavity resonance shifts for the VCSELs, aiming to provide concrete inputs for the optimization of the thermal management of the next generation of deep-UV emitting devices. In the first part of this work the temperature profile and the heat flow in UVB/UVC VCSELs and UV-emitting thin-film flip-chip LEDs is simulated in COMSOL Multiphysics by implementing 2D and 3D steady-state simulations. Different geometries are explored for each device in order to minimize the temperature rise in the active region and improve the heat flow from the active region toward the heat sink. The heat capability of the different devices is then studied by calculating the thermal resistance, used as a figure of merit to compare all the different geometries. The second part of the thesis is aimed at studying the effects of temperature rise in the cavity of a VCSEL in terms of temperature induced resonance wavelength shift. A one-dimensional transfer matrix method is implemented to solve the Helmholtz's equation along the VCSEL optical axis and extract the standing wave pattern. The temperature profile along the optical axis is extracted from the thermal simulation implemented in COMSOL and used to update the refractive index of each layer of the resonator according to the thermo-optic coefficient of the corresponding material. Different VCSEL structures are investigated: UVB and UVC emitting VCSELs with a double dielectric DBR scheme and a blue VCSEL with hybrid DBR configuration. In the latter case, the calculated shift rate is compared to literature values, obtaining great accordance between simulations and measurements.

# *Acknowledgements*

As a conclusion of this long years at Politecnico di Torino, I really think that it is dutiful to mention some of the people that have contribute to this success. During my stay in Göteborg, I had the privilege to work in close contact with a group composed by very talented people that made my international experience constructive either from a human and an academic point of view.
First of all, I am very grateful to Prof. Äsa Haglund for accepting me as a master student in her group at the Chalmers University of Technology and for all the encouragement. I am also very thankful to my co-supervisors at Chalmers, Filip Hjort and Michael Bergmann for the big help with COMSOL and the discussions on the processing techniques of LEDs and VCSELs. Thanks also to Ass. Prof. Johan Gustavvson for its help with the transfer matrix method. Finally, many thanks to Ass. Prof. Jörgen Bengtsonn for all the interesting discussions.

A conclusione di questo lungo percorso al Politecnico di Torino, penso sia doveroso spendere qualche parola di ringraziamento per tutte quelle persone che in un modo o nell'altro hanno contribuito a questo traguardo.
Un grande ringraziamento al mio relatore, il Prof. Michele Goano, e i miei correlatori il Dott. Alberto Tibaldi e il Prof. Francesco Bertazzi per avermi fatto avvicinare al mondo dell'optoelettronica e, soprattutto, per il supporto e la pazienza avuti nei miei confronti durante il lavoro di stesura della tesi. Ringrazio anche il mio correlatore, il Dott. Pierluigi Debernardi, per l'aiuto ricevuto durante il breve periodo di preparazione prima della partenza per Göteborg, periodo che è stato essenziale per una più profonda comprensione dei principi di funzionamento dei VCSEL.

Ai miei genitori, per non aver mai dubitato mai delle mie capacità, spronandomi a dare sempre il meglio. Grazie alle mie sorelle, Alessandra ed Elena, per esserci sempre nonostante la distanza.
Un ringraziamento speciale, infine, a tutti i miei amici per aver reso questi anni di università un po' meno faticosi.

# Contents

# List of Figures

# List of Tables

# 1 | Introduction to III-nitride opto-electronics

Group-III nitride semiconductors and their alloys have been recognized among the most promising materials for opto-electronic devices operating in the short-wavelength region. Thanks to the possibility of tuning the electronic bandgap by varying the composition of the alloys, they are able to cover a wide range of emission wavelengths from the near infrared down to the ultra-violet region of the optical spectrum. There are several characteristics of nitride compounds which make them particularly attractive for photons emitting devices, including Light-Emitting Diodes (LEDs) and Laser Diodes (LDs).

The large difference in electronegativity between nitrogen and the elements of the III group leads to the formation of very strong chemical bondings, which makes the obtained compound highly chemically stable and optimal for harsh environment applications.

The main challenge of heterostructures based on III-nitride materials relies on the lack of lattice-matched substrates. A high density of dislocation defects is present in the epitaxial structure due to the mismatch between the lattice parameters of substrate and epilayers, with a consequent formation of a strained film upon deposition [1]. In non-optimized heterostructures the dislocation density is typically of the order of $10^{10}$cm$^{-2}$. Threading dislocations (TDs) act as acceptor-like levels in which electrons can be trapped, generating an electric field by which holes are attracted recombining with electrons non-radiatively, thus reducing the radiative recombination efficiency and the Internal Quantum Efficiency (IQE) [2]-[3].

Differently from other conventional materials for opto-electronic applications, like silicon or gallium arsenide which crystallize in a zinc-blend diamond-like cubic structure, III-nitride compounds crystallize in their most stable form in a wurzite structure, in which nitrogen atoms are placed at the lattice sites of a hexagonal close packed (HCP) structure and the group-III atoms occupy half of the tetrahedral sites available in the lattice. This wurzite crystal structure is both non-centrosymmetric and polar, leading to the formation of very strong spontaneous and/or piezoelectric-induced polarization fields along the c-axis ($\sim$ 10 MV/cm). In devices with quantum wells (QWs) active regions, the generated polarization fields are large enough to spatially separate electrons and holes toward opposite sides of the QW reducing the overlap between electrons and holes wave functions, with a consequent reduction of the radiative recombination efficiency, photon emission rate and causing a red shift of the photoluminescence peak (quantum confined stark effect) [4]-[6].

Ultraviolet light is the portion of the non-visible light spectrum which comprises wavelengths ranging from 400 nm down to 100 nm. A further classification is based on the interaction of the light with the biological environment and its transmittance through the atmosphere: UVA (400-320 nm) in non-germicidal and is partly transmitted through the atmosphere, UVB (320-280 nm) is germicidal, irritant to human skin and it is mostly absorbed by the atmosphere, while UVC (280-200 nm) is absorbed, strongly germicidal and ozone producing. The last class comprises the VUV (Vacuum UV, 200-100 nm) which is highly attenuated in air and can be used only in vacuum conditions.

AlGaN alloys have emerged as the most promising semiconductor compounds for deep-ultraviolet (DUV) applications. Indeed, electronic bandgap engineering can be performed by changing the alloy composition, enabling the production of semiconductor light sources covering most of UVA, UVB and UVC spectra ($\sim$ 200-363 nm) [7]. The main interest in pushing the emission wavelength toward such short wavelengths is motivated by the large variety of applications of ultraviolet-emitting devices ranging from the biomedical field, for dermatological therapy (i.e. psoriasis, vitiligo, cutaneous T-cell lymphoma), to UV curing for their high efficiency in catalyzing chemical reactions (mainly UVA and UVB), to plant illumination systems for greenhouses (UVB), and water/surface purification and disinfection (UVC and below) exploiting the strong germicidal capabilities of deep-UV radiation.

One of the main limitations of a realistic implementation of deep-UV devices lies in the thermal dissipation. Several studies have reported an output power conversion efficiency for blue-VCSELs and UVB-LEDs lower than the 10 % [8], meaning that all the input power that is not converted into optical power is dissipated into heat. Even more challenging is the implementation of UV-emitting vertical-cavity surface-emitting lasers (VCSELs). In fact, the poor refractive index difference and poor hole transport properties of nitride materials prevents the use of AlGaN distributed Bragg reflectors (DBRs). On the other hand, VCSELs based on dielectric DBRs exhibit mediocre heat conduction properties, leading to dramatic increases of the cavity temperature. In fact, only few nitride-based vertical-cavity structures with emission wavelength in the UV range have been reported so far: *Onishi et al. (2015)* [9] demonstrated CW lasing at 420 nm for an electrically injected GaN based VCSEL at room temperature, *Liu et al. (2016)* [10] demonstrated an optically pumped VCSEL structure based on an AlGaN cavity with a bottom electrically conductive DBR and emitting at 374 nm. The lowest reported wavelength for an AlGaN-based device have been obtained by *Chen et al. (2010)* [11], in which an emission wavelength of 343.7 nm have been achieved for an optically pumped cavity based on 3D AlGaN nanopillars. Therefore, it is straightforward to notice how thermal management in UV-emitting LEDs and VCSELs is a crucial issue for the developing and the future implementation of such kind of devices.

The scope of this thesis work is then to study the thermal characteristics of AlGaN-based UV-emitting thin-film flip-chip LEDs and VCSELs exploiting different device geometries to enhance the thermal dissipation in the proximity of the active region toward the heat sink and study the thermal effects in terms of cavity resonance shifts for the VCSELs, giving reliable and concrete inputs for the design of the next generation of deep-UV emitting devices.

## 1.1 Light-emitting devices: light generation mechanisms

Before proceeding with the thermal simulations of the semiconductor devices studied in this thesis work it is useful to have a small introduction to the theory behind light emission in light-emitting diodes and surface-emitting diode lasers.

From a quantum-mechanical description of the materials one can derive the allowed energy levels that electrons can occupy in a solid by solving the Schrödinger's time-independent equation, which is an eigenvalues equation whose solutions are the eigenvalues (energy levels) and eigenfunctions (wavefunctions) of the electronic population in the solid. In semiconductive materials the energy band structure is characterized by a forbidden energy gap which separates conduction and valence band. When energy greater than the forbidden gap is provided to the material it may cause the promotion of electrons from the valence to the conduction band, inducing the passage of the atomic state from the fundamental to an excited level. The passage of one electron to the conduction band leaves a vacancy in the valence band carrying a positive charge (i.e. holes). When a photon with energy higher (or at least equal) than the forbidden gap is absorbed by the material one electron-hole couple is generated. The electron-hole couple may be characterized by a certain binding energy due to the electrostatic Coulombic attraction between the opposite charge associated with the two particles. The generated bound state between electron and hole is identified as an *exciton*. A sketch of the transition from valence to conduction band is shown in figure 1.1.

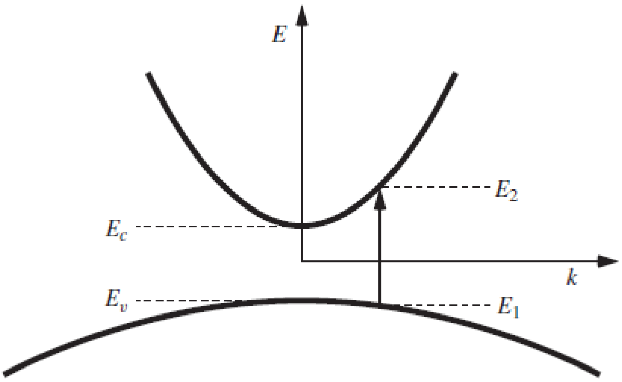

Figure 1.1: Energy band diagram of a direct bandgap semiconductor, showing a transition of one electron from a valence band bound state to a free-carrier state in the conduction band. Image from [12].

The generated electron in the conduction band can recombine with one hole releasing an energy equal to the difference between the two energy levels. If this energy is emitted as a photon we talk about radiative recombination. This carrier recombination mechanism can be exploited to build light emitting devices. Non-radiative recombination phenomena does not produce emission of radiation and they comprises Auger recombination and Shockley-Read-Hall recombination.

To summarize, four basic electronic recombination/generation mechanisms exists in a semiconductor [12]:

- Spontaneous recombination (photon emission, $R_{sp}$): one electron in the conduction band decays spontaneously to the valence band causing the emission of a photon with energy equal to the difference between the two energy levels. If a large number of such events occurs it would produce a relatively incoherent emission of light, because of the random emission time and directions. Spontaneous recombination is the main mechanism for LEDs operation, in which feedback is missing and no amplification of the signal occur.

- Stimulated generation (photon absorption, $R_{12}$): in which the absorption of photons with energy greater (or at least equal) to the bandgap causes the promotion of electrons from the valence to the conduction band, with the consequent formation of electron-hole couples (i.e. excitons).

- Stimulated recombination (coherent photon emission, $R_{21}$): it is the opposite process of stimulated generation. One incident photon perturbs the electronic system causing the relaxation of one electron from the conduction to the valence band (electron-hole couple recombination) with the consequent emission of an additional photon with same wavelength and phase of the impinging one. Stimulated recombination is at the basis of the operation mechanism of lasers, in which the presence of positive gain layers produces a positive feedback mechanism inducing the resonance of the radiation inside the cavity.
- Non-radiative recombination (Auger or defects/trap-assisted): are a set of recombination mechanisms which does not produce photon emission. On the contrary, the excess energy is dissipated mainly as heat.

Non-radiative recombination phenomena must be minimized in light emitting devices, in order to enhance the radiative mechanism and increase the conversion efficiency and, consequently, the optical output power.

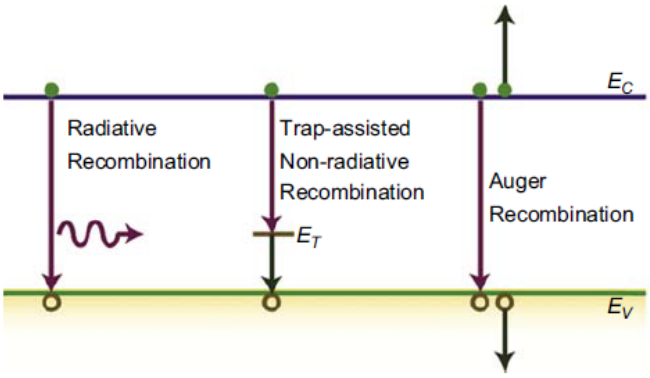

Figure 1.2: Sketch of the main radiative and non-radiative recombination mechanism in semiconductors. Image from [13].

## 1.2 Light Emitting Diodes (LEDs)

Light emitting diodes are pn junction based devices which are able to emit light upon injection of current in forward bias conditions. As already introduced in section 1.1, radiation is generated by spontaneous recombination mechanisms resulting in an incoherent light emission over a relatively broad range of wavelengths. The peak emission occurs around an energy value corresponding to the band-gap energy, so emission wavelength can be tailored by a proper choice of the materials.

The LED can be considered as a transducer, able to convert injected electrical energy into output optical power by the physical mechanism of *electroluminescence*. When a forward bias is applied to a pn junction, electrons in the n-side of the junction are injected into the p-side where they became minority carriers. The same injection mechanism can be applied to holes, which on the contrary moves from the p-side toward the n-side of the junction. The excess minority carriers have a density much higher than the thermodynamic equilibrium value, so that they recombine with the corresponding majority carriers with consequent emission of light [14].

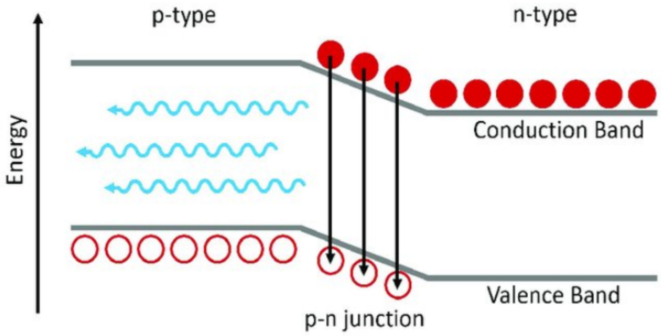

Figure 1.3: Schematic representation of the electron-hole recombination mechanism in pn-junction LED. Image from [15].

In order to increase the radiative recombination rate and minimize non-radiative phenomena, the excess injected carrier density should be higher in the regions where the optical recombination is desired. In standard p-n junction based LEDs carriers are distributed along the whole diffusion length and they can recombine in both the two diffusion region and the space-charge region (i.e. at the interface between p- and n- side). As a consequence, emitted photons can be reabsorbed by the material and they do not contribute to the output optical power. In order to increase the efficiency usually an asymmetric junction is exploited, in which the thin surface layer is less doped than the substrate [16]. To increase the output efficiency and reduce the re-absorption of the emitted radiation several alternative solutions can be used. In general, the active region of a LED can be composed by different structures [13]:

- a depletion region of a p-n junction obtained by a junction between two regions of the same material with opposite doping (i.e. homojunction), like in standard LED technology;
- a small bandgap region sandwiched between two wide bandgap regions, forming a double heterostructure p-n junction;
- a quantum well (QW) or quantum dot (QD) region embedded between two external barriers. The structure can be seen as a heterojuction but the reduced dimensions of the central region give rise to quantization of the energy states and confinement effects, which can be exploited to tailor the emission properties of the device.

Exploiting a double heterojunction design or the confinement effects in QWs or QDs, electrons remain trapped in the central region with narrower bandgap, thus increasing the carrier concentration inside the active region. Being the active region characterized by a smaller bandgap compared to the external layers, the emitted photons cannot be absorbed by the wide bandgap *cladding* layers and they are able in principle to reach the surface of the device. In such way carrier recombination rate is enhanced and the output efficiency is drastically increased.

### 1.2.1 Carrier generation and recombination in the active region

For the purpose of this work we will focus the attention on thin-film LEDs, in which the active region is epitaxially grown by alternating thin layers of wide and narrow bandgap materials. The active region is then composed by one or several QWs in which the injected carriers remain trapped and recombine radiatively. Indeed, only a fraction of the total injected carriers actually remain trapped in the small bandgap region and this percentage is referred as *injection efficiency* ($\eta_i$) [16].

Consider for simplicity a double-heterostructure LED composed by a narrow bandgap intrinsic region sandwiched between two wide bandgap doped regions, as shown in Figure 1.4. The current density in the active region is described by a dynamic process governed by a rate equation, according to which the time evolution of the carrier density is a function of the generation term $G_{gen}$, accounting for radiative and non-radiative recombination processes as well as carrier leakages, and a recombination term $R_{rec}$:

$$\frac{dN}{dt} = G_{gen} - R_{rec} \tag{1.1}$$

The generation rate $G_{gen}$ can be easily calculated as:

$$G_{gen} = \frac{\eta_i I}{qV} \tag{1.2}$$

where I is the total injected current, q is the elementary charge and V the volume of the active region.

The total recombination rate can be written as the sum of different contributions:

$$R_{rec} = R_{sp} + R_{nr} + R_l \tag{1.3}$$

where $R_{sp}$ is the spontaneous emission rate describing the spontaneous recombination with consequent emission of radiation, $R_{nr}$ is referred to non-radiative processes (Auger recombination, SRH recombination), $R_{sp}$ is the spontaneous recombination term describing the perturbation on the system by incident photons and $R_l$ is linked to carrier leakage from the QW region by thermally activated processes. In general, the main contribution to current leakage is due to the non-zero tails of the Fermi-Dirac distribution according to which the energy levels in the conduction bands are populated. Under the effect of temperature the tails of the distribution are enhanced and a fraction of the electrons trapped in the potential well are able to escape, giving a contribution to leakage current and thus reducing the injection efficiency. To reduce the leakages in AlGaN-based devices an electron blocking layer (EBL) is usually added in close proximity of the active region, by inserting a thin layer of material with wide-bandgap acting as a potential barrier for high energy electrons, preventing electron leakage toward the p-side cladding layers with a consequent decrease in the leakage current [17], [18].

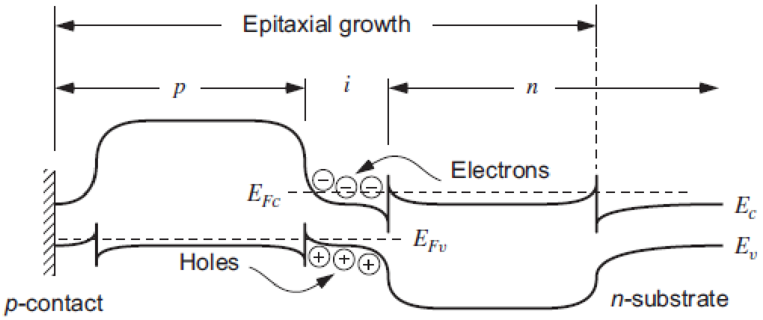

Figure 1.4: Band diagram of a forward biased double-heterostructure diode. Image from [19]

### 1.2.2 Photon generation and radiative efficiency

In steady-state conditions (i.e. dN/dt=0) the carriers generation rate equals the recombination rate

$$G_{gen} = \frac{\eta_i I}{qV} = R_{sp} + R_{nr} + R_l \tag{1.4}$$

where the stimulated recombination rate has been neglected, approximation which is acceptable in standard LED technology, whose operation relies on spontaneous recombination phenomena. On the contrary, the stimulated recombination term must be taken into account in laser physics where the stimulated recombination mechanism plays a major role in the emission.

Since the dependence of $R_l$ and $R_{nr}$ on I is not well-know, for simplicity the *radiative efficiency* is introduced. This term is defined as the ratio between the spontaneous emission rate and the total generation rate

$$\eta_r = \frac{R_{sp}}{R_{sp} + R_{nr} + R_l} \qquad \longrightarrow R_{sp} = \eta_r \frac{\eta_i I}{qV}. \tag{1.5}$$

The spontaneous emission rate $R_{sp}$ describes the number of photons generated by spontaneous emission per unit volume and unit time. Therefore, the spontaneously emitted output optical power can be simply calculated by multiplying $R_{sp}$ by the energy per photon ($h\nu$) and the volume of the active region V:

$$P_{sp} = h\nu V R_{sp} = \eta_i \eta_r \frac{h\nu}{q} I \tag{1.6}$$

The total output power is then obtained by multiplying $P_{sp}$ by the collection efficiency $\eta_c$. The collection efficiency defines the fraction of photons that are actually collected by the detector. In fact, not all the emitted photons from the active region are able to reach the surface and being emitted. Due to the refractive index difference between the substrate and the surrounding environment (air) part of the emitted photons are reflected back into the device by total internal reflection (TIR) at the surface, reducing the output optical power. TIR is a major issue in LEDs. Novel structure have been exploited in order to reduce the TIR at surface, including surface roughening [20] or substrate microstructuring [21]. However, the TIR phenomenon is limited in nitride based devices with respect to the case of III-arsenide based devices, characterized by a bigger refractive index and smaller critical angles. Thus, the main limitation in ultraviolet LEDs is more related to the challenges in the surface microstructuring, losses in the substrate and polarization of emitted light. All these problems can be partly reduced by using the thin-film flip-chip geometry.

### 1.2.3 Thin-film flip-chip (TFFC) LEDs

One of the main solutions to increase the external quantum efficiency is the use of a different design to enhance light extraction and collection.
One of the most used structures is the thin-film LED (TF LED), which is characterized by an epitaxially grown active region based on multiple quantum wells, for high carrier injection efficiency, sandwiched between two external wide bandgap layers. The small thickness of the resulting device compared to the top surface area guarantees that only a negligible part of the generated light is emitted from the lateral walls, so that the majority of the light is directed toward the top surface, enhancing the extraction efficiency.
The output efficiency can be further improved by using the flip-chip design. This technique can be applied on both standard and thin-film LEDs and it exploits substrate removal steps after which the device is flipped and bonded to the carrier chip. In such way the n-side surface is completely exposed and the light extraction efficiency is enhanced. The p-side is therefore metallized to double function as a reflector and p-contact.
Several techniques can be used for substrate removal, but the application depends on the materials used in the device:

- Standard Wet Etching is typically used for in IR or visible-emitting devices (based on GaAs/InP alloys). For deep-UV applications this technique is usually avoided since nitrides are practically inert to wet etching, thus alternative solutions for substrate release are required;

- Laser lift-off (LLO) has been efficiently used for visible emitting blue devices based on GaN, but the exposed surface after substrate release is relatively rough and a poor control of the thickness is achieved. In addition, in AlGaN-based devices the stress induced in the device may generate cracking and thermal decomposition of AlGaN leaves Al-residues that are difficult to remove. Thus, it is in general avoided in deep-UV applications but it results to be quite efficient in long wavelength emitting devices;

- Chemical mechanical Polishing (CMP) is based on the combination of mechanical abrasion and chemical etching of the substrate. This technique has good performance but the substrate is not reusable. This is particularly to be avoided when using nitride-based expensive substrates, like AlN, and it does not offer the precise thickness control required for VCSELs processing;

- Electro-Chemical Etching (ECE) is a new technique that has been recently demonstrated to work also on AlGaN-based material, achieving complete etching of a sacrificial AlGaN-based layer with really smooth surfaces and good thickness control. This is the technique used in the devices studied in this work to perform substrate removal prior to the flip-chip bonding, both for the LEDs and VCSELs.

## 1.3 Vertical-Cavity Surface-Emitting Lasers (VCSELs)

The main requirement for any laser structure are a pump source (in general pumping can be induced by optical injection by means of an external laser or current injection through electrical contacts), an active medium for light amplification by stimulated emission and a resonator, which provides optical feedback.

Semiconductor lasers are light emitting devices with semiconductive gain medium. The gain medium is designed and properly chosen in order to amplify radiation over a specific range of wavelengths. When sufficiently *pumped*, by either electrical or optical energy, enough electrons present in the material are excited to higher energy levels to achieve the *inversion of population condition*. In this state, higher energy levels are more populated than lower energy states, where the carrier density is reduced. This condition is required to have lasing, since only in population inversion the active region provides gain, i.e. the stimulated emission is larger than the absorption. Above a certain threshold of pumping, the resonant cavity provides sufficient positive feedback for the amplification to overcome the losses and lasing can be established. The obtained generated light is mostly coherent and characterized by a very narrow linewidth.

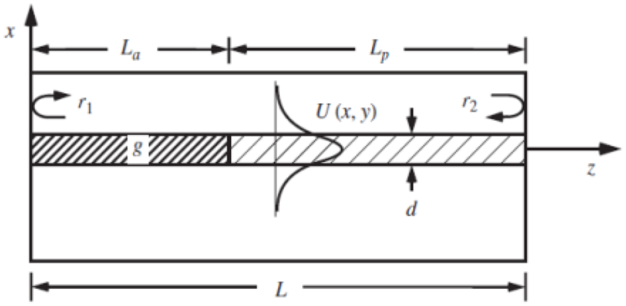

Figure 1.5: Simple structure of a laser resonant cavity. The laser cavity is in a standard Fabry-Perot configuration, with emission from the edge of the device. Image from [19].

There are two main types of semiconductor lasers, which can be classified according to the direction of propagation of the light with respect to the epitaxial growth direction:

- Edge-Emitting Lasers (EELs), in which the output beam is emitted through one of the cleaved facets perpendicular to the plane of the epitaxial layer;
- Vertical-Cavity Surface-Emitting Lasers (VCSELs), in which the output light beam is emitted perpendicularly to the epitaxial plane.

In standard edge-emitting lasers the light propagates perpendicularly to the epitaxial structure and emerges from one of the two cleaved facets which act as reflectors. The non symmetric waveguide results in an elliptical and highly-divergent output beam. Due to the long cavity the emission is typically multi-mode. High output powers are in general easily achievable, making EEL the most used choice for high-power applications.

On the contrary, VCSELs are characterized by a light propagation perpendicular to the epitaxial layer. The mirrors of the resonant cavity are then composed by Distributed Bragg

Reflectors (DBRs), which are characterized by an alternating stack of high and low refractive index materials. The light is emitted from either the top or bottom surface of the device, resulting in a circular, symmetric and low-divergent output beam, making it possible to collimate the light beam by a simple lens. The really short cavity allows for longitudinal single mode emission, but the output power is significantly smaller than the one obtained for standard edge-emitting devices. The vertical emission and the small dimensions of VCSELs allow for easy integration with standard opto-electronics and device testing right after growth, before wafer dicing. In addition, single VCSELs can be combined and integrated in two-dimensional arrays, allowing for higher output optical power maintaining a relatively high quality of the total output light beam.

### 1.3.1 VCSEL structure

As already anticipated in the previous section, in a VCSEL the resonant cavity is defined by an active gain region sandwiched between two DBR mirrors. The gain section is responsible for the amplification of the signal emitted by the MQWs based active region. The epitaxial structure is in general grown by Metal Organic Chemical Vapor Deposition (MOCVD) or Molecular Beam Epitaxy (MBE) in order to obtain high-quality layers of controlled thickness.

The pumping can be obtained either optically by an external laser with shorter wavelength than the emission one or electrically, through electrical contacts for current injection. In the latter case the current path is defined by current confinement strategies, such as the creation of an oxide aperture by lateral oxidation or ion implantation.

The generated light resonates in the cavity by multiple reflections at the top and bottom mirrors and it is emitted from one of the two DBRs, properly engineered to be less reflective. In general, a VCSEL can be designed to emit either from the top DBR by using a top ring contact or from the bottom of the device through a transparent substrate. In figure 1.6 a typical structure of an electrically pumped VCSEL is illustrated.

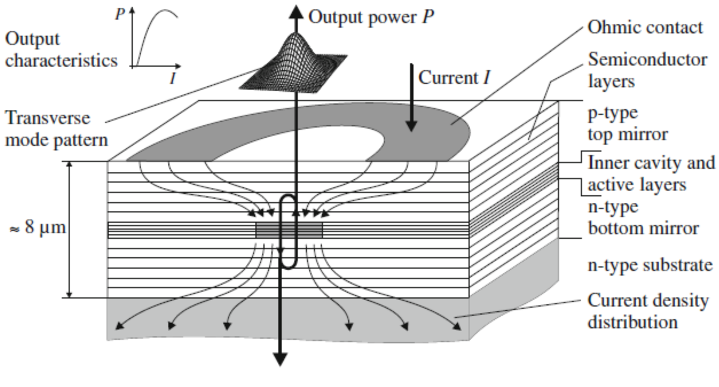

Figure 1.6: Schematic layer structure and operating principle of a VCSEL. Electrical injection is achieved by a top ring contact, which allows the emission from the top surface by the central hole. Image from [22].

### 1.3.2 Distributed Bragg Reflectors

In a VCSEL the mirrors of the resonant cavity are two distributed Bragg reflectors (DBRs). The structure consist of a stack of alternating layers with high and low refractive index, each one of a thickness corresponding to one-quarter of the wavelength in the material. Due to the vertical geometry where the thin active region only gives a small amplification per roundtrip, a high number of DBR pairs are required to achieve high reflectivity and so high gain. The maximum reflectivity is achieved at the Bragg wavelength which is defined starting from the grating period $\Lambda$:

$$\lambda_B = 2\Lambda n_{eff} \tag{1.7}$$

where $n_{eff}$ is the effective refractive index of the grating. Consider a DBR stack composed by $\mathrm{M}_{Bt,b}$ pairs of layers with alternating high and low refractive index, respectively indicated by $\bar{n}_1$ and $\bar{n}_2$. The index sequences can be expressed as $\bar{n}_c|\left(\bar{n}_1|\bar{n}_2\right)^{M_{Bt}}|n_{air}$ for the top mirror and $\bar{n}_c|\left(\bar{n}_1|\bar{n}_2\right)^{M_{Bb}}|\bar{n}_1\bar{n}_s$ for the bottom mirror, where $n_c$ is the refractive index of the cavity and $\bar{n}_s$ is the refractive index of the substrate. At the Bragg wavelength $\lambda_B$ the peak reflectivity can be computed as [23]

$$R_{t,b} = \left(\frac{1-b_{t,b}}{1+b_{t,b}}\right)^2 \tag{1.8}$$

with

$$b_t = \frac{\bar{n}_s}{\bar{n}_c}\left(\frac{\bar{n}_1}{\bar{n}_2}\right)^{2M_{Bt}} \qquad \mathit{and} \qquad b_b = \frac{\bar{n}_1^2}{\bar{n}_c\bar{n}_s}\left(\frac{\bar{n}_1}{\bar{n}_2}\right)^{2M_{Bb}} \tag{1.9}$$

The two refractive index $\bar{n}_1$ and $\bar{n}_2$ are the refractive indexes of the layers in the DBR stack, while $\bar{n}_c$ and $\bar{n}_s$ are the refractive indexes associated to the cladding layer (i.e. the cavity in a VCSEL) and substrate.

The broad range of wavelengths that are reflected back from the DBR is called stop-band and it can be calculated as:

$$\Delta\lambda_{stop} \approx \frac{2\lambda_B\Delta\bar{n}_B}{\pi\langle\bar{n}_{gr}\rangle} \tag{1.10}$$

where $\langle\bar{n}_{gr}\rangle$ is the spatial average of the group index $\bar{n}_{gr} = \bar{n} - \lambda d\bar{n}/d\lambda$ and $\Delta\bar{n}_B = |\bar{n}_1 - \bar{n}_2|$ is the refractive index difference between the two layers of each DBR pair. Thus, the stop-band is proportional to the refractive index step of the grating and to achieve high reflectivity over a wider range of wavelengths materials with high difference in refractive index are preferred. Near the Bragg wavelength the phase of the reflectivity varies almost linearly. Such reflection can be approximated by a discrete mirror reflection ($r_{eq}$) placed at a distance $L_{eff}$ from the beginning of the DBR. In this picture, the reflectivity can be written as

$$r = |r_{eq}|e^{-j\phi} = |r_{eq}|e^{-j2\beta_r L_{eff}} \tag{1.11}$$

so that the effective length can be obtained from the phase change as

$$l_{eff} = -\frac{1}{2}\frac{d\phi_r}{d\beta} = \frac{\lambda^2}{4\pi\langle\bar{n}_{gr}\rangle}\frac{d\phi_r}{d\lambda} \tag{1.12}$$

According to the Coupled Mode Theory (CMP), which is a perturbative approach in which the coupling between modes is reflected into a perturbation of the refractive index of the material, and assuming lossless mirror ($\sqrt{R} \approx 1$) the latter expression reduces to

$$l_{eff} \approx \frac{\tanh(\kappa L_B)}{2\kappa} = \frac{\sqrt{R}}{2\kappa} = \frac{\sqrt{R}}{2\kappa} = \frac{\sqrt{R}\lambda_B}{4\Delta\bar{n}_B} \approx \frac{\lambda_B}{4\Delta\bar{n}_B} \tag{1.13}$$

where $L_B$ is the total length of the DBR mirror and $\kappa = 2\Delta\bar{n}_B$ is the coupling coefficient of a quarter wavelength stack.
The total effective length of the cavity is then calculated as the sum of the length of the inner cavity and the penetration depth of the field in the DBRs: $L_{eff} = L + l_{eff,t} + l_{eff,b}$, where $L$ is the length of the inner cavity. From the effective length, finally, the spacing between the different allowed cavity modes can be estimated

$$\Delta\lambda_l \approx \frac{\lambda^2}{2L_{eff}\langle\bar{n}_{gr}\rangle} \tag{1.14}$$

It is straightforward to notice how in a VCSEL single longitudinal mode emission is easily achievable. Being the cavity epitaxially grown, the thickness of the inner cavity is small leading to a big spacing between the different resonant modes in the cavity, so that only one cavity mode falls within the reflectivity curve of the DBR and the spectral gain bandwidth (i.e. lasing mode).

### 1.3.3 Confinement factor and threshold gain

Because of the small thickness of the active gain region the overlap between the standing wave pattern and the gain region must be considered in order to calculate the average gain of the cavity. For that purpose, the relative confinement factor (or gain enhancement factor) is introduced and defined as the average intensity in the active region normalized to the average intensity over the whole inner cavity of the laser [24]

$$\Gamma_r = \frac{L}{d_a}\frac{\int_{d_a}|E(z)|^2dz}{\int_L|E(z)|^2dz}. \tag{1.15}$$

The gain condition for lasing can be obtained by the first Barkhausen round-trip condition (i.e. in order to sustain resonance the round-trip gain in absolute value is equal to unity: $|RT| = 1$), such that at threshold the modal gain equals the cavity losses (mirror + material)

$$g_{th} = \alpha_m + \langle\alpha_i\rangle = \alpha_a + \frac{1}{\Gamma_r d_a}\left[\alpha_i\left(L_{eff} - d_a\right) + \ln\frac{1}{\sqrt{R_t R_b}}\right] \tag{1.16}$$

where $d_a$ is the thickness of the active region, $\alpha_a$ refers to the internal losses in the active region and $\alpha_i$ is in general the spatial average over the locally varying loss coefficient, where weighting with the standing wave intensity has to be applied. The latter contains scattering and diffraction loss components and free-carrier absorption contributions in doped semiconductors [22].
Once the threshold gain is known, the photon lifetime can be calculated as

$$\frac{1}{\tau} = \frac{d_a}{L_{eff}}v_{gr}\Gamma_r g_{th} \approx v_{gr}\left[\alpha_i + \frac{1}{L_{eff}}ln\frac{1}{\sqrt{R_t R_b}}\right] = v_{gr}\left(\langle\alpha_i\rangle + \alpha_m\right) \tag{1.17}$$

where the group velocity of the laser mode is $v_{gr} = c/\langle\bar{n}_{gr}\rangle$. In equation (1.17) a further approximation is imposed by considering $\alpha_a \ll g_{th}$ and $d_a \ll L_{eff}$, conditions which are usually satisfied in conventional VCSELs.

### 1.3.4 Threshold current

Once the threshold gain is calculated, the threshold current can be obtained. The gain for a MQWs based active region can be expressed by a simple three-parameters logarithmic formula which expresses the dependence on the carrier density [19]:

$$g(n) = g_1 ln\frac{n + n_s}{n_t + n_s} \tag{1.18}$$

where $g_1$ is a fitting parameter, n is the carrier density, $n_s$ is a shift imposed to force the natural logarithmic to be finite at n=0 (so that the gain equals the unpumped absorption due to band-to-band transitions), and $n_t$ is the transparency carrier density (i.e. such that $g(n_t = 0)$). If we restrict the model only to non-negative gains the latter formula can be further approximated to a two-parameter expression:

$$g(n) = g_0 \ln \frac{n}{n_t} \tag{1.19}$$

with $g_0$ as a fitting parameter as well.
Assuming no off-set between gain peak and resonance wavelength the current density can be calculated as

$$j_{th} = \frac{qd_a}{\eta_I \tau_{sp}} n_{th} \tag{1.20}$$

where q is the elementary charge, $d_a$ is the active region thickness, $n_{th}$ is the threshold carrier density and $\eta_I$ is the carrier injection efficiency. The other parameter appearing in equation 1.20 is the spontaneous recombination lifetime $\tau_{sp}$, which depends on the carrier density:

$$\frac{1}{\tau_{sp}(n)} = \frac{1}{\tau_{sp,r}(n)} + \frac{1}{\tau_{sp,n}(n)} = A + Bn + Cn^2 \tag{1.21}$$

with A,B and C coefficients related to non-radiative interface or surface recombination, radiative bimolecular recombination and Auger recombination, respectively.
The threshold current is finally calculated by multiplying the threshold current density $j_{th}$ by the active region area $A_a$:

$$I_{th} = j_{th} A_a = \frac{qV_a}{\eta_I \tau_{sp}} n_{th} = \frac{qV_a}{\eta_I} \left( An_{th} + Bn_{th}^2 + Cn_{th}^3 \right) \tag{1.22}$$

where $V_a = A_a d_a$ is the active volume. Being the threshold current directly proportional to the active region area, it is straightforward to observe that for small active region volumes really low threshold current can be achieved.
In Figure 1.7 the gain as a function of the carrier density is shown. When threshold is reached the gain remains constant at the value it reaches at threshold, causing the carrier density to remain constant as well. Above threshold any increase in current turns to emitted photons and no carrier density increase is observed. This situation is clearly shown in Figure 1.8, where the carrier density as a function of the injected current is represented.

In order to better understand the meaning of laser threshold, some further considerations can be done. In general, the condition to sustain resonance are known as Barkhausen round-trip conditions, which are not satisfied by one single mode but several longitudinal modes are allowed in the cavity. Among all the allowed modes just few of them satisfy the laser threshold condition $RT = 1$. Below threshold an increase in the current lead to an increase in the carrier population and gain. When the laser threshold is reached the gain does not

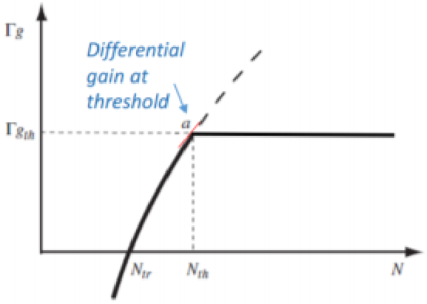

Figure 1.7: Gain curve versus carrier density.

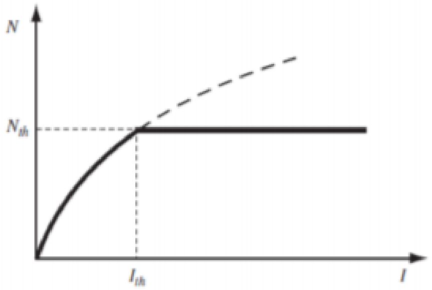

Figure 1.8: Carrier density versus injected current.

increase anymore with current and it is clamped to its threshold value, so that an increase in the current results in an increase of the emitted photons. This situation is expressed schematically in figure 1.9. Notice that the graphs in figure shows the spectral gain for an edge-emitting laser, since the spacing between the longitudinal modes in a VCSEL is smaller than the gain curve width, but the theory behind the laser operation is exactly equal in the two cases.

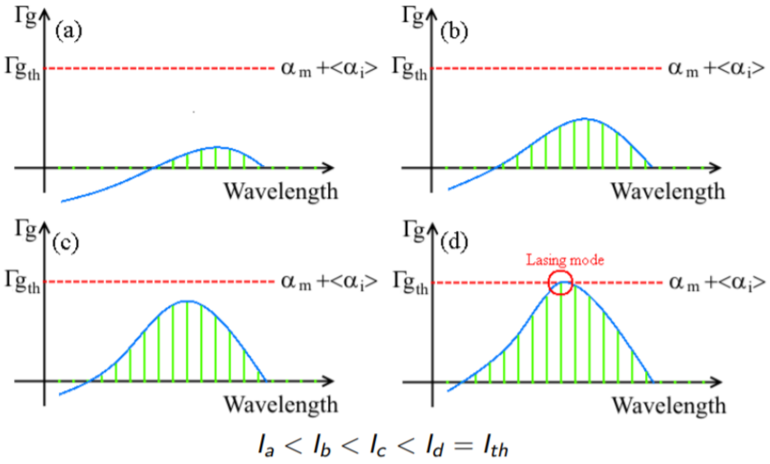

Figure 1.9: Spectral gain evolution for increasing injected current for an EEL laser.

### 1.3.5 Output power and Quantum Efficiency

Above threshold, the output power emerging from either the top or the bottom mirror of the laser resonator increases linearly with driving current [19]:

$$P_{b,t} = \eta_{dt,b} \frac{\hbar\omega}{q} (I - I_{th}) \qquad (I > I_{th}) \tag{1.23}$$

where the quantity $\eta_{dt,b}$ is the *differential quantum efficiency* defined as the fraction of injected electron that produces coherent emission from the top or bottom mirror and can be experimentally measured by calculating the slope of the P-I curve. As illustrated in Figure 1.10, below threshold the generation of photons is dominated by spontaneous emissions processes, while above threshold the stimulated emission dominates and the spontaneous emission is clamped at its threshold value.

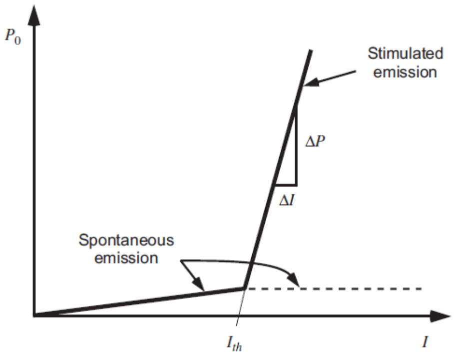

Figure 1.10: Output power versus driving current curve. [19]

## 1.4 Heat transport in semiconductor devices

Heat is one of the main limiting mechanism of the performance of opto-electronic devices. In fact, all the power dissipated by heat (or more in general by non-radiative phenomena) could potentially contribute to the output optical power. Thus, minimizing the temperature is one of the key points in improving the output performance of photonic devices.
The thermal problem is critical in deep-UV emitting devices. Power conversion efficiency in such kind of devices is still limited to a maximum of 10% for blue-VCSELs and UV-emitting thin-film flip-chip LEDs, while no lasing below 340 nm have been reported for AlGaN based VCSELs. Thus, a good thermal management in UV-emitting devices is crucial to push the emission to shorter wavelengths and to exploit the advantages of deep-UV light.

### 1.4.1 The Heat Equation

Heat transport in semiconductive devices is described, under steady state conditions, by the *heat equation*, which is a second order partial differential equation describing the distribution of heat in space:

$$\boldsymbol{\nabla} \cdot (\kappa \nabla T) = -Q_{tot} \tag{1.24}$$

where $\kappa$ is the thermal conductivity, T is the temperature increase computed with respect to the heat sink temperature $T_0$. The term $Q_{tot}$ comprises all the heat sources and it can be written as the sum of different contributions [25]:

$$\begin{aligned} Q_{tot} &= Q_{Joule} + Q_{optical} + Q_{rec} + Q_{capt/esc} \\ &= \sigma^{-1}||\mathbf{J}||^2 + \alpha W_{opt} + E_g R_{nr} + \Delta_{C/V} C_{n/p}^{cap} \end{aligned} \tag{1.25}$$

Let's analyse each term separately. The first term $Q_{Joule}$ is referred to Joule heating dissipation mechanism. The generated heat is in general proportional to the electrical conductivity $\sigma$ and the injected current density $\mathbf{J}$: when a current flows into a resistance it generates a temperature increase proportional to the square of the current. The self heating mechanism by Joule effect is particularly critical in nitride based devices due to the high resistance of the cladding layers, so a careful control on the cavity self-heating is required when considering electrically injected devices. Joule heating is the major heating effect in LEDs, while the UV VCSELs still relies on an optical pumping mechanism such that the contribution of Joule heating is not present and the main contribution to the heat is due to non-radiative recombination processes. The second term $Q_{opt}$ is related to optical absorption mechanisms, in which intra-band and free carrier absorption are included through the absorption coefficient $\alpha$ and $W_{opt}$ is the 3D modal power density profile. Non-radiative phenomena, including Auger and Shockley-Read-Hall (SRH) recombination, are included in the third therm $Q_{rec}$ where $R_{nr}$ describes the non-radiative recombination rate and $E_g$ is the energy gap of the material. The last term models the contribution of carrier escape/capture, with $\Delta_{C/V}$ being the conduction-valence band offset and $C_{n/p}$ is the corresponding capture/escape rate. In principle, also Peltier and Thomson effects should be included in the heat equation, but they are negligible with respect to the other thermal phenomena [25] and thus can also be not included in the total heat equation.

### 1.4.2 Temperature effects in VCSELs

VCSELs are more than other types of emitting devices sensitive to temperature effects. The temperature rise in VCSEL cavities due to self-heating effects, Joule heating and carriers non radiative recombination will induce a drastic reduction of the laser output performance. Three main temperature-induced effects can be summarized for a VCSEL as a consequence of the increasing temperature in the cavity:

1. Increase in the threshold current density. The main contribution is found to be Auger recombination, vertical carrier leakage in the MQWs active region [26] and detuning between gain peak and resonance wavelength;

2. Thermal roll over, which is the reduction of the output power with increasing temperature. The self-heating in VCSELs cavity limits the output power of such devices to below 20 mW [27], [28];

3. Detuning between the gain peak and the resonance wavelength. In a VCSEL the emission wavelength is determined by the resonance peak which falls under the gain peak. With increasing temperature in the cavity both the resonance wavelength and the gain peak experience a red shift. The shift, however, occurs at different rates so that the detuning between these two quantities determines the VCSEL output performance.

Let's proceed analysing each effect and its dependence on the increasing temperature separately.

#### Increase in threshold current density

The threshold current density in VCSELs is the nominal value of injected current necessary to induce lasing. Above threshold the number of higher energy states is much more populated with respect the the fundamental level so that the inversion of population condition is achieved and the stimulated recombination dominates over the spontaneous recombination mechanism.

The temperature dependence of the threshold current can be obtained by studying the temperature dependence of the quantities appearing in the expression of the threshold current reported in equation 1.22. Considering that around threshold the main recombination mechanism is the spontaneous recombination and expliciting the expression for the carrier density at threshold, equation 1.22 reduces to:

$$I_{th} \simeq \frac{qV_a}{\eta_I} B n_{th}^2 = \frac{qV_a}{\eta_I} B \left( N_{tr} e^{\frac{\langle \alpha_i \rangle \alpha_m}{\Gamma g_0}} \right)^2 \tag{1.26}$$

where $n_{tr} \propto T$, $g_0 \propto 1/T$ and $\alpha_i \propto T$ [19]. Therefore, it can be concluded that the threshold current density has an overall exponentially increasing behaviour with temperature.

Any other recombination mechanism, such as Auger or SRH recombination, as well as carrier leakages will enhance the above described temperature dependence. In fact, an increase in temperature increases the vertical leakage of carriers, such that electrons trapped in the QW region gain sufficient energy to escape from the potential well and are injected in the contact layers of the cavity where the recombination of carriers does not contribute actively to the output optical power. So the amount of carriers injected in the cavity must be higher to achieve the same carrier population in the QW so that the threshold current increases as well.

### Thermal roll-over

The thermal-roll over mechanism is defined as the premature saturation of the output power with increasing bias current, under CW operation. In fact, increased heat in the cavity reduces the total amount of power that can be converted into optical power reducing the efficiency of the device. Thermal roll-over is one of the main limitations of nitride based emitters, whose optical power is limited by the non-optimized dissipation of heat in the device.

### Detuning between resonance wavelength and gain peak

The major problem related to the increasing temperature in the cavity is the red shift of the resonance wavelength in the cavity with increasing temperature. The resonance wavelength of the resonator is shifted toward higher wavelengths as temperature increases. This is a direct consequence of the increase in the refractive index of the material. This leads to an increase in the optical length of the cavity and thereby a longer resonance wavelength.

The gain peak experiences also a red shift but the rate is reduced compared to the shift of the resonance wavelength. The gain peak shift is indeed directly related to the band gap shrinking with increasong temperature. The emission of light from the QW will then occurs at lower energies which corresponds to higher wavelengths.

The detuning between gain peak and resonance wavelength will then directly affect the optical properties of the device. In fact, if the wavelength of the resonator does not fall in correspondence with the gain peak the output optical power will be drastically reduced with respect to the maximum achievable power with a consequent reduction in the efficiency.

### 1.4.3 Thermal effects in LEDs

Similar effects as the ones reported for the VCSELs affect the LEDs technology. The high temperature rise in the active region is, in this case, mainly related to Joule heating effects. The relatively high n- and p- contact resistances lead to high operating voltages in UV LEDs with a consequent self-heating in CW operation [29]. This self-heating has as main consequence the saturation of the output power, which results to be limited as the temperature in the device increases (i.e. analogous effect to the thermal roll-over for the VCSELs). The maximum achievable output power is then limited to few milliWatts in CW operations, while relatively higher values can be obtained in pulsed operation regimes where the P-I characteristic shows an approximately linear trend [30].

The second temperature effect in LEDs is the red shift of the peak wavelength, which shifts toward higher values [31]. This is due to the band gap narrowing with increasing temperature, which leads to the absorption and then emission of photons with lower energies. Thus, above RT the emission wavelength results to be shifted. Other secondary effects includes the reduction of the PL peak and the broadening of the full-width at half maximum (FWHM) of the emission peak [31]. The latter effect is mainly related to the increase in near-band edge (NBE) transition probability due to the presence of defects. The defects density increases with increasing temperature due to the difference in the thermal expansion coefficient of the epi-layers with a consequent increase in the relative strain between the thin films [32].

The optimization of the thermal resistance is in the case of LEDs mainly related to the device packaging which offers a great flexibility in the design. Due to the low thermal conductivity of sapphire (3.5 $\mathrm{Wm^{-1}K^{-1}}$), which is commonly used as substrate in UV emitting LEDs, the flip-chip design is usually exploited to allow for the bonding of the device to an AlN carrier chip [8],[33]. AlN is indeed characterized by a higher thermal conductivity leading to a better heat spreading toward the heat sink.

# 2 | Thermal simulations of UV-emitting VCSELs and LEDs

In this chapter the thermal properties of UV-emitting VCSELs and LEDs are studied. The heat flow in the device and the maximum temperature achieved in the active region are simulated in COMSOL Multiphysics, by means of 2D and 3D steady-state simulations.
The results obtained for the initial structure are then used as starting point to modify the geometry in order to achieve a better thermal dissipation of the heat in the device.
The thermal resistance for each geometry is then calculated and used as a figure of merit to compare the different designs.
Three different type of devices are analysed in the following: optically pumped UVB-VCSELs, with an AlGaN based cavity, optically pumped UVC-VCSELs, with a similar structure to the one used for the UVB lasers but the cavity is AlN-based, and UVB emitting LEDs. In the latter case, four designs are studied to better manage the current crowding effect established between the p- and n-electrode.

## 2.1 UVB Vertical-Cavity Surface-Emitting Lasers (VCSELs)

Vertical-Cavity Surface-Emitting Lasers (VCSELs) are semiconductor-based laser diodes which emit light normal to the device surface. These devices have gained a great attraction in the past few years due to their capability of single-mode emission, circularly symmetric Gaussian beam profiles, small divergence angles, low threshold currents and simple packaging. At the same time, the VCSEL design provides a relatively easy 2D array integration and low manufacturing costs, compared to their edge-emitting counterpart.
The thermal behaviour of the device plays a crucial role in the optimization of the output performance of the laser. In lasers composed of a resonant cavity made by wide-bandgap materials with a double dielectric DBR configuration, the low thermal conductivity of the materials is responsible for the drastic reduction of the vertical heat transport through the bottom DBR mirror with a consequent increase in the cavity temperature and so of the thermal resistance. On one hand, the use of dielectric materials increases the miniaturization capability (a lower number of layer is required to reach the same reflectivity of an epitaxial DBR). On the other hand, due to the very low thermal conductivity of the materials, the heat transport in the vertical direction from the active region toward the heat sink is drastically reduced. The self-heating generated in the cavity leads to an increase in the non-radiative carrier losses and an increase in the threshold current, a reduction of output power, a shift of the lasing wavelength, and a decrease of the slope output efficiency and the differential quantum efficiency [26], with a consequent reduction of the performance in CW operation.

Additionally, the operating lifetime of semiconductor lasers usually decrease exponentially with temperature. Therefore, a good thermal management in the structure is required to increase the lifetime of the device and increase the efficiency.

### 2.1.1 Double dielectric DBR structure

One of the biggest challenges for UV-emitting VCSELs lies in the need for high reflectivity DBRs. Dielectric mirrors as replacements for epitaxially grown thermally conductive DBRs have many advantages from an optical point of view. The high refractive index contrast between the materials composing the DBR allows for using a lower number of pairs with respect to their epitaxial counterpart, achieving easily a very high reflectivity ($\sim$ 99%) and a wide stop-band.

The structure of the UVB-emitting VCSEL studied in this section is reported in Figure 2.1. The use of a double dielectric DBR structure requires a modification of the technological process due to the impossibility to grow the cavity directly on the dielectric materials. For that purpose, the laser cavity is first epitaxially grown on an AlN or sapphire substrate. The DBR, corresponding to the bottom mirror in the final structure, is deposited by sputtering on top of the epitaxial structure. Finally, the metal stack required for the bonding is deposited on the DBR mirror and it composed of Au(200 nm)/Ti(10 nm)/$SiO_2$(20 nm)/Al(50 nm). The 50 nm thick Al layer is used to increase the reflectivity of the bottom DBR and to reuse part of the optical pump power not absorbed by the active region. A thin $SiO_2$ layer is used to separate Al and Au and avoid interdiffusion of the materials. At this point, the substrate is released by electrochemical etching (ECE) of a sacrificial layer. The advantages of using ECE for substrate removal with respect to the conventional lift-off process relies on the possibility of a better control in the cavity length and for a reduced roughness of the top cavity surface, reducing the scattering losses at the interface between the top surface of the cavity and the DBR. In the VCSEL processing, usually the sacrificial layer consist of an $Al_{0.37}Ga_{0.63}N$ laye, on top of which an $Al_{0.11}GaN/Al_{0.37}GaN$ superlattice is grown. The presence of the superlattice in contact with the laser cavity allows to enhance the etching at the top surface obtaining a very smooth profile, essential to minimize the losses.

After the ECE step the structure is flipped upside down and bonded to the Au covered silicon carrier. After the bonding process, the top DBR mirror is deposited on the AlGaN cavity. In this way, the AlGaN cavity becomes completely enclosed between two dielectric DBR mirrors, composed of a stack of alternating $SiO_2$(53.8 nm)/$HfO_2$(36.8 nm) layers.

The cavity is designed to emit in the UVB-range at 320 nm and it is composed by an active region consisting of five $Al_{0.2}Ga_{0.8}N/Al_{0.5}Ga_{0.5}N$ QWs, sandwiched between two $Al_{0.6}Ga_{0.4}N$ layers.

If on one hand the optical properties of dielectric DBRs are superiors in the UV range, the poor thermal conductivity of the dielectric materials used for the DBRs inhibits the vertical heat transport from the active region toward the heat sink, leading to a dramatic increase in the cavity temperature.

In the following, the heat flow and the temperature profile are calculated for different designs, in order to study the improvements of the thermal performance of the device, reducing the thermal losses and increasing the output power and the efficiency of the laser.

The thermal resistance of the different structures ($R_{th}=\Delta T/P_{diss}$) is then calculated and used as a figure of merit to compare the different structures from a thermal perspective.

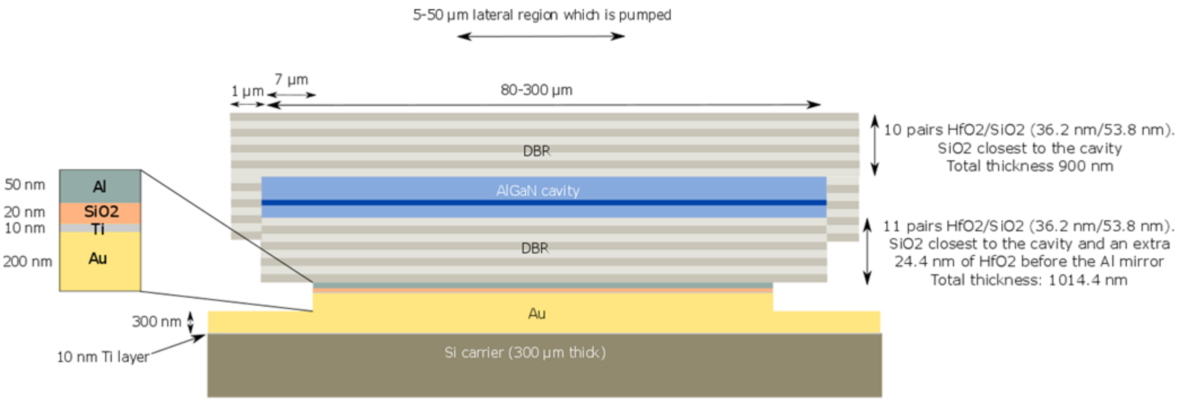

Figure 2.1: UVB-VCSEL structure with double dielectric DBR and 2.5$\lambda$ cavity length.

### Structure modelling

The simulations are carried out by using the commercial tool COMSOL Multiphysics in steady-state conditions. As the VCSEL structure is symmetric around the z-axis (perpendicular to the emission surface), a 2D axisymmetric geometry is used: half of the device is built in two dimensions and it is rotated around the z-axis to build the 3D structure.

A particular attention must be devoted to the modellization of multi-stacked structures, in which the multiple interfaces between the thin layers acts as additional scattering centers by interfacial phonons reducing the overall thermal conductivity with respect to the bulk materials. Thus, both the DBR and QWs region can be modelled as effective layers with anisotropic thermal conductivity [34], calculated as:

$$\kappa_{th,L} = \frac{\kappa_1 d_1 + \kappa_2 d_2}{d_1 + d_2} \quad ; \quad \kappa_{th,V} = \frac{d_1 + d_2}{\frac{d_1}{\kappa_1} + \frac{d_2}{\kappa_2}} \tag{2.1}$$

where $d_1$ and $d_2$ are the thicknesses of the two layers of the stack and $\kappa_1$ and $\kappa_2$ are the associated thermal conductivities. Isotropic thermal conductivity is assumed for all the other layers.

The small thickness of the active region with respect to the cavity cladding layers allows to lump all the heat sources in the active region [35], as a disk of diameter d=20 µm and thickness 85 nm. The heat source is passed to the simulator in terms of power density per unit volume. The total dissipated power is assumed to be equal to 0.1 W [36] and the power density is obtained simply by dividing the dissipated power by the total volume of the active region:

$$P_{density} = \frac{P_{diss}}{V_{active}} = 3.7467 \times 10^{15}\; W/m^3 \tag{2.2}$$

The power density is kept constant in all the simulations in order to be able to directly compare the temperature for the different structures.

The boundary conditions are set in the heat source section of the simulator:

- an initial temperature of 293.15 K is set as initial condition in the whole simulation domain;

- the temperature is fixed to the ambient temperature (293.15 K) at the bottom surface of the device;
- all the other boundaries are assumed to be thermally insulating.

### Thermal conductivities

The two main parameters that affects the thermal behaviour of the device are the thermal conductivities of AlGaN, since it regulates the heat flow in the cavity, and of $HfO_2$ that influence mainly the heat flow through the DBR mirrors. $SiO_2$, even though is present close to the cavity has a thermal conductivity that is slightly varying around 1.4 $Wm^{-1}K^{-1}$ depending on thickness and deposition conditions, such that the thermal properties of the DBRs are dominated by the thermal conductivity of $HfO_2$.
In the case of AlGaN, the thermal conductivity is strongly dependent on the alloy composition. It can be calculated from the thermal conductivities of the binary compounds which forms the alloy (AlN and GaN), by a non-linear interpolation law [37]:

$$\kappa_{Al_xGa_{1-x}N} = \left[\frac{1-x}{\kappa_{GaN}} + \frac{x}{\kappa_{AlN}} + \frac{x\,(1-x)}{C_k}\right] \tag{2.3}$$

where the thermal conductivity of GaN is assumed to be $\kappa_{GaN}$=130 $Wm^{-1}K^{-1}$ and the thermal conductivity of AlN is set equal to $\kappa_{AlN}$=350 $Wm^{-1}K^{-1}$. The parameter $C_k$=3.2 $Wm^{-1}K^{-1}$ arises from the lattice disorder and it describes the random distribution of Ga and Al atoms in the lattice.
The trend of the thermal conductivity as a function of the Al composition is plotted in Figure 2.2. It presents a minimum around an Al molar fraction x=0.5 and it tends to the value of the binary compounds at the extremities. The drop of the thermal conductivity from the binary compounds values is due to the increasing scattering by acoustic phonons with increasing concentration of foreign atoms in the lattice, that acts as additional scattering centers reducing the overall thermal conductivity.
These calculated thermal conductivity values are the lowest values found in literature for the AlGaN alloy, thus the obtained simulations represents a worst case in term of AlGaN thermal conductivity.

The thermal conductivity of hafnium dioxide is strongly dependent on the thin-film thickness, which influence mainly the grain size of the poly-crystalline film, and on the substrate on which the thin film is deposited.
The thermal conductivity values found in literature ranges from 0.052 $Wm^{-1}K^{-1}$ for dielectric thin-films deposited by e-beam evaporation [38] to 17 $Wm^{-1}K^{-1}$ for $HfO_2$ in its bulk form [39]. The oxide layers in the DBR are deposited by sputtering, so in order to obtain results as realistic as possible the thermal conductivity of $HfO_2$ is set equal to $\kappa_{HfO_2}$=1.2 $Wm^{-1}K^{-1}$, corresponding to the measured value by *Lee et al.* [40] for $HfO_2$ thin-films deposited by DC magnetron sputtering.
All the dimensions of the layers and the thermal conductivity values of the different layers are summarized in Table 2.1.

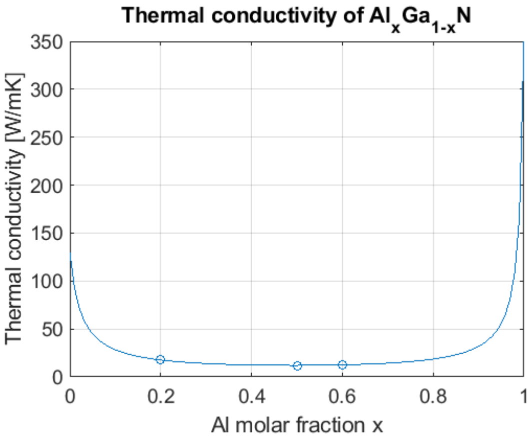

Figure 2.2: Thermal conductivity of AlGaN as a function of the aluminum composition.

| **Layer** | **Material** | **Diameter [µm]** | **Thickness [nm]** | $\kappa_{th}$ **[W/mK]** |
|---|---|---|---|---|
| Top DBR | $SiO_2/HfO_2$ | **82-302** | 900 | $\kappa_L$=1.4196<br>$\kappa_V$=1.312 |
| Top AlGaN | $Al_{0.6}Ga_{0.4}N$ | **80-300** | **210.6** | 12.5327 |
| Active region | $Al_{0.5}Ga_{0.5}N/$ $Al_{0.2}Ga_{0.8}N$ | **80-300** | 85 | $\kappa_L$=12.654<br>$\kappa_V$=12.459 |
| Bottom AlGaN | $Al_{0.6}Ga_{0.4}N$ | **80-300** | **33.4** | 12.1639 |
| Bottom DBR | $SiO_2/HfO_2$ | **80-300** | 990 | $\kappa_L$=1.3196<br>$\kappa_V$=1.312 |
| Hafnium dioxide (Bottom DBR) | $HfO_2$ | **80-300** | 24.4 | 1.2 |
| Aluminium | Al | **66-286** | 50 | 237 |
| Silicon dioxide | $SiO_2$ | **66-286** | 20 | 1.4 |
| Contact | Ti/Au/Ti | **66-286** | 520 | $\kappa_L$=305.65<br>$\kappa_V$=208.79 |
| Peripheral part of the contact | Au/Ti | 300 | 310 | $\kappa_L$=307.5<br>$\kappa_V$=220 |
| Substrate | Si | 300 | 300 000 | 130 |

Table 2.1: Simulation parameters for the double dielectric DBR structure. The values in bold text indicates the dimensions that are varied in the simulations performed as a function of the mesa width (80-300 µm) and AlGaN inner cavity thickness (329-8225 nm). For the diameter also the range of variation is indicated, while the thicknesses represents the initial values of the AlGaN cavity layers. All the dimensions not in bold text are kept fixed throughout all the simulations.

### Simulation results

The thermal performance of the structure under analysis is studied in terms of temperature profile and heat flow for different geometries.
As initial condition a pumped region of radius $r_{active}$=10 µm and a mesa of radius $r_{mesa}$=60 µm are considered. The temperature profile is shown in Figure 2.3. The arrows, in proportional scale, represents the heat flux. The maximum temperature achieved in the active region is of 559 K. This dramatically high temperature is a consequence of the double DBR configuration, whose really poor thermal conductivity inhibits the heat flow from the active region toward the substrate. Looking at the heat flow diagram (arrow plot), it can be observed that the dissipation occurs mainly laterally through the AlGaN cavity, whose thermal conductivity is low but higher than the one of the two DBR mirrors, and vertically through the bottom DBR mirror.

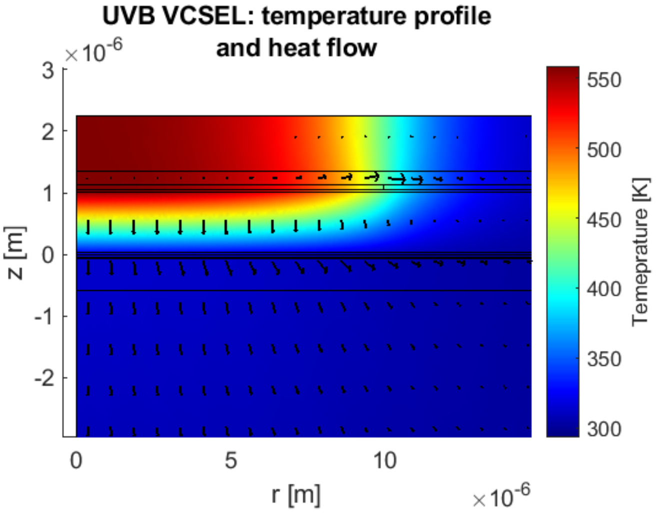

Figure 2.3: Temperature profile and heat flux in the UVB VCSEL with double DBR structure for $r_{active}$=10 µm and $r_{mesa}$=60 µm.

The simulation is then repeated iteratively by varying the design parameters and the effect in terms of maximum temperature in the cavity are studied as a function of different geometrical parameters:

- the active region radius is varied in the range 2.5 ÷ 25 µm. The active region is identified as the pumped region, related to the dimensions of the pumping laser beam. These simulations are mainly aimed at studing how much the VCSEL can be pumped before reaching dramatic temperatures in the cavity;
- the mesa radius iis varied in the range 40 ÷ 150 µm, to study the lateral heat flow mainly through the cavity layer toward the edges of the mesa;
- the cavity length is increased up to 25 times its initial value. Both the top or bottom AlGaN cladding layers are varied accordingly to investigate the heat spreading in the cavity.

**Influence of active region dimension** The simulations are run for increasing active region radius, keeping the mesa size and the inner cavity length fixed to their initial values

($r_{mesa}$=60 µm , $t_{cavity}$=329 nm). The active region is defined as a disk whose size is dependent on the dimension of the laser spot used to pump the VCSEL.

The active region radius is increased from 2.5 µm up to 25 µm and the pumped optical power density is kept constant to the value specified in equation (2.2). The corresponding plot is shown in Figure 2.4. Keeping the power density constant, a wider active region produces an increase in the total dissipated power in the cavity with a consequent increase in the maximum cavity temperature. This behaviour is confirmed by the simulations in which the temperature in the cavity shows a steep increase as the pumping region width increases up to approximately 10 µm, while it shows a sort of saturation for bigger active region sizes. The saturation of the maximum temperature at bigger pumped region width reflects the fact that the heat transport is enhanced for wider contact areas.

The thermal resistance is a figure of merit of the whole device used to describe the ability of a homogeneous material to conduct the heat. It is calculated as the ratio between the increase in temperature in the cavity with respect to the initial temperature (293.15 K) and the total dissipated power:

$$R_{th} = \frac{\Delta T}{P_{diss}} \tag{2.4}$$

The calculation is repeated for increasing active region width and the resulting plot is shown in Figure 2.5. Keeping the dissipated power density constant, an increase in the active region width produces an increase in the total dissipated power. Thus, the thermal resistance reduces with increasing active region size. This results is not straightforward. In fact, one would expect a raise in the thermal resistance for wider active regions, since an increase in the dissipated power leads to an increase in the cavity temperature. The observed behaviour is the opposite and it is an indication of the fact that a bigger surface area enhances the heat dissipation. The increase in temperature with the active region size is then smaller than the increase in dissipated power, with a consequent reduction of the thermal resistance. In conclusion, the heat dissipation is more efficient for bigger active regions, but the temperature reached in the cavity is still too high.

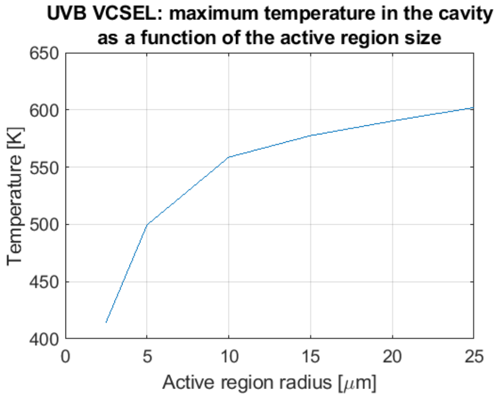

Figure 2.4: Maximum temperature in the cavity as a function of the active region radius for the double DBR configuration.

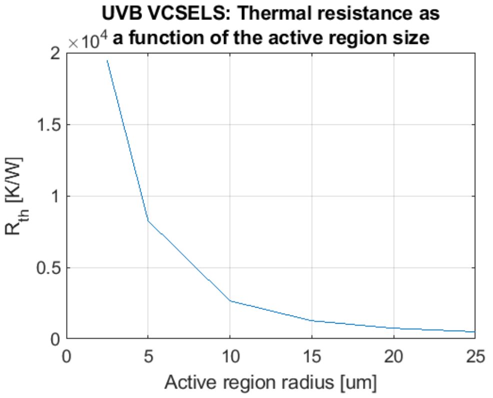

Figure 2.5: Thermal resistance as a function of the active region radius for the double DBR configuration.

**Influence of mesa size** The thermal behaviour of the VCSEL as a function of the mesa radius is now studied. The active region radius is kept fixed at $r_{active}$=10 µm. Looking at the

temperature profile in the structure simulated at the fixed simulation parameters reported in Figure 2.3, it can be observed that the reduction in temperature occurs in few micrometers at the borders of the active region. Thus, being that the mesa size is relatively big compared to the active region width, the temperature reduction is expected to not be significantly dependent on the mesa dimensions. The predicted behaviour is confirmed by the simulations, in which the mesa radius is varied in the range 40 ÷ 150 µm. The results of the simulation are plotted in Figure 2.6: a decrease in the maximum temperature reached in the cavity is observed for smaller mesas and the trends saturates for bigger mesa sizes, but the obtained reduction in temperature is not significant. A maximum reduction in temperature of 0.0387 K is observed by increasing the mesa radius from 40 µm to 150 µm.
The trend of the thermal resistance as a function of the mesa size is plotted in Figure 2.7. Also in this case, no significant dependence on the mesa size is observed since the reduction in temperature with increasing diameter of the mesa is not effective.

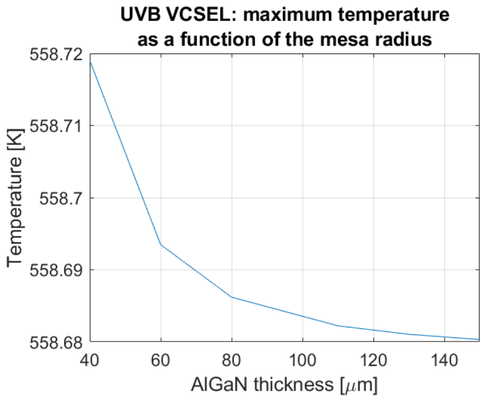

Figure 2.6: Maximum temperature in the cavity as a function of the mesa radius for the double DBR configuration, for $r_{active}$=10 µm.

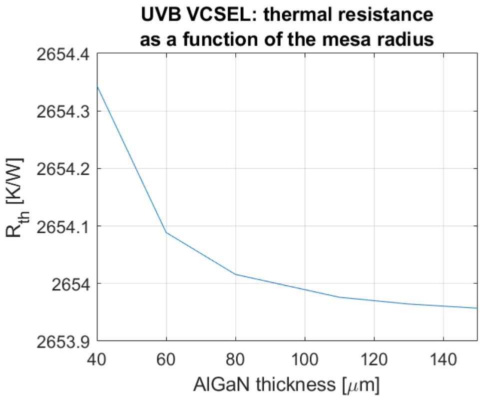

Figure 2.7: Thermal resistance as a function of the mesa radius for the double DBR configuration, for $r_{active}$=10 µm.

**Influence of cavity length** The last simulation is devoted to the study of the effects of the cavity length on the thermal behaviour of the device. A shorter cavity is preferable to have single-longitudinal mode operation, a better longitudinal optical confinement factor and lower absorption loss, but at the same time it leads to a reduction in the heat dissipation capability. A longer cavity will produce a more effective spreading of the heat reducing the maximum temperature achieved in the active region.
In the simulations the cavity length is increased by increasing either the top or bottom AlGaN cladding layers. The AlGaN cavity is increased up to 25 times the nominal value reported in Table 2.1.
The results of the simulation are shown in Figure 2.8. It can be observed that the curve obtained by varying the top AlGaN shows a monotonically decreasing behaviour with increasing cavity length, while the one obtained varying the bottom AlGaN layer saturates at longer cavity lengths. In the first case, the active region is kept closer to the bottom DBR and the path the heat has to travel from the active region toward the substrate is smaller, thus producing a more effective reduction in temperature.

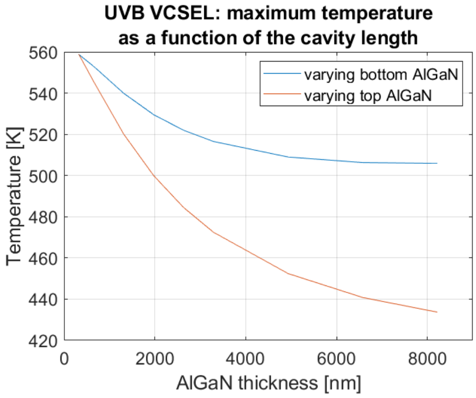

Figure 2.8: Maximum temperature in the cavity as a function of the cavity length for the double DBR configuration. The two curves are obtained by varying separately the bottom and the top AlGaN cladding layers of the cavity.

In Figure 2.9 and 2.10 the thermal resistance as a function of the cavity length is plotted varying the top and bottom AlGaN layer, respectively. The trend of the thermal resistance follows the behaviour of the temperature in the cavity and it is an indication of the better thermal behaviour of the system for longer cavity lengths. Thus, the most effective way to reduce the temperature in the cavity and achieving a better dissipation of heat is achieved by varying the top AlGaN cladding layer.

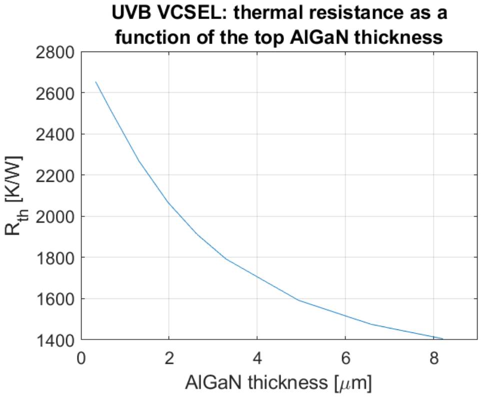

Figure 2.9: Thermal resistance as a function of the cavity length for the double DBR configuration, obtained by varying the top AlGaN cladding layer.

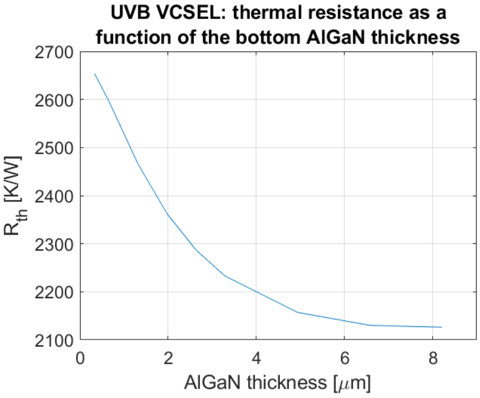

Figure 2.10: Thermal resistance as a function of the cavity length for the double DBR configuration, obtained by varying the bottom AlGaN cladding layer.

### Comparison with epitaxial bottom DBR

It is interesting to compare the obtained results for the double DBR configuration with a structure in which the bottom DBR is epitaxially grown, in order to have an idea of how much the thermal performance of the device is worsened in the first case.

The advantage of a dielectric DBR is in the superior optical properties. The high refractive index difference between $HfO_2$ and $SiO_2$ allows to reach high reflectivity over a wide range of wavelengths and reduced number of DBR pairs. The use of an epitaxial DBR is characterized by better thermal performance, due to the higher thermal conductivity of the materials with respect to the dielectric $SiO_2/HfO_2$ DBR, but the optical properties are not optimal, in terms of reduced reflectivity and narrower stop-band.

The epitaxial DBR used in the simulation is composed by an alternating stack of AlN ($37.2\,nm$) and $Al_{0.6}Ga_{0.4}N$ (33.9 nm) layers. Due to the relatively small refractive index difference between the materials which composes the DBR layers a higher numbers of $AlN/Al_{0.6}Ga_{0.4}N$ pairs are required to achieve high reflectivity. A reasonable choice is to use 40 pairs, although even in this case a $\sim 99\%$ of reflectivity is difficult to achieve [41].

The thermal conductivities of the materials are taken from literature values. The thermal conductivity of epitaxially grown AlGaN is modelled as for the cavity by means of the non-linear interpolation law reported in equation (2.3). The thermal conductivity of AlN is set equal to 200 $Wm^{-1}K^{-1}$ [42].

It is worth to notice that the AlN cannot be grown on top of gold or silicon. Thus, the silicon carrier is replaced by a sapphire substrate, with a 300 nm thick layer of AlN on top [43]. All the other simulation parameters are kept equal to the previous simulations.

The temperature profile and the heat flow for an active region radius $r_{active}$=10 µm and a mesa radius of $r_{mesa}$=60 µm are shown in Figure 2.11. Compared to the previous design the total temperature in the cavity is drastically reduced achieving a maximum temperature of 361 K. The high thermal conductivity of the AlN layers in the epitaxial DBR acts as heat spreaders increasing the lateral heat flow through the bottom DBR.

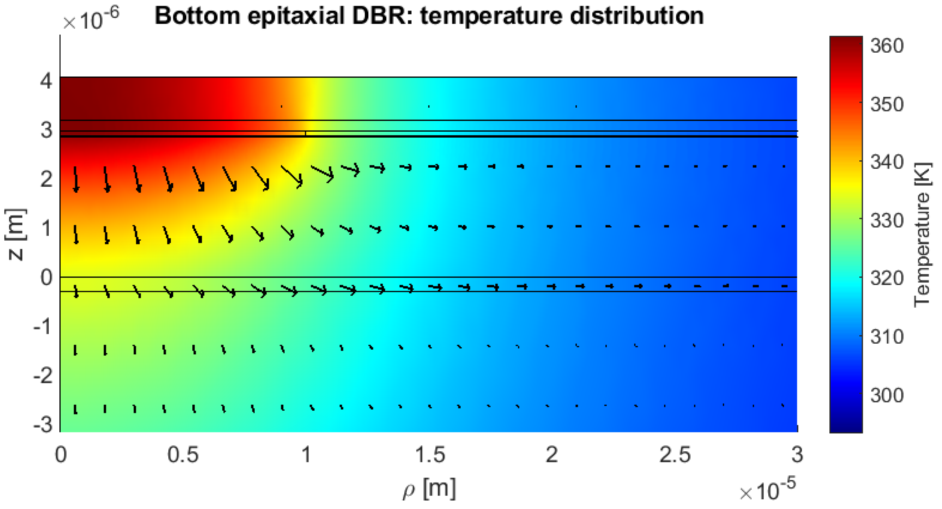

Figure 2.11: Temperature profile and heat flow in the VCSEL with bottom epitaxial DBR.

### 2.1.2 Recessed metal design: addition of a thermal shunt ring

The main problem related to the uninterrupted double dielectric DBR structure is that there is no high thermal conductivity material in contact with the cavity and the heat flow toward the heat sink is reduced, causing a dramatic increase in the cavity temperature.

In order to improve the heat dissipation one solution is to add a thermal shunt ring in order to put a metal with high thermal conductivity closer to the active region [28]. The thermal shunt is inserted by etching a ring in the bottom DBR structure before the flip-chip procedure, in which the inner ring of the shunt is put in correspondence of the perimeter of the active region in order to do not influence the optical field in the cavity.

The structure under analysis is shown in Figure 2.12. After the etching of the thermal shunt ring the Al/$SiO_2$/Ti/Au contact layers are deposited on the bottom DBR. The obtained structure will be flip-chip bonded to the 300 nm thick Au contact previously deposited on the silicon substrate. Thus, an air gap will remain trapped in the thermal shunt ring, that will not be completely filled with metal. In the obtained structure the Al layer is directly in contact with the cavity, reducing the path for the heat to flow from the active region to the substrate.

Different modifications are then investigated in order to try to improve the thermal performance:

- removal of the $SiO_2$ layer;
- removal of the Al layer;
- filling the air gap with gold.

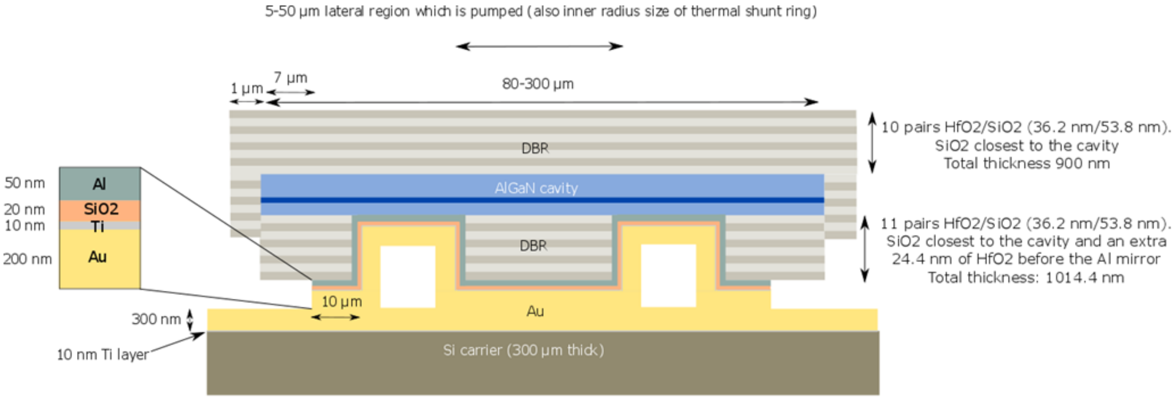

Figure 2.12: UVB-VCSEL structure with a thermal shunt ring.

### Comparison with uninterrupted bottom DBR

The simulations performed for the structure with the uninterrupted bottom DBR are repeated in the case of the structure with the thermal shunt and the obtained results are compared between the two structures in terms of temperature decrease and thermal resistance as a function of active region size, mesa dimension and cavity length.

The first simulation is run at fixed simulation parameters, for an active region of radius 10 μm and a mesa of radius 60 μm. The temperature distribution in the structure is shown in Figure 2.13. The presence of the air gap in the shunt inhibits the heat flow, thus the heat is mainly dissipated through the gold ring closest to the active region. A temperature reduction of 2 K is achieved with the introduction of the thermal shunt.

**Influence of active region dimension** The simulation is run by increasing the active region radius in the range 2.5 ÷ 20 μm. The shunt inner ring is placed in correspondence of

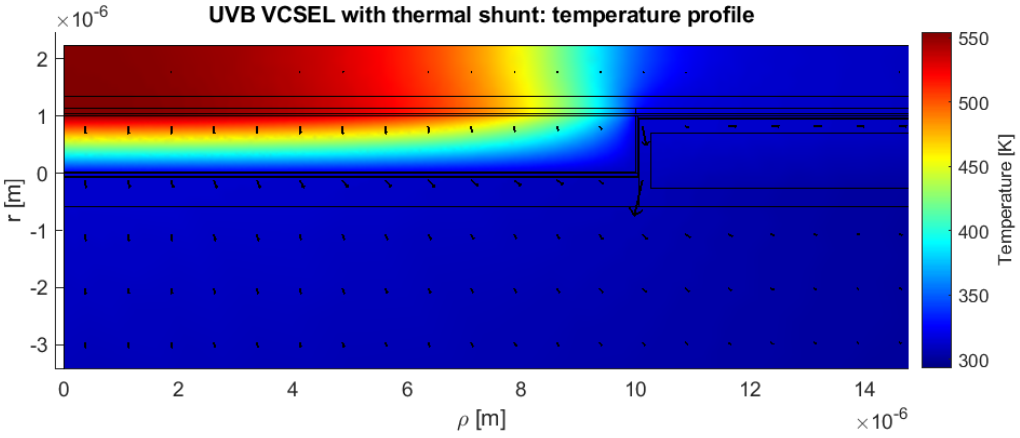

Figure 2.13: Temperature profile in the VCSEL in the recessed metal design, for an active region of radius $r_{active}$=10 µm and a mesa radius of $r_{mesa}$=60 µm.

the active region boundary and its size is also increased during the simulation.
In Figure 2.14 the maximum temperature in the cavity as a function of the active region size is reported. It can be observed that the effect of the thermal shunt is more effective for smaller pumped region sizes, so for smaller injected power, reaching maximum reduction in temperature of 42 K for an active region of radius 2.5 µm. For bigger sizes of the pumped region the reduction in temperature with the addition of the thermal shunt appears to be not effective. The minimum reduction in temperature occurs for an active region of radius 20 µm and it corresponds to a decrease in temperature in the thermal shunt structure of only 1.3 K with respect to the temperature achieved in the uninterrupted DBR structure.

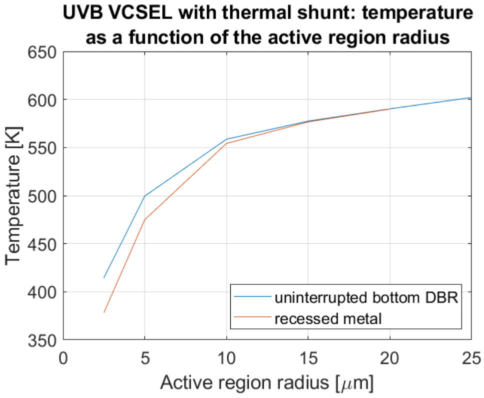

Figure 2.14: Comparison between the maximum temperature in the cavity as a function of the active region radius with and without the thermal shunt ring.

**Influence of mesa size** The simulation is run by varying the mesa radius in the range 40÷ 150 µm. The results of the simulation are shown in Figure 2.15 and Figure 2.16, in terms of maximum temperature and temperature increase in the cavity. The calculations are also are compared with the results for the uninterrupted bottom DBR design analysed in Section

2.1.1.

The results shows that in the structure with the thermal shunt ring the maximum temperature in the cavity actually increases with increasing mesa width. This behaviour is due to the presence of the air gap. Air is characterized by a very poor thermal conductivity (0.02527 $Wm^{-1}K^{-1}$), so the heat is mainly conducted through the gold metallic layer around the air gap. When the mesa size is increased, the outer gold ring is moved away from the active region boundary reducing the section of the region through which the heat can flow. The maximum temperature increase is still not significant, and that confirms the initial hypothesis according to which the heat is mainly dissipated in the vertical direction through the bottom DBR.

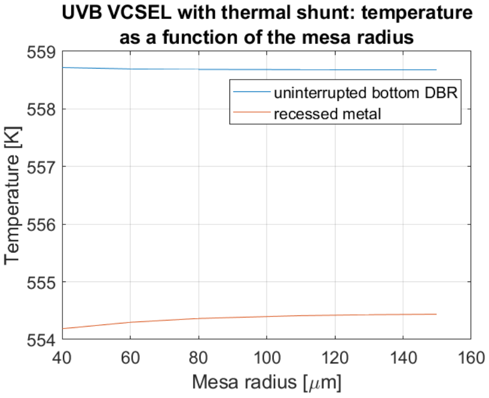

Figure 2.15: Comparison between the maximum temperature in the cavity as a function of the mesa radius in the UVB VCSEL structure with and without the thermal shunt ring.

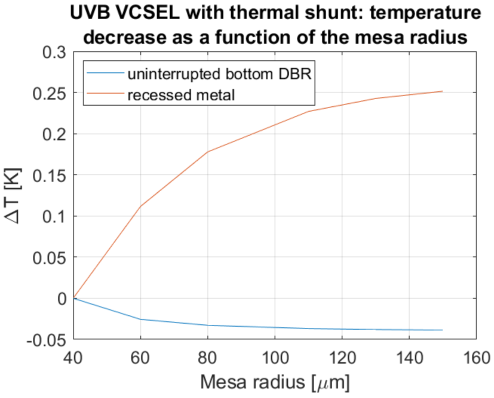

Figure 2.16: Comparison between the maximum temperature decrease in the cavity as a function of the mesa radius in the UVB VCSEL structure with and without the thermal shunt ring.

**Influence of the cavity length** The last simulation is performed for increasing cavity length. The cavity length is varied by either increasing the top and bottom AlGaN layers. The thickness of the cladding layers of the cavity are increased up to 25 times their nominal value reported in Table 2.1.

The results are plotted in Figure 2.17 and Figure 2.18. The most effective way to reduce the cavity temperature is to vary the top AlGaN cladding layer, keeping in this way the active region closer to the metallic contact of the shunt.

### Removal of $SiO_2$/Al layer

In the structure with the thermal shunt an Al/$SiO_2$/Au metal stack is deposited on the bottom DBR before flipping the structure and bonding it to the bottom gold contact deposited on the Si carrier. The effects of the removal of Al and $SiO_2$ layers are investigated in this section. The presence of the $SiO_2$ layer, due to its small thermal conductivity ($\kappa_{th,SiO_2}$=1.4 $Wm^{-1}K^{-1}$), prevents the heat to flow toward the gold contact. The removal of the oxide layer

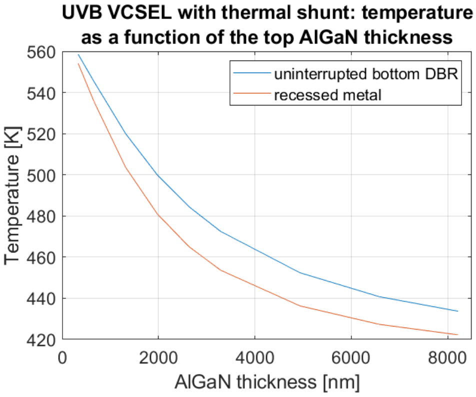

Figure 2.17: Comparison between the maximum temperature in the cavity as a function of the AlGaN thickness in the UVB VCSEL structure with and without the thermal shunt ring, varying the top AlGaN cladding layer.

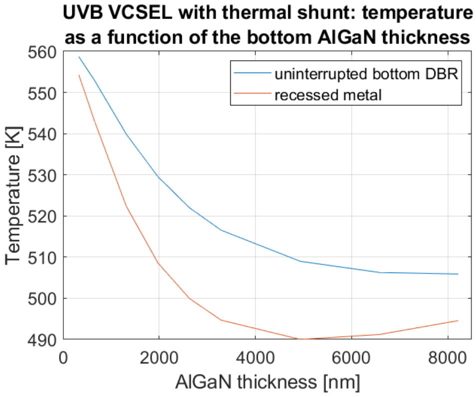

Figure 2.18: Comparison between the maximum temperature in the cavity as a function of the AlGaN thickness in the UVB VCSEL structure with and without the thermal shunt ring, varying the bottom AlGaN cladding layer.

is then expected to improve the thermal performance of the device reducing the maximum temperature achieved in the cavity. Without the oxide the cavity is directly in contact with the metallic contact which is characterized by a high thermal conductivity and the maximum temperature in the cavity is expected to reduce.

The Al layer is used for its high reflectivity to increase the total reflectivity of the bottom mirror. The presence of Al allows for using a lower number of layers in the bottom DBR ensuring at the same time a high reflectivity. The simulation is run by simply removing the Al layer without increasing the bottom DBR thickness. The results of the simulation are shown in Figure 2.19-2.23. The removal of the oxide layer actually improves the thermal performance of the device reducing the maximum temperature achieved in the cavity. The removal of the Al does not introduce significant differences, since the thermal conductivities of Al and Au are comparable and heat is dissipated efficiently. Therefore, the presence of the Al does not affect the thermal behaviour of the device. On the contrary, the removal of the Al layer would require an increase in the bottom DBR thickness, actually worsening the thermal performance of the device.

### Filling the thermal shunt with gold

In the recessed metal design, the air ring present in the shunt actually reduces the effective thermal conductivity of the shunt, due to the poor thermal conductivity of air (0.02527 $\mathrm{Wm^{-1}K^{-1}}$ at 300 K). An improvement of the structure involves filling the air gap with gold in order to enhance the heat dissipation toward the substrate.

The results of the simulation are reported in Figure 2.24. The temperature appears to be reduced of 2 K at fixed simulation parameters ($r_{active}$=10 µm, $r_{mesa}$=60 µm) with respect to the initial structure. Thus, the recessed metal design, either with the air gap or completely filled with Au, is not an effective solution to improve the heat dissipation in the UVB VCSEL structure with double dielectric DBR.

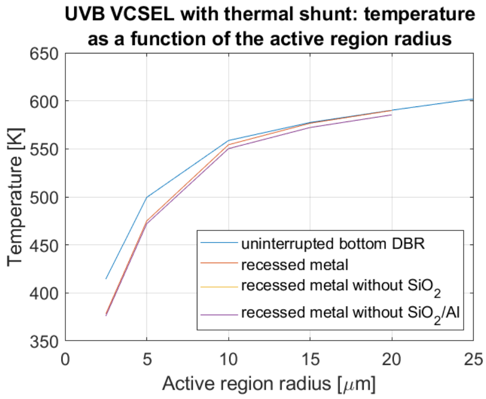

Figure 2.19: Comparison between the maximum temperature in the cavity as a function of the active region radius with and without the thermal shunt ring.

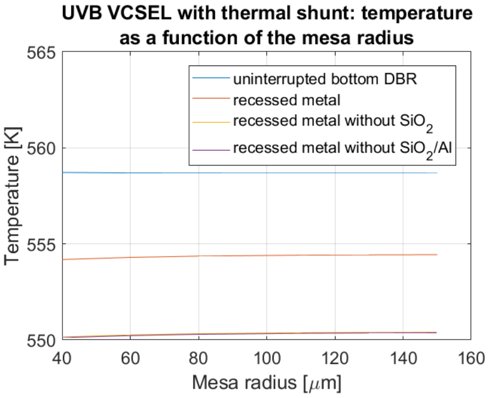

Figure 2.20: Comparison between the maximum temperature in the cavity as a function of the mesa radius with and without the thermal shunt ring.

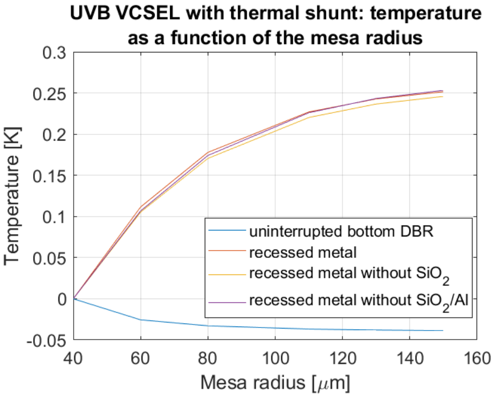

Figure 2.21: Comparison between the maximum temperature decrease in the cavity as a function of the mesa radius with and without the thermal shunt.

### Heat spreading layer

Due to the poor control on the thermal performance by using standard thermal management techniques, an alternative structure including an high thermal conductivity heat spreading layer in the cavity placed between the top AlGaN cavity contact and the top DBR is now investigated.
The choice of the materials is a critical challenge in this case. In fact, as the heat spreader is in contact with the cavity the material used affects directly the resonance of the radiation in the resonator and so the distribution of the optical field. In particular, two main requirements must be satisfied for a good heat spreader:

- high lateral thermal conductivity;
- transparency in the UV range.

As material of choice two different options are studied in the following: AlN, which is not absorbing at 320 nm and characterized by a high thermal conductivity if epitaxially deposited,

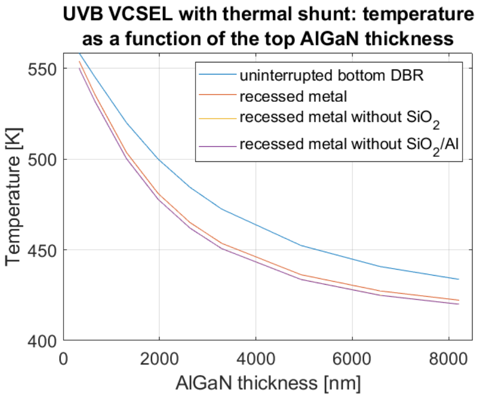

Figure 2.22: Comparison between the maximum temperature in the cavity as a function of the top AlGaN cladding layer thickness with and without the thermal shunt ring.

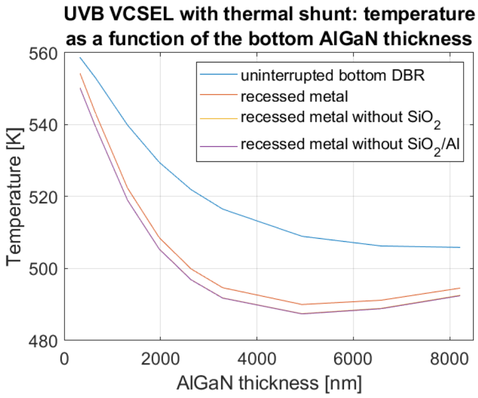

Figure 2.23: Comparison between the maximum temperature in the cavity as a function of the bottom AlGaN cladding layer thickness with and without the thermal shunt ring.

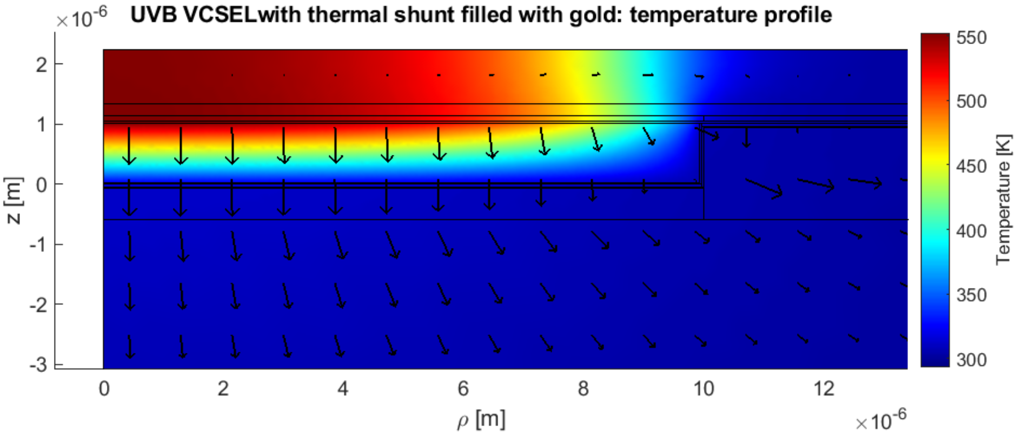

Figure 2.24: Temperature profile in the VCSEL in the recessed metal design with the thermal shunt filled with Au, for an active region of radius $r_{active}$=10 µm and a mesa radius of $r_{mesa}$=60 µm.

and CVD diamond films, quite expensive technology but with superior thermal characteristics and very low absorption in the UVB range due to the wide bandgap of diamond.

**Alluminum nitride** AlN is characterized by a really high thermal conductivity even in thin-film form ($\sim$ 200 Wm$^{-1}$K$^{-1}$ [36]). This property makes it a really promising material for thermal management applications. The presence of a thin-film of AlN in contact with the cavity enhances the lateral heat spreading toward the side of the mesa drastically decreasing the maximum temperature reached in the cavity.

In Figure 2.25 the thermal profile of the structure with an AlN layer of thickness 250 nm is shown. The heat flow is represented by the arrow plot (in proportional scale), showing that the heat transport is mainly conducted through the high thermal conductivity AlN layer, so that the importance of the bottom DBR from a thermal perspective is reduced.

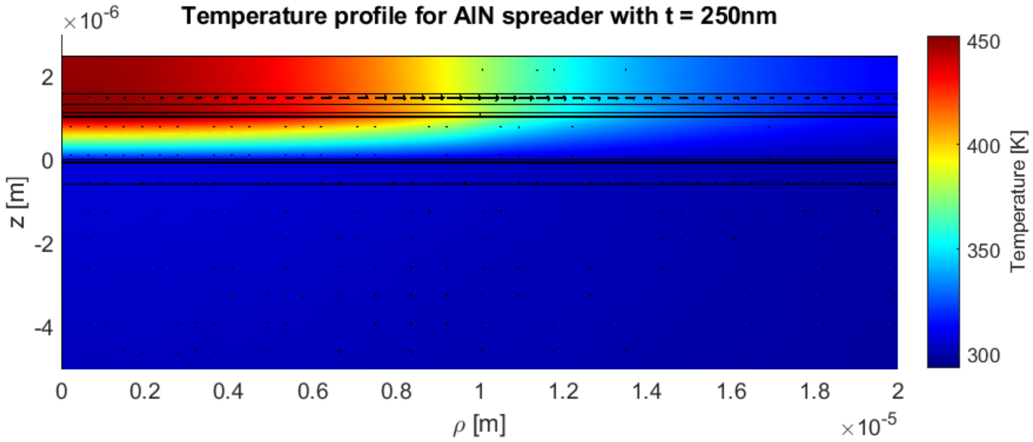

Figure 2.25: Temperature profile and heat flux in the UVB VCSEL structure with a 250 $nm$ thick AlN heat spreading layer.

In figure 2.26 the maximum temperature in the cavity achieved by increasing the AlN spreading layer from 50 nm up to 600 nm is represented. By adding the AlN heat spreading layer the temperature in the cavity is reduced, but a relatively thick layer of AlN is required to achieve reasonably low values of temperature with a consequent reduction in the optical performance.

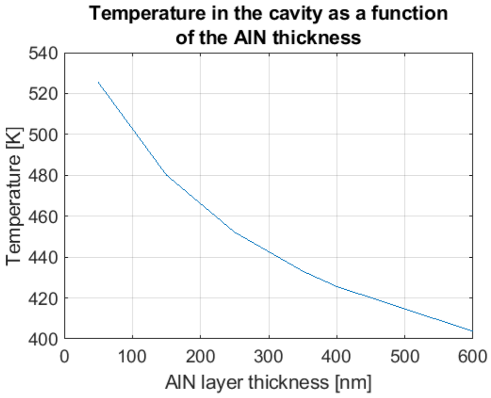

Figure 2.26: Influence of the AlN heat spreader: maximum temperature in the cavity as a function of the AlN heat spreading layer thickness.

**CVD diamond films** As alternative material to AlN as heat spreading layer for UVB VCSELs application a thin diamond film is investigated. Diamond has a nominal energy gap of 5.5 eV making it transparent to UV radiation and a really high thermal conductivity value, which exceed 2000 $Wm^{-1}K^{-1}$ in its bulk form.

High quality diamond thin-films can be easily produced and integrated into a VCSEL cavity by direct deposition of the film by CVD or bonding of thin diamond wafers. The thermal conductivity of CVD diamond is certainly reduced compared to the thermal conductivity value of bulk diamond, but it is still sufficiently high to be considered a good candidate as heat spreader ($\kappa_{th} \sim 800$ Wm$^{-1}$K$^{-1}$ [44]).

In Figure 2.27 the temperature profile and the heat flux in the UVB VCSEL structure with a 250 nm thick diamond layer is shown. Even for a thin layer the lateral heat spreading toward the edge of the mesa is efficient. The lateral heat flow is enhanced as the thickness of the diamond layer is increased, reaching sufficiently low temperature for a thickness of 600 nm (figure 2.28).

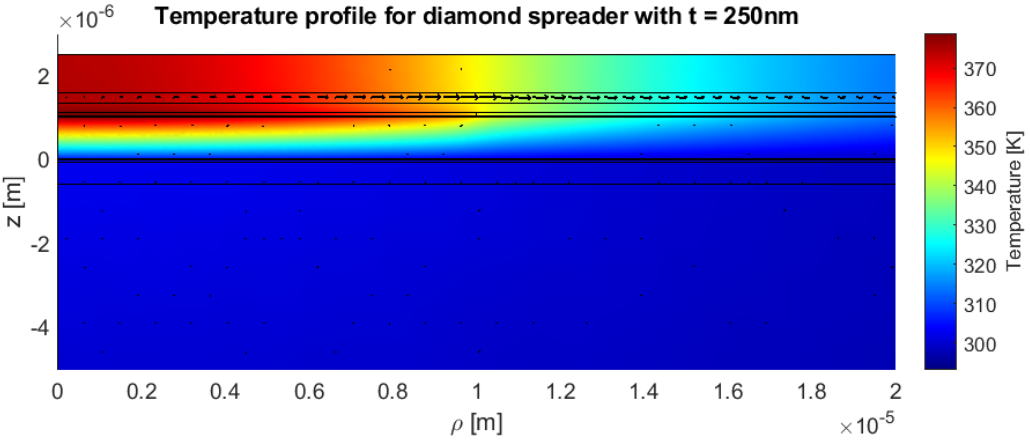

Figure 2.27: Temperature profile and heat flux in the UVB VCSEL structure with a 250 $nm$ thick diamond heat spreading layer.

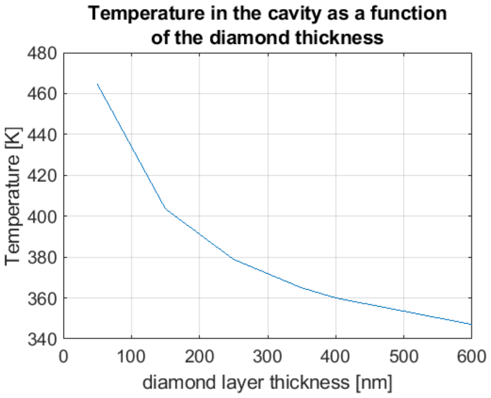

Figure 2.28: Influence of the diamond heat spreader: maximum temperature in the cavity as a function of the diamond heat spreading layer thickness.

## 2.2 UVC Vertical-Cavity Surface-Emitting Lasers (VCSELs)

The thermal behaviour of deep-UV VCSELs emitting in the UVC range, are studied in this section. The structure is analogous to the one used for the UVB-emitting lasers and composed by a double dielectric DBR design with the cavity completely enclosed between the DBR stacks. It is composed by a $2.5\lambda$ long aluminium nitride cavity, and an active region consisting of five QWs ($Al_{0.7}Ga_{0.3}N/Al_{0.3}Ga_{0.7}N$) designed to emit at 275 nm. Both the bottom and top DBR are composed by a stack of ten pairs of $SiO_2/HfO_2$(45.82 nm/29.88 nm), where the $SiO_2$ is in contact with the cavity. For the bottom DBR an additional $SiO_2/HfO_2$ (45.82 nm/48.3 nm) pair is added before the Al mirror to adjust the phase for the reflection on the Al layer. The final epitaxial structure is summarized in Table 2.2.

| **Layer** | **Material** | **Diameter [$\mu$m]** | **Thickness [nm]** | $\kappa_{th}$ **[W/mK]** |
|---|---|---|---|---|
| Top DBR | $10\times SiO_2/HfO_2$ | 121 | 757 | 1.3 |
| Cathode | *AlN* | 120 | 120.4 | 200 |
| Active region | $Al_{0.7}Ga_{0.3}N/$ $Al_{0.3}Ga_{0.7}N$ | 120 | 111.2 | 14.3 |
| Anode | AlN | 120 | 60.1 | 200 |
| Bottom DBR | $11\times SiO_2/HfO_2$ | | 757 | 1.3 |
| Aluminum mirror | Al | 113 | 202 | 237 |
| Silicon dioxide | $SiO_2$ | 113 | 20 | 1.4 |
| Titanium | Ti | 113 | 10 | 21.9 |
| Gold contact | Au | 113<br>600 | 200<br>300 | 317<br>317 |
| Titanium | Ti | 600 | 10 | 21.9 |
| Carrier | Si | 600 | 300 000 | 130 |

Table 2.2: Simulation parameters for the UVC-VCSELs design.

As in the previous case, both the active region and the DBRs are modeled as effective layers of anisotropic thermal conductivity, calculated as expressed in (2.1). Calculations shows that for both the materials the thermal conductivity can be considered isotropic.
The dissipated power in the active region is considered to be equal to 0.1 W for a pumped region of 10 µm, the power density is calculated accordingly by dividing the total dissipated power by the active region volume:

$$P_{density} = 2.8640 \times 10^{15}\, W/m^3 \tag{2.5}$$

Due to the slightly smaller power density with respect to the UVB VCSEL structure, the temperature can not be directly compared with the previous configuration. The better thermal performance can be indeed studied in therms of thermal resistance.
The heat sources are placed in the active region and the power density is kept fixed in all the different simulations.
As boundary conditions the following rules are imposed:

- an initial temperature of 293.15 K is set on the whole simulation domain;

- a fixed temperature of 293.15 K is set on the bottom surface of the silicon carrier;
- thermal insulation on all the other boundaries.

**Simulation results**

The heat flow and the temperature profile in the structure are studied.
In Figure 2.29 the temperature distribution in the device for a 2.5$\lambda$ cavity is shown, the arrow plot (in proportional scale) represents the heat flow. It can be observed that the temperature in the cavity is drastically reduced due to the presence of AlN cladding layers which acts as heat spreaders increasing the lateral heat transport toward the edge of the mesa. In this case, a thermal conductivity of $\kappa_{th}$=200 $\mathrm{Wm^{-1}K^{-1}}$ is used for AlN [36]. The value of the thermal conductivity is reduced with respect to the bulk value (i.e. 350 $\mathrm{Wm^{-1}K^{-1}}$) due to the small dimensions of the AlN cavity external layer, so that the thin-film value is used.

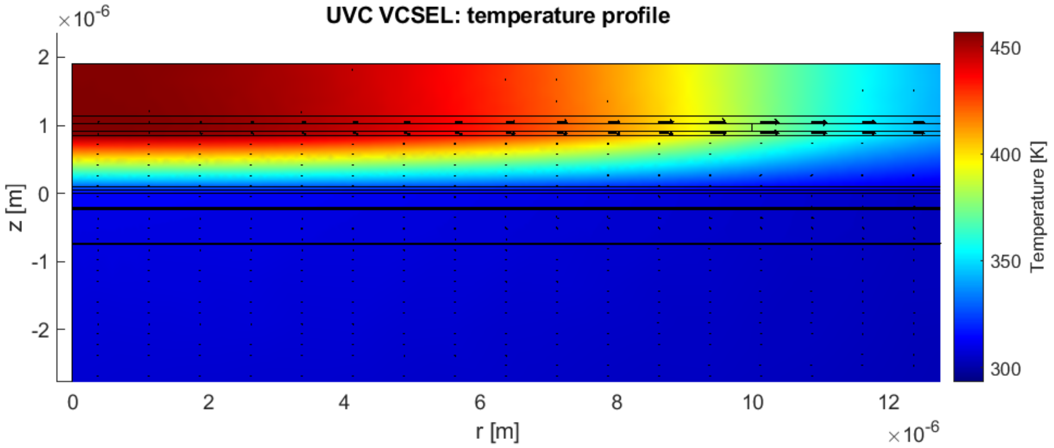

Figure 2.29: Temperature distribution and heat flow in the UVC-VCSEL design for a 2.5$\lambda$ cavity.

The temperature can be further reduced by increasing the cavity length, as shown in figure 2.30. As the cavity is increased the temperature in the active region drastically reduces.
The better thermal performance of the UVC design can be observed by comparing the thermal resistance with to the one obtained for the UVB design (Section 2.1.1). The thermal resistance as a function of the cavity length is shown in Figure 2.31. In the UVC VCSEL design, with AlN-based cavity, the thermal resistance results to be halved with respect to the UVB design. This is an indication of the big influence the thermal conductivity of the cavity layer material have on the heat dissipation properties of the structure.
In contrast to the behaviour observed in the UVB design, in this case the reduction in temperature by varying the cathode or the anode is comparable. This is an indication of the fact that, as the thermal conductivity of the cavity is increased, the main dissipation mechanism is the lateral heat spreading in the cavity.

As already introduced in the previous section, the aluminium layer under the bottom DBR is used to enhance the reflectivity of the bottom mirror allowing for using a reduced number of pairs in the bottom DBR. The removal of the Al layer is now studied. For that purpose in order to achieve a high reflectivity required for the bottom mirror the DBR pairs

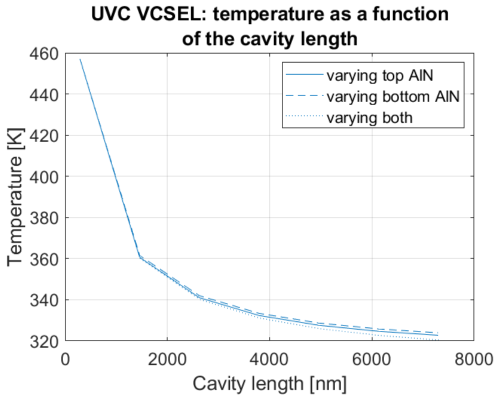

Figure 2.30: Maximum temperature in the cavity as a function of the cavity length for the UVC-VCSEL design.

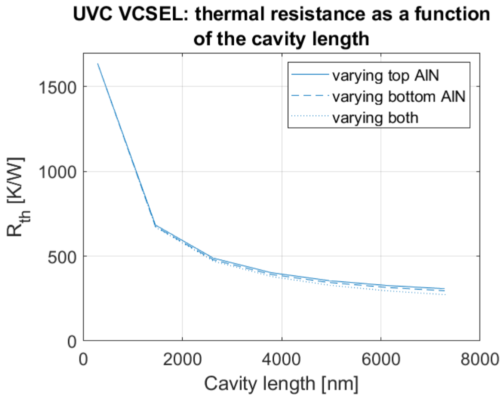

Figure 2.31: Thermal resistance as a function of the cavity length for the UVC-VCSEL design.

are increased to fifteen.

As shown in Figure 2.32, where the temperature profile in the design without Al layer is represented, the temperature behaviour is dramatically worsened. The increase of the bottom DBR thickness reduces the vertical heat flow toward the substrate resulting in an increase in the temperature reached in the active region. The worsening of the performance can be studied in term of thermal resistance, which is increased by 15%.

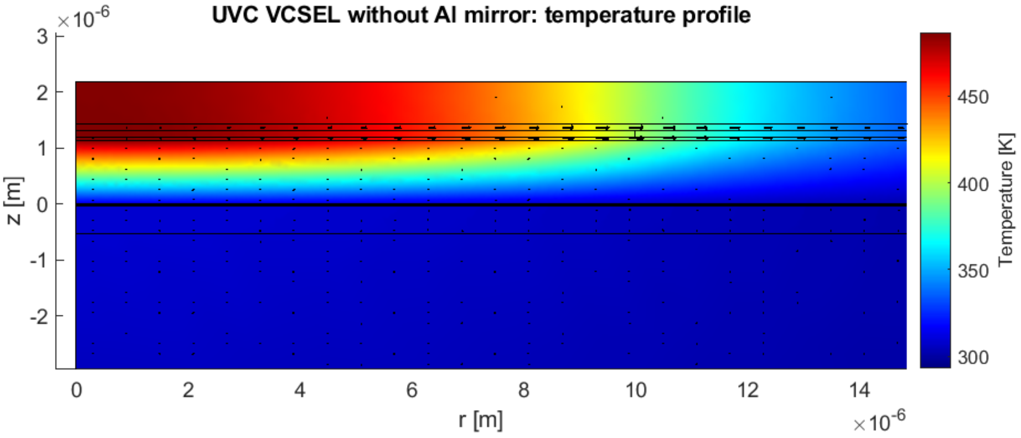

Figure 2.32: Temperature distribution and heat flow in the UVC-VCSEL design for a 2.5$\lambda$ cavity without the Al layer.

An increased cavity length is therefore required in this design in order to reach a reasonable temperature in the cavity. The study of the maximum temperature and thermal resistance as a function of the cavity length are reported in Figures 2.33 and 2.34. As the cavity length increases the main heat transport mechanism occurs in the lateral direction through the AlN cavity and the reduction of the thermal performance due to the presence of the thicker bottom DBR is attenuated. So that the temperature reached in the active region for a longer cavity is approximately equal to the one achieved for the design with the Al layer. The simulations are implemented by varying either the cathode or anode side of the cavity. As in the case of UVB VCSELs, the increase of the top side of the cavity will produce a more effective heat spreading. However, in this case the decrease in temperature is limited to few Kelvins and this reduction is more effective for longer cavities. This behaviour leads to the conclusion that the material in the cavity plays a major role in the heat spreading capabilities of the device. In fact, being AlN much more thermally conductive then AlGaN, it acts as a heat spreading layer enhancing the heat flow in the lateral direction.

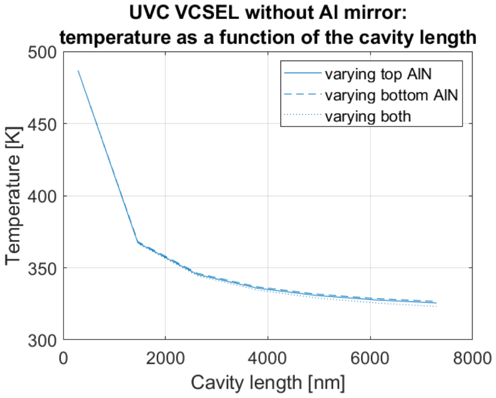

Figure 2.33: Maximum temperature in the cavity as a function of the cavity length for the UVC-VCSEL design without the Al layer.

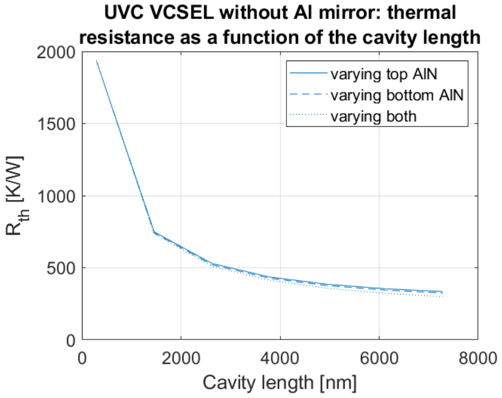

Figure 2.34: Thermal resistance as a function of the cavity length for the UVC-VCSEL design without the Al layer.

## 2.3 UVB thin-film flip-chip LEDs

In this section the thermal characteristics of UVB-emitting light-emitting diodes is studied. UV-LEDs have gained a lot of attraction in the last few years due to the wide range of applications in which they can be employed, such as UV curing, water purification and gas sensing.

Thanks to the thin-film technology, in which the active region is composed by an epitaxially deposited stack of quantum wells, the output performance of such devices has experienced a boost. In fact, in thin-film devices the edge region becomes a negligible fraction of the area of the LED, resulting in an enhanced collection efficiency [45]. Moreover, being the dimensions reduced, the photons travels a shorter path inside the device so that the reabsorption of light is minimized.

Here, UVB-emitting thin-film LEDs, realized in a flip-chip technology are studied. The thin-film design is implemented as in the case of VCSELs by substrate removal through electrochemical etching of an AlGaN-based sacrificial layer. In such way, the top surface is completely exposed increasing the emission surface area and resulting in a better power conversion efficiency. In the case of LEDs, in general a single sacrificial layer is composed of $\mathrm{Al_{0.37}Ga_{0.63}N}$ is used.

First, a simple two-dimensional simulation is performed to study in first approximation the thermal behaviour of the device. Then, 3D simulations are implemented in COMSOL Multiphysics in order to simulate more complex structures in which both the mesa and the contacts are realized in a fin-shape for a better current spreading.

### 2.3.1 2D simulations

The structure considered in the following is an AlGaN based device with a square-shaped mesa (Figure 2.35). The epitaxial structure with relative composition and thicknesses of the different layers is summarized in Table 2.3. The active region is composed by three $\mathrm{Al_{0.21}Ga/Al_{0.33}GaN}$ quantum wells emitting in the UVB-range with a peak wavelength of 310 nm. A passivation dielectric layer 500 nm-thick is then deposited by sputtering or Plasma-Enhanced Chemical Vapor Deposition (PECVD) of $\mathrm{SiO_2}$ to stabilize the mesa after the ECE and passivate the sidewalls.

The active region is modeled as in the case of the VCSELs structure as an effective layer with anisotropic thermal conductivity, calculated according to equation (2.1). All the other layers have been considered separately with the nominal thermal conductivity of the material composing the structure as summarized in Table 2.3.

The thicknesses of the device with respect to the thickness of the substrate allows to lump all the heat sources in the active region. Due to the lack of measurements for the UV-LEDs the total dissipated power is taken from [46] by simply subtracting the measured optical output power from the electrical input power in the device. The obtained power density is calculated accordingly by dividing the total dissipated power by the total active region volume:

$$P_{diss} = 0.159W \rightarrow P_{density} = 7.3944 \times 10^{13} W/m^3 \tag{2.6}$$

Notice that the so calculated power density is kept constant for all the different designs in order to be able to compare the different heat dissipation capabilities.

The following boundary conditions are used:

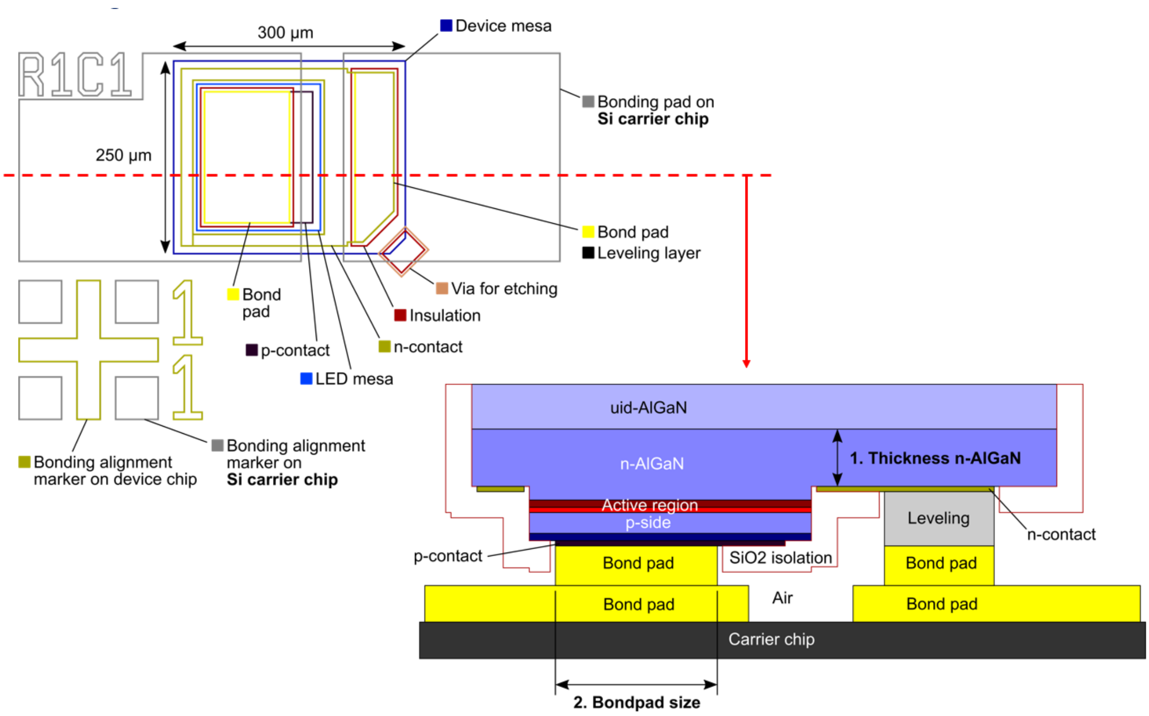

Figure 2.35: Section of the LEDs with the square mesa design used for the 2D simulations.

| **Layer** | **Material** | **Doping** | **Thickness [nm]** | $\kappa_{th}$ **[W/mK]** |
|---|---|---|---|---|
| Shield layer | $Al_{0.5}Ga_{0.5}N$ | | 430 | 1.4 |
| n-AlGaN | $Al_{0.5}Ga_{0.5}N$ | Si ($2\times10^{18}$) | 1067 | 11.9904 |
| First barrier | $Al_{0.33}Ga_{0.67}N$ | Si | 40 | 13.2996 |
| Active region | $2\times Al_{0.33}Ga_{0.67}N$<br>$3\times Al_{0.21}Ga_{0.79}N$ | | 5<br>2 | $\kappa_{th,L}=13.2996$<br>$\kappa_{th,V}=17.088$ |
| Last barrier | $Al_{0.33}Ga_{0.67}N$ | | 15 | 13.2996 |
| EBL | $Al_{0.8}Ga_{0.3}N$ | Mg | 25 | 18.6457 |
| p-SL | $Al_{0.50}Ga_{0.50}N$ | Mg | 158 | 11.9904 |
| GaN-cap | GaN | Mg | 20 | 130 |
| p-contact | Pd<br>Au | | 50<br>50 | 71.8<br>317 |
| n-contact | Ti<br>Al<br>Ti<br>Au | | 20<br>80<br>40<br>100 | 21.9<br>237<br>21.9<br>317 |
| Leveling | Au | | 334 | 317 |
| Top bondpad | Au | | 600 | 317 |
| Bottom bondpad | Au<br>Ti | | 600<br>10 | 317<br>21.9 |
| Carrier chip | Si | | 390000 | 130 |

Table 2.3: Epitaxial structure of the thin-film LED with relative simulation parameters.

- a constant temperature of 293.15 K is imposed on the bottom surface of the carrier chip, to model the heat sink;
- an initial temperature of 293.15 K is set over the whole simulation domain;
- all the other boundaries are considered to be thermally insulating.

The first simulation is run at fixed simulation parameters in order to study the temperature distribution and the heat flow in the device. For that purpose a total AlGaN thickness of 1047 nm and a bondpad width of 70 µm is considered.

The results of the first simulation are shown in figure 2.36. A maximum temperature of ≈480 K is reached in the central region of the device, between the two gold bondpads. In all the other parts of the active region, the thermal spreading is enhanced by the vicinity of the maximum temperature region to the gold pad efficiently conducting the heat toward the substrate.

The most efficient way to increase the heat extraction from the device is to increase the gold pad width under the mesa in order to increase the contact area between the maximum temperature region and the gold pad. If on one hand this would be better for a thermal perspective enhancing the dissipation of heat, on the other hand it would require a better alignment accuracy during the bonding process. Having a wider bondpad would lead to an increase in the possibility of creating a short cut between the two contact. Reducing the bondpad width will require a lower accuracy during the bonding process, reducing in this way the risk of shortcuts between p and n electrodes. For that reason, a trade off between a good thermal dissipation and a small alignment accuracy is required.

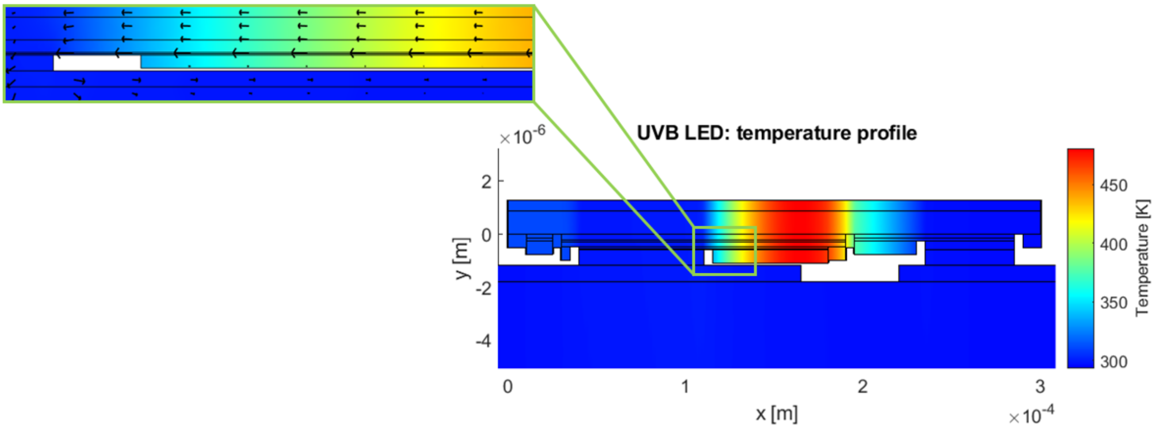

Figure 2.36: Temperature profile and heat flow in the UVB-LED structure, for a bondpad dimension of 70 µm. The arrow plot (proportional scale) in figure shows the heat flow along the different layers of the epitaxial structure.

As shown in Figure 2.36, the heat is mainly dissipated through the p-contact toward the substrate. In order to enhance the heat dissipation the thickness of the Au layer in the p-contact can be increased in order to increase the area through which the heat flows. For that purpose, the simulation is repeated for increasing thickness of the gold layer in the p-contact from the initial thickness of 50 µm up to 300 µm, since not particular restrictions on the p-contact thickness are required during the processing of the device. The maximum temperature as a function of the Au thickness for a bondpad width of 70 µm is shown in figure 2.37.

The figures also reports the simulation results for a thickness of the $SiO_2$ passivation layer of 600 nm, which corresponds to a situation in which the gap between the p-contact and the gold bottom pad in completely filled with dielectric material. It is important to notice how the maximum temperature reduces significantly in this second situation. Increasing the thickness of the $SiO_2$ in order to put in contact the dielectric layer with the gold bottom pad enhances significantly the vertical heat flow toward the substrate enhancing the heat dissipation even for small thicknesses of the Au layer. In fact, by increasing the oxide thickness a maximum reduction in temperature of 149 K is achieved.

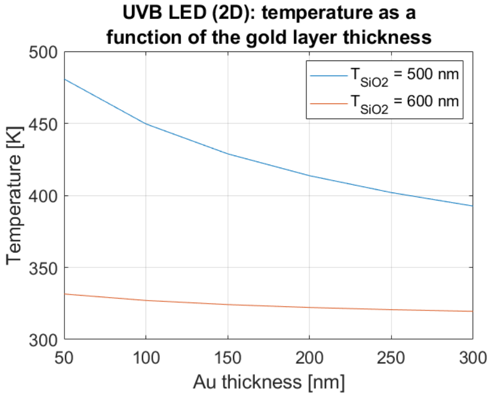

Figure 2.37: Maximum temperature as a function of the Au layer thickness in the p-contact for two different thickness of the $SiO_2$ passivation layer.

The first two-dimensional simulation is run taking as simulation parameters the top n-AlGaN thickness as indicated in Figure 2.35. In opposition to the VCSELs case in which a long cavity reflects in the possibility of multi-mode emission and a shift of the resonant wavelength, for the LEDs no particular requirements must be applied on the nAlGaN thickness. The results of the simulations are shown in figure 2.38. Also in this case the simulation is performed for two values of $SiO_2$ thickness. The results shows an approximately linear temperature decrease with increasing AlGaN thickness for both the dielectric layer thicknesses, evidencing once more how the vertical heat transport is the main dissipation mechanism in this structure.

### 2.3.2 3D simulations

In order to have a much more comprehensive study of the temperature characteristics of LEDs, 3D simulations are performed for different designs aimed at reducing current crowding. In Figure 2.39 a top view of the structures implemented in this section is shown.

The current flow through the device is not vertical, resulting in an increase of the current crowding at the edge of the mesa. One of the main contribution to the heat in LEDs is the Joule heating effect, thus it is straightforward to think that where the current crowding is enhanced the temperature would increase, causing a non uniform temperature profile with a consequent non uniform emission of light. This effect must be in general minimized in order to have good output performance.

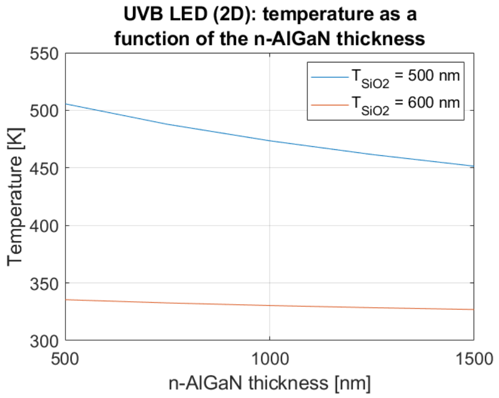

Figure 2.38: Maximum temperature as a function of the AlGaN thickness in the p-contact for two different thickness of the $SiO_2$ passivation layer.

To have a better current spreading the contacts are shaped in a fin-like structure (designs 2, 3 and 4 in Figure 2.39), the mesa is shaped accordingly to the p-contact shape.
A first simulation is implemented for a rectangular mesa design in order to compare the results with the 2D simulations already performed.

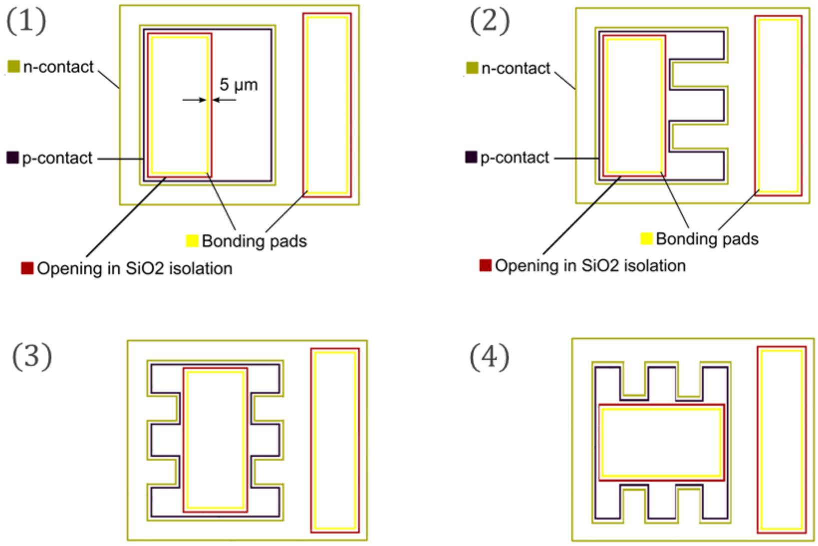

Figure 2.39: Top view of the LED structures implemented in the 3D simulations.

### Rectangular mesa

The first design is a three-dimensional extension of the 2D structure, characterized by a rectangular mesa of dimensions 160 µm × 190 µm, while the device dimensions are 300 µm × 250 µm. The epitaxial structure is equal to the one described in Table 2.1.
Some simplifications on the structure are done with respect the the 2D case in order to simplify the simulation. P-contact and n-contact, being composed by a stack of different materials are considered as effective layers with anisotropic thermal conductivity calculated

according to equation (2.1). In addition, due to the small dimensions of the epitaxial layers with respect to the lateral dimensions of the device an auto-generated mesh is not applicable in this case and a user-defined mesh needs to be defined. For that purpose, looking at the 2D simulation of the temperature profile it can be noticed that in each layer of the structure the temperature gradient mainly occurs in the lateral direction, while in the vertical direction the temperature is almost constant. Thus, more mesh points are required along the horizontal direction with respect to the vertical one. For that purpose a 2D triangular mesh is used in correspondence of the bottom side of the n-contact and the obtained distribution is sweeped vertically along the whole structure of the device. In the substrate, a three-dimensional tetrahedral mesh is used.
In Figure 2.40 a top view of the mask sequence used for the fabrication is shown. The first design is characterized by a width of the left bondpad (under the mesa) of 70 µm so that the results at fixed design parameters can be compared to the one obtained in the 2D simulations. The simulations are then repeated iteratively for increasing bondpad width and AlGaN thickness to study how the temperature can be reduced by tuning the dimensions of the two layers.

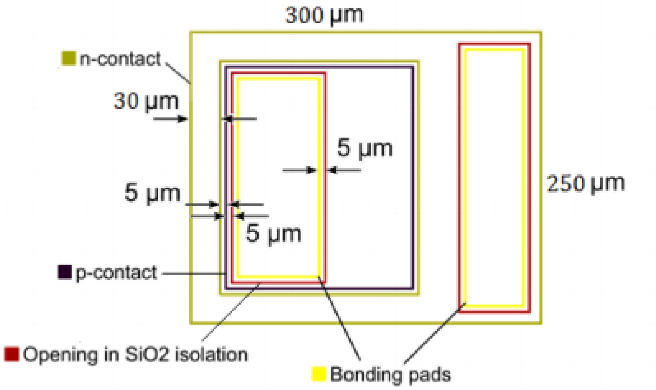

Figure 2.40: Top view of the device structure, with a rectangular mesa design.

The first simulation is performed at fixed parameters:

- bondpad width: 70 µm
- AlGaN thickness: 1067 µm

The result of the simulation is shown in Figure 2.41 and Figure 2.42 for a $SiO_2$ thickness of 500 nm and 600 nm, respectively, where the temperature profile is represented from a top view of the device. A slightly smaller temperature with respect to the results of the 2D simulation is observed, but this can be simply explained by the fact that in the 2D case the heat spreading in the lateral direction along the y-axis was not considered, so the obtained results appeared to be overestimated. The results shows accordance with the previous simulations and the maximum temperature is achieved in the central region of the device between the two bondpads and mainly dissipated through the gold pads.

The simulation is then repeated varying the bondpad width and the AlGaN thickness in order to study the influence on the maximum temperature and eventually tune the two parameters in order to reach a tradeoff between a small alignment accuracy and a reasonable

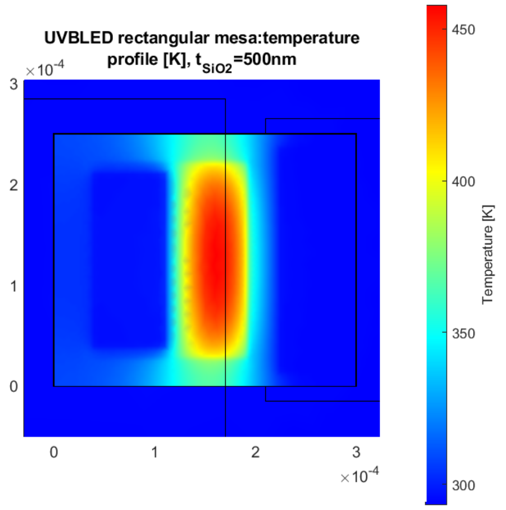

Figure 2.41: Temperature distribution in the rectangular mesa LED for a $SiO_2$ thickness of 500 nm.

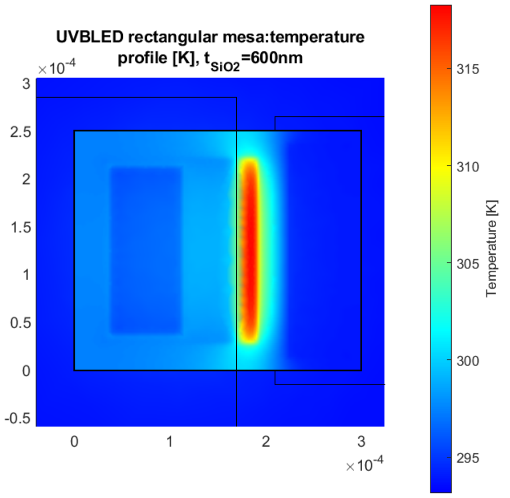

Figure 2.42: Temperature distribution in the rectangular mesa LED for a $SiO_2$ thickness of 600 nm.

temperature in the device.

In figure 2.43 the maximum temperature in the device is plotted as a function of the top AlGaN layer thickness, which is increased from 0.5 µm up to 1.5 µm. The plot reports the results for two values of $SiO_2$ thickness. It can be noticed that as the AlGaN thickness is increased the maximum temperature decreases as well with an almost linear behaviour like in the 2D case. The simulations shows a really weak dependence of the temperature on the AlGaN thickness as the $SiO_2$ thickness is increased up to 600 nm confirming that the main mechanism of heat spreading in the device occur in the vertical direction rather than in the lateral one. Thus, even if the $SiO_2$ is characterized by a very poor thermal conductivity ($\kappa_{th,SiO2}$=1.4 $Wm^{-1}K^{-1}$) the most efficient way to reduce the temperature is to increase the thickness of the dielectric passivation layer.

In figure 2.44 the temperature is represented as a function of the bondpad dimension. It can be easily notice that for a $SiO_2$ of thickness 600 nm the temperature is randomly varying around an average value of 318.3 K so that the maximum temperature is clearly independent from the bondpad dimension. This solves the problem of the alignment accuracy, so smaller bondpad can be used ensuring at the same time a good heat spreading.

### E-shaped p-contact

In the second design a more complex geometry is implemented by using a fin-like structure with three mesa fins and a similar shaped p-contact. The structure is modelled in order to have the fin width exactly equal to the spacing between the fins, while the n-contact fins are modelled in order to have a 5 µm space from the p-contact in order to avoid shortcuts between the two contacts. A representation of the mask layout for the processing of the device is shown in Figure 2.45. All the other dimensions are kept equal to the rectangular mesa design.

The simulation results for the second design at fixed simulation parameters are shown in Figure 2.46 and Figure 2.47, where the temperature distribution of the device is shown.

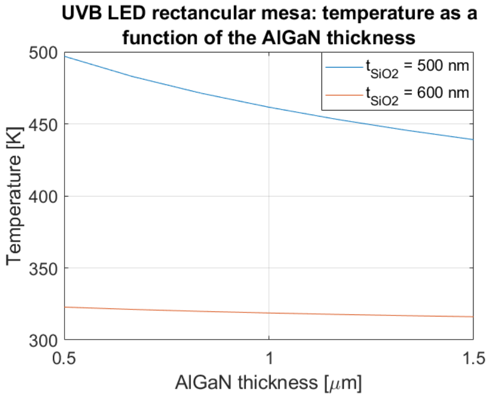

Figure 2.43: Maximum temperature as a function of the top AlGaN thickness for two thicknesses of the $SiO_2$ layer and fixed bondpad width (70 µm).

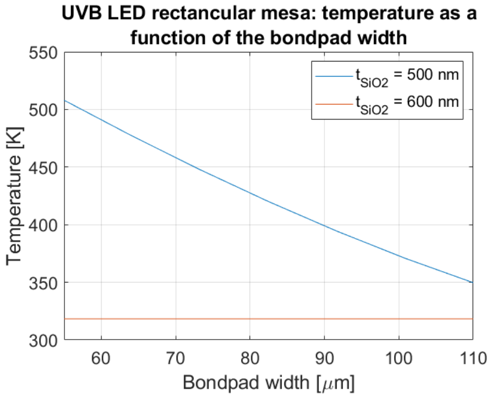

Figure 2.44: Maximum temperature as a function of the bondpad width for two thicknesses of the $SiO_2$ layer and fixed total AlGaN thickness (1067 nm).

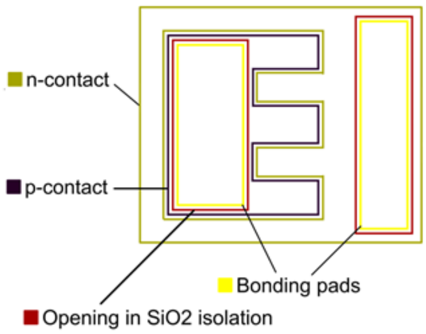

Figure 2.45: Top view of the device structure in the E-shaped p-contact design.

The maximum temperature is in this case observed in the central region of the fins, while the presence of the Au bondpad (n-contact) efficiently removes the heat at the extremities of the fins. This clearly shows how this structure is actually not only better from an electrical perspective but also from a thermal point of view. In fact by dividing the mesa in several fins the lateral heat spreading in the y direction is enhanced.

The simulation is repeated for increasing AlGaN thickness and increasing bondpad width. The results are shown in Figure 2.48 and Figure 2.49, respectively. In this case, the dependence on the AlGaN thickness appears to be weaker than in the design with the rectangular mesa achieving a maximum reduction of 30 K by increasing the AlGaN thickness from 0.5 µm up to 1.5 µm.

### Symmetric E-shaped p-contact

To reduce the current crowding also on the left side of the mesa a symmetric E-shaped contact is implemented, adding fins electrodes also on the other side on the mesa. A top view of the structure is shown in figure 2.50.

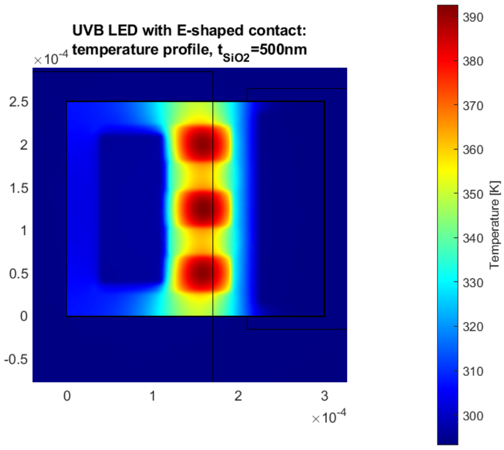

Figure 2.46: Temperature distribution for the LED design with E-shaped p-contact for a $SiO_2$ thickness of 500 nm.

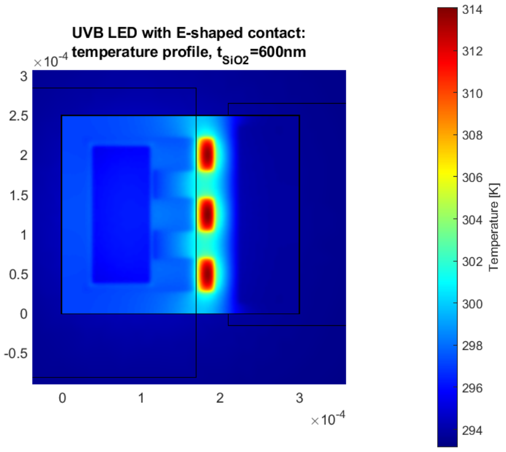

Figure 2.47: Temperature distribution for the LED design with E-shaped p-contact for a $SiO_2$ thickness of 600 nm.

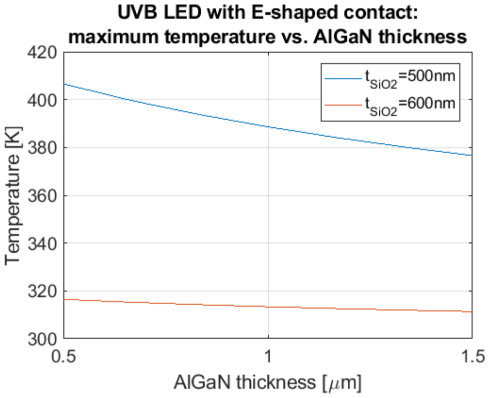

Figure 2.48: Maximum temperature as a function of the AlGaN thickness for the LED design with E-shaped p-contact, for two thicknesses of the $SiO_2$ layer and fixed bondpad width (70 µm).

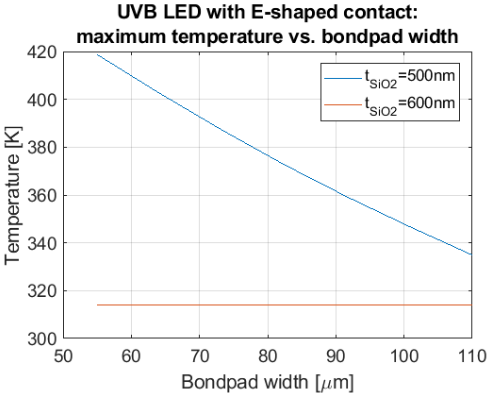

Figure 2.49: Maximum temperature as a function of the bondpad width for the LED design with E-shaped p-contact, for two thicknesses of the $SiO_2$ layer and fixed total AlGaN thickness (1067 nm).

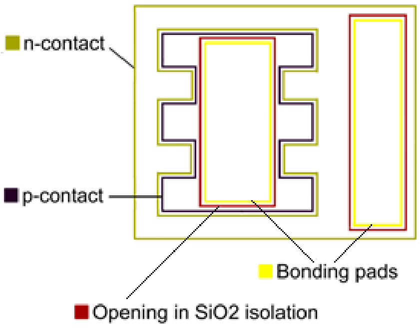

Figure 2.50: Top view of the device structure in the symmetric E-shaped p-contact design.

The temperature profile is shown in Figure 2.46 and Figure 2.47. For a $SiO_2$ thickness of 500 nm the maximum temperature is achieved in the correspondence of the left fins extremities. This is reasonable since they are connected only to the gold pad under the mesa so that the heat is dissipated only through that path. The right fins are in between the two pads and the heat is dissipated through both of them resulting in a lower temperature. A further reduction in temperature is observed ($T_{max}$ = 378 K) with respect to the previous design with E-shaped mesa. The temperature reduction is however mainly due to the shorter fins length, which enhances the heat dissipation through the gold bondpad under the p-contact.

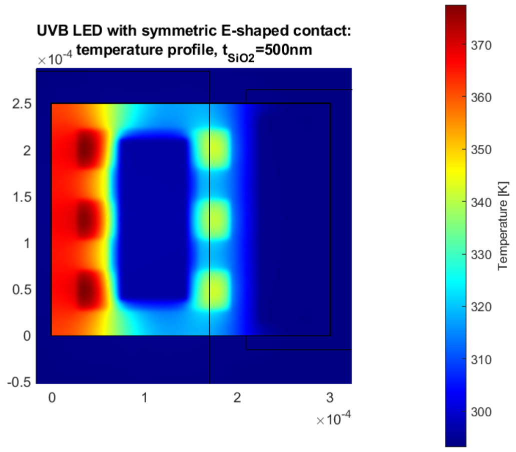

Figure 2.51: Temperature distribution for the LED design with symmetric E-shaped p-contact for a $SiO_2$ thickness of 500 nm.

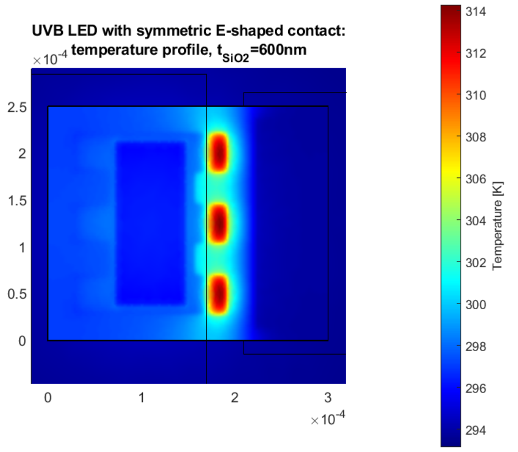

Figure 2.52: Temperature distribution for the LED design with symmetric E-shaped p-contact for a $SiO_2$ thickness of 600 nm.

In Figure 2.53 the maximum temperature is extracted as a function of the AlGaN thickness. The dependence is weaker in this case compared to the design with fins only on one side of the mesa, achieving a maximum reduction in temperature of 23.5 K.
To study how much the alignment accuracy can be reduced, the simulations are implemented by varying the bondpad lateral dimension. The results are shown in Figure 2.54. Also in this case increasing the thickness of the $SiO_2$ layer allows to reduce the bondpad dimension without effects on the heat dissipation capability of the device.

### 90° rotation of symmetric E-shaped p-contact

The last design studied in this chapter is obtained by rotating the p-contact 90°. A top view of the structure is shown in Figure 2.55.

For a $SiO_2$ thickness of 500 nm (Figure 2.56) the maximum temperature is achieved in the left part of the mesa, while the heat is efficiently dissipated in all the other regions due to the vicinity to the gold pad. It can be noticed that by rotating the bondpad, the temperature achieved in the device is increased with respect to the previous designs, but it is still lower than the device with rectangular mesa.
As the thickness of the $SiO_2$ passivation layer is increased to 600 nm (Figure 2.57) and the dielectric passivation layer is put in contact with the gold bottom bondpad the temperature

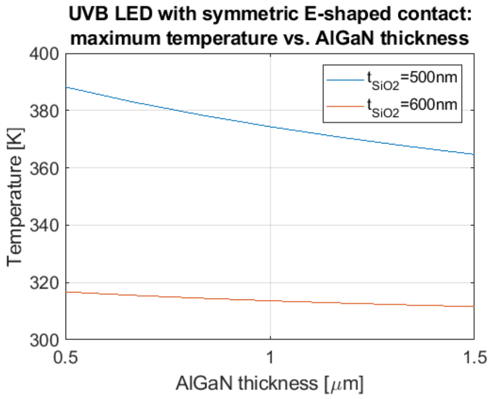

Figure 2.53: Maximum temperature as a function of the AlGaN thickness for the LED design with symmetric E-shaped p-contact, for two thicknesses of the $SiO_2$ layer and fixed bondpad width (70 µm).

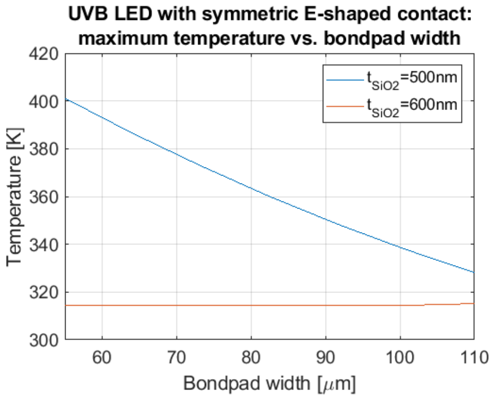

Figure 2.54: Maximum temperature as a function of the bondpad width for the LED design with Symmetric E-shaped p-contact, for two thicknesses of the $SiO_2$ layer and fixed total AlGaN thickness (1067 nm).

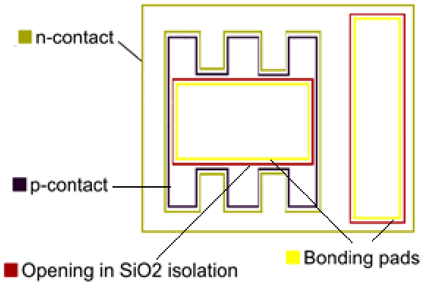

Figure 2.55: Top view of the device structure in the rotation of the symmetric E-shaped p-contact design.

drastically reduces, reaching a temperature of 298 K, which is indeed comparable to the ambient temperature.

The simulations are repeated for increasing AlGaN width and bondpad dimensions. Notice that also in this case the bondpad shorter dimension is varied, so that the variation occurs in the y direction in this case. Thus, varying the bondpad width does not directly affect the alignment tolerance that is related to the dimensions along x.
The results of the simulations are shown in figures 2.58 and 2.59, respectively. It is evident from the temperature study that for this design the most efficient way to dissipate heat is to increase the thickness of the $SiO_2$, so that both the dependence on the AlGaN thickness and bondpad dimension become negligible.

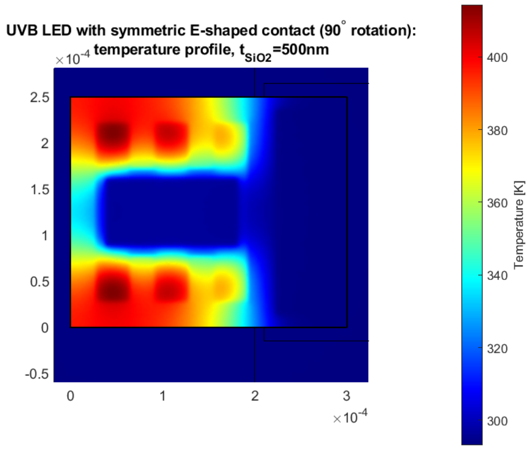

Figure 2.56: Temperature distribution for the LED design with 90° rotation of the symmetric E-shaped p-contact for a $SiO_2$ thickness of 500 nm.

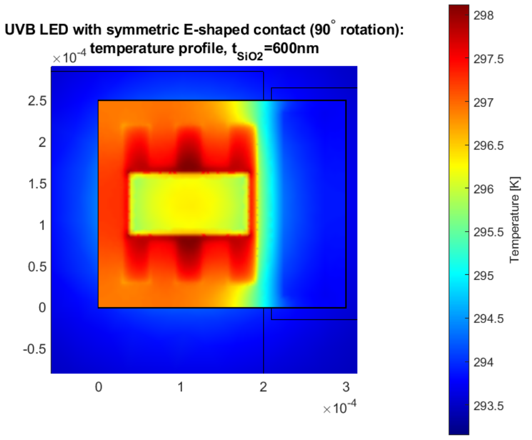

Figure 2.57: Temperature distribution for the LED design with 90° rotation of the symmetric E-shaped p-contact for a $SiO_2$ thickness of 600 nm.

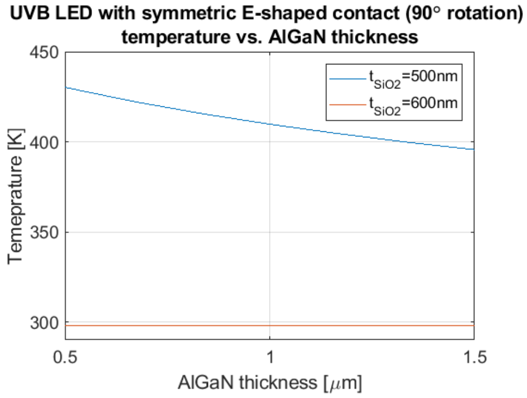

Figure 2.58: Maximum temperature as a function of the AlGaN thickness for the LED design with 90° rotation of the symmetric E-shaped p-contact, for two thicknesses of the $SiO_2$ layer and fixed bondpad width (70 µm).

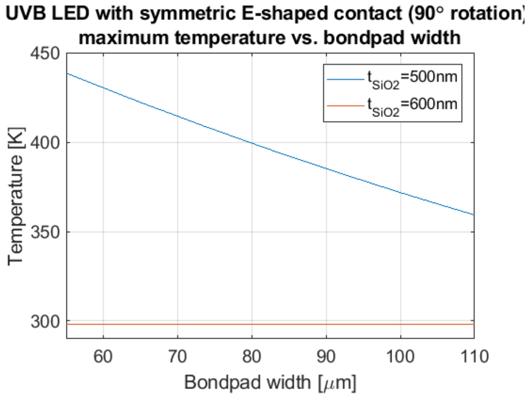

Figure 2.59: Maximum temperature as a function of the bondpad width for the LED design with 90° rotation of the Symmetric E-shaped p-contact, for two thicknesses of the $SiO_2$ layer and fixed total AlGaN thickness (1067 nm).

### Thermal resistance calculation

The temperature behaviour for the different designs described so far can be compared by studying the trend of the thermal resistance associated to each device:

$$R_{th} = \frac{\Delta T}{P_{diss}} \tag{2.7}$$

Where ΔT is the temperature increase in the LED, calculated as the difference between the maximum temperature achieved in the active region and the ambient temperature (293.15 K), and $P_{diss}$ is the total dissipated power in the active region (W).

The calculations for an oxide thickness of 500 nm are reported in figure 2.60 and 2.61. Even if it reaches higher temperatures the square mesa design is the one characterized by the lowest thermal conductivity: at equal dissipated power density, the heat generated in the active region is higher than in the other designs due to the bigger contact area between the p-contact and the mesa.

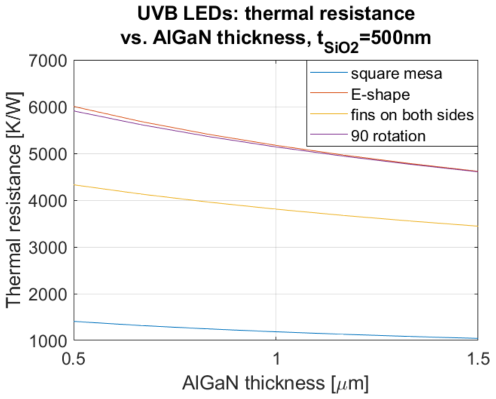

Figure 2.60: Thermal resistance as a function of the AlGaN thickness for the different designs for a $SiO_2$ layer thickness of 500 nm.

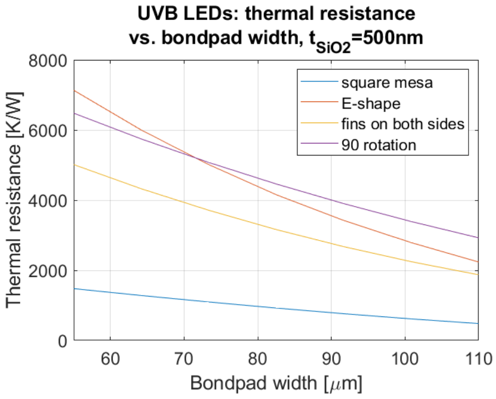

Figure 2.61: Thermal resistance as a function of the AlGaN thickness for the different designs for a $SiO_2$ layer thickness of 500 nm.

A way to reduce efficiently the thermal resistance is to increase the thickness of the $SiO_2$. In fact, the results reported in figures 2.62 and 2.63 shows a reduction of approximately one order of magnitude for all the different designs.

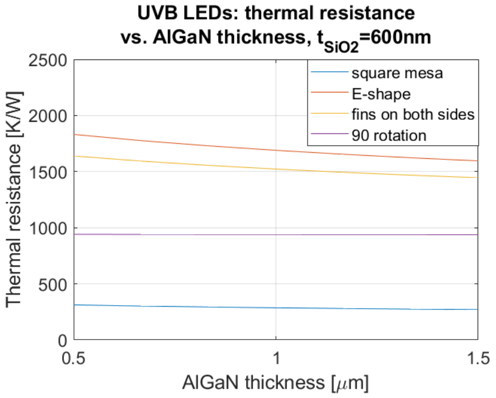

Figure 2.62: Thermal resistance as a function of the AlGaN thickness for the different designs for a $SiO_2$ layer thickness of 600 nm.

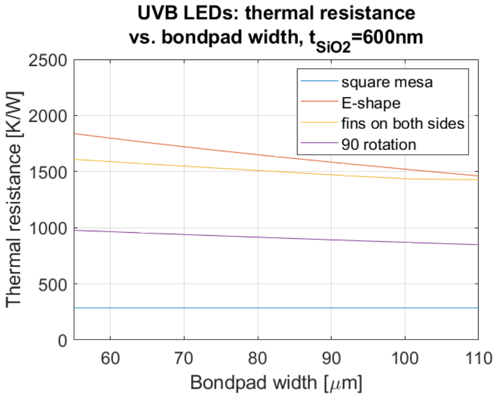

Figure 2.63: Thermal resistance as a function of the AlGaN thickness for the different designs for a $SiO_2$ layer thickness of 600 nm.

Even if the thermal resistance is drastically decreased with increased dielectric layer thickness, it is still too high compared to the typical thermal conductivities of UVB LEDs. Recent studies on such devices report a thermal conductivity ranging in the interval 37 $\div$ 154 K/W [29], according to different designs, confirming the necessity of additional improvements under a thermal perspective in order to further reduce the thermal resistance of our devices. The great difference between the simulation results and the literature values for such kind of devices can be also explained by the fact that the computations of the thermal resistance in this work are computed by taking as a reference the maximum temperature achieved in the active region. A more accurate and realistic result can be obtained by taking a sort of average of the temperature in the active region. With respect to the VCSEL case, the temperature in the active region is now strongly varying in the horizontal direction, so that the computation of the thermal resistance is strongly sensitive to the choice of the reference temperature for the calculations. These calculations are, however, not implemented in the following and can be taken as a future step for the developing of this work.

# 3 | Transfer matrix method for thermo-optical simulations of VCSELs resonance

In this chapter a one-dimensional transfer matrix method is implemented in Matlab to study the temperature induced shift in the resonance wavelength. The resonance wavelength appears to be red-shifted as the cavity temperature increases. Two types of results are studied in the following.

An initial simulation for a constant temperature profile at 300 K in the whole resonator is studied and the resonance wavelength is extracted. The second set of simulations are implemented for a varying temperature profile along the optical axis. It is extracted from the COMSOL simulations performed in the previous chapter and the average temperature in each layer is calculated. This is then used to update the thermo-optic coefficient of the corresponding layer. A the end, the obtained resonance wavelength is compared to the one relative to the constant temperature profile to calculate the shift-rate.

The second type of simulations are repeated at increasing power density. From the COMSOL simulations it is observed that the temperature achieved in the cavity is perfectly linear with increasing dissipated power density in the active region for all the structures under analysis. The simulation is then repeated iteratively for increasing dissipated power and the corresponding resonant wavelength trend with power is reported.

## 3.1 The Transfer Matrix Method (TMM)

The transfer matrix method is a powerful tool for the design of optical cavities. It can be used more in general to study propagation in any multilayered structure by analysing the interaction of reflected and transmitted wave at each interface of the stack.

Assuming linearly polarized waves in a one-dimensional scalar approach the Helmholtz's equation must be solved [22]. It is a second order differential equation:

$$\frac{d^2E(z)}{dz^2} + \gamma^2 E(z) = 0 \tag{3.1}$$

where $E(z)$ is the phasor of the transverse electric field component. The complex propagation constant can be computed as

$$\gamma = \beta_m - i\frac{\alpha_m}{2} \tag{3.2}$$

where the real part $\beta_m = 2\pi\bar{n}_m/\lambda$ is related to the refractive index of the m-th layer of the stack, while the imaginary part $\alpha_m$ is related to losses and it it is assumed do be grater or

equal than zero everywhere in the cavity except for the QW region where the presence of gain lead to $\alpha_m < 0$.
Light propagating in a multilayered structure experience multiple reflection events each time it meets a surface, where it can be either reflected back into the current medium or transmitted in the next layer of the stack. In each layer the total electric field can be computed as the superposition of a forward propagating wave, travelling toward positive value of z, and a backward propagating wave travelling in the opposite way. Assuming a stack composed by M layers, the electric field in the layer $z_m < z < z_{m+1}$ caN be written as

$$E(z) = E_m^+(z) = E_m^-(z) = E_m^+ e^{-i\gamma_m(z-z_m)} + E_m^- e^{i\gamma_m(z-z_m)} \tag{3.3}$$

where $E_m^+$ and $E_m^-$ are the complex field amplitudes of the waves at interface posed at $z = z_m$. The complex amplitudes can be calculated by imposing as boundary conditions the continuity of electric and magnetic field transverse components, obtaining:

$$E_m^+ = \left(\gamma_m^+ E_{m+1}^+ + \gamma_m^- E_{m+1}^-\right) e^{i\gamma_m d_m} \tag{3.4}$$

$$E_m^- = \left(\gamma_m^- E_{m+1}^+ + \gamma_m^+ E_{m+1}^-\right) e^{-i\gamma_m d_m} \tag{3.5}$$

with $d_m$ thickness of the m-th layer of the stack and the abbreviations:

$$\gamma_m^+ = \frac{\gamma_m + \gamma_{m+1}}{2\gamma_m} \tag{3.6}$$

$$\gamma_m^- = \frac{\gamma_m - \gamma_{m+1}}{2\gamma_m} \tag{3.7}$$

have been introduced.
Equations (3.4) and (3.5) can be written in a more compact way in a matrix form:

$$\begin{pmatrix} E_m^+ \\ E_m^- \end{pmatrix} = \bar{T}_m \begin{pmatrix} E_{m+1}^+ \\ E_{m+1}^- \end{pmatrix} \tag{3.8}$$

where $\bar{T}_m$ is the Transfer Matrix of the system.
The above explained set of equations are known as Transfer Matrix Method and it will be used in this chapter to study the resonance of the radiation in VCSELs cavities.

## 3.2 Matlab implementation of the TMM

The TMM is used to calculate the distribution of the z-component of the electric field in the cavity. The used model is one-dimensional such that only the field along the optical axis of the device is considered.
The input of the program is a `.txt` file containing the structure and the relevant parameters for the given material. The structure is defined layer by layer, each one specified by a different material. The general structure of a layer is defined in the following way:

```
Material   Thickness   Thermo-optic coefficient   Temperature  (QW)
```

The first word specifies the material of the layer, the second one is the thickness expressed in nanometers, then the thermo-optic coefficient is defined and the last parameter is the temperature of the layer. The text in brackets (QW) is used to specify if the defined layer is a QW region. If the string `'QW'` is read at the end of the line, than the absorption is set to 0 and the confinement factor is set to 1. The structure is read layer by layer and all the parameters are saved.

The main parameter which defines the thermal behaviour of the system is the thermo-optic coefficient, which is defined as the derivative of the refractive index with respect to the temperature. The thermo-optic coefficients of $SiO_2$,$HfO_2$, Al and $Al_{0.7}Ga_{0.3}N$ are computed by interpolating data extracted from literature. The lack of measurements for AlGaN at different compositions leads to the necessity of a more general definition for the thermo-optic coefficient of AlGaN which is strongly related to the Al composition of the alloy. In Appendix A the derivation of the thermo-optic coefficient for all the Al composition of AlGaN alloys as a function of the wavelength and the temperature is reported. All the calculated values are extracted and used to update the refractive index of the corresponding layer according to the temperature specified in the input file.

At this point, the electric field distribution can be computed. For that purpose, the z axis is discretized in infinitesimal elements each one of length $0.05 \times 10^{-9} m$. In order to find the resulting electric field the Helmholtz equation is solved:

$$\nabla^2 E(z) + k^2 E(z) = 0 \tag{3.9}$$

where $k$ is the wavenumber and E(z) the electric field. The Helmholtz's equation is therefore an eigenvalue equation whose solutions are the eigenvalues (resonance wavelengths) and eigenvectors (z-component of the field). The problem is solved by building a matrix A of size $n \times n$, with $n$ number of elements along z. This matrix is a sparse matrix in which only the elements along the main diagonal and the first two adjacent diagonals are non-null. The eigenvalue equation associated to the matrix A ($A\Psi(z) = 0$) is solved through the matlab command:

```
[ tmp.eigVectors, tmp.eigValues ] = eigs(A, tmp.solutions, 'sm')
```

where `tmp.solutions` is a variable containing the number of eigenvalues to be computed, in this case it is set to 2, while `'sm'` specifies the type of eigenvalues to be computed (`'sm'` = smallest magnitude). The correct eigenvalue is then selected by taking the one with smaller imaginary part. In fact, the imaginary part is related to the absorption and so to the losses. The associated eigenvector is the electric field distribution in the cavity (i.e. standing wave) and it is extracted according to the index corresponding to the selected eigenvalue.

The obtained eigenvalue corresponds to the correction to the resonance wavelength, which is updated according to the following formula:

$$\lambda_{new} = \frac{\lambda_0}{1 - Re\{\xi\}} \tag{3.10}$$

where $\lambda_0$ corresponds to the initial guess for the resonance wavelength defined at the beginning of the algorithm and $\xi$ is the calculated eigenvalue of the matrix A, solution of the Helmholtz's equation. The calculated resonance wavelength is used as initial guess for the computation of the field by updating the wavenumber $k$ appearing in equation 3.9. At this point the Helmholtz's equation is solved again and the relative error is computed by subtracting this final value to the initial guess, in modulus. The procedure is repeated in loop until a certain tolerance is reached: $|\lambda_0 - \lambda_{new} < 10^{-3}|$.

From the obtained field and resonance wavelength several other quantities, characteristic of VCSELs resonance and operation, are computed. These quantities include:

- longitudinal confinement factor;
- cavity loss;
- threshold gain;
- photon lifetime;
- slope efficiency.

## 3.3 Results

The Transfer Matrix Method presented in the previous sections is used to study the thermal behaviour of the VCSELs resonance for different structures. In particular, UVB, UVC VCSELs and GaN based blue VCSELs are analysed. Due to the lack of measurements on the first two kind of devices the comparisons with measured values are reported only for the case of blue-VCSELs. The results of the simulations show great accordance with the experimental results reported in literature.
The simulations are repeated for each structure in the case of short and long cavity showing a reduced rate of shift of the wavelength for the two cavity length. In fact, for longer cavities the temperature reached in the active region is drastically reduced leading to a smaller shift in the emission wavelength.

### 3.3.1 GaN-based blue-emitting VCSELs

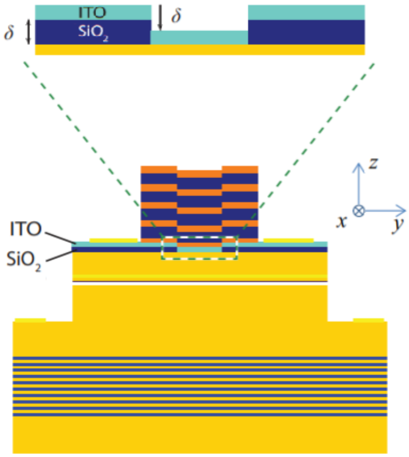

Figure 3.1: GaN-based VCSEL structure emitting at 420 nm (blue range of the light spectrum), with GaN cavity and hybrid DBR configuration (top dielectric DBR and bottom epitaxial mirror). Image adapted from [47].

In order to analyse the correctness of the results a first simulation is performed on the GaN-based blue-emitting VCSEL studied in [47],[48]. The VCSEL structure under study is shown in Figure 3.1 and it is composed by a GaN-based cavity designed to emit at a nominal wavelength of 420 nm. The structure is characterized by a n hybrid DBR configuration, with

a top dielectric DBR composed of a stack of 7 pairs of $SiO_2$(71.4 nm)/$TiO_2$(40.1 nm) layers and a bottom epitaxially grown DBR made by 42 pairs of GaN(42.17 nm)/$Al_{0.8}In_{0.2}N$(45.65 nm) layers. The device is electrically pumped and the current injection is implemented by using intracavity contacts through a layer of conductive oxide (ITO), while the current confinement is performed by using a $SiO_2$ aperture of width 4 µm. The temperature profile is first simulated in COMSOL Multiphysics and extracted. The average temperature in each layer is then calculated and used to update the refractive index of the layer. In Figure 3.2 the temperature profile and the staircase approximation are shown.
Due to the bottom epitaxial DBR the temperature achieved in the active region is significantly lower than the one reached in the UV-VCSELs with double dielectric DBR scheme. In fact, as III-nitride materials have better thermal conductivity the heat is efficiently dissipated toward the substrate.
The obtained thermal profile shows good agreement with the results reported in the paper.

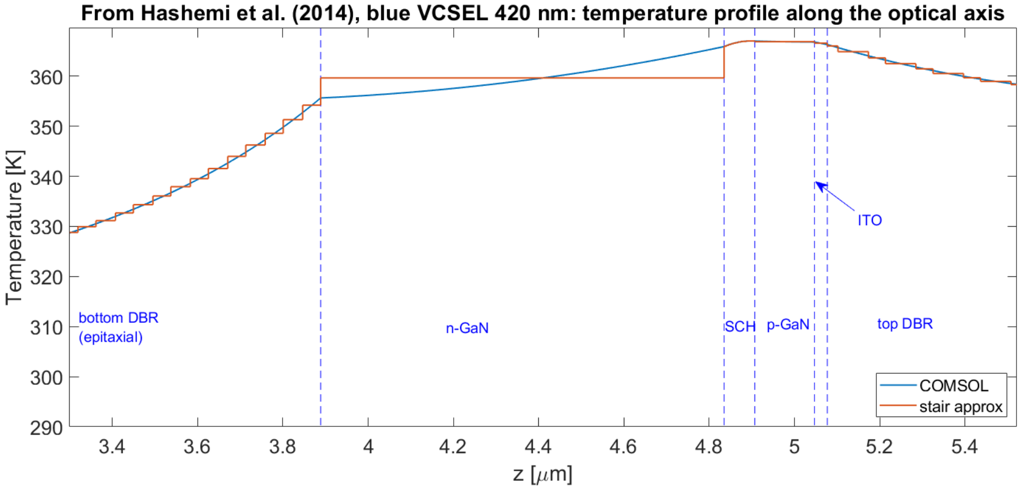

Figure 3.2: Temperature profile extracted from COMSOL and staircase approximation for the blue-emitting VCSEL from [48].

The simulation is performed initially for a constant temperature of 300K in the whole structure and then it is repeated in the case of space varying temperature. The shift rate $d\lambda/dT$ is computed by the ratio between the difference between the resonance wavelengths in two cases and the difference between the maximum temperature in the cavity and 300K. In table 3.1 the results for the GaN based blue VCSEL are reported.
The obtained resonance shift is computed accordingly:

$$\frac{d\lambda}{dT} = \frac{0.1952\,nm}{67\,K} \approx 0.029\,nm/K \tag{3.11}$$

Literature values for GaN-based blue VCSELs ranges from 0.012[49] nm/K to 0.06[50] nm/K. Thus, the value obtained from the simulations is comparable with the typical experimentally measured shift of the wavelength with temperature which confirms the correctness of the approach.

The temperature profile has been calculated starting from a dissipated power in the active region of $5 \times 10^{16}$ W/m$^3$, value obtained from calculations of the Joule heating effects in the structure [48]. The total dissipated power is then approximately 0.045 W. In figure 3.3

|  | const $T = 300K$ | T profile from COMSOL |
|---|---|---|
| Resonance wavelength [nm] | 419.9992 | 420.1944 |
| Threshold gain in QWs [cm$^{-1}$] | 79458.2227 | 79273.335 |

Table 3.1: Resonance wavelength and threshold gain for the blue emitting VCSEL structure for a constant temperature along the optical axis of 300 K and for the temperature profile extracted by COMSOL.

the resonance wavelength as a function of the dissipated power is reported. A linear trend of the resonance wavelength is observed in the case of the blue VCSEL. This behavior is straightforward since the thermo-optic coefficient for all the layers in the cavity is assumed to be constant with temperature.

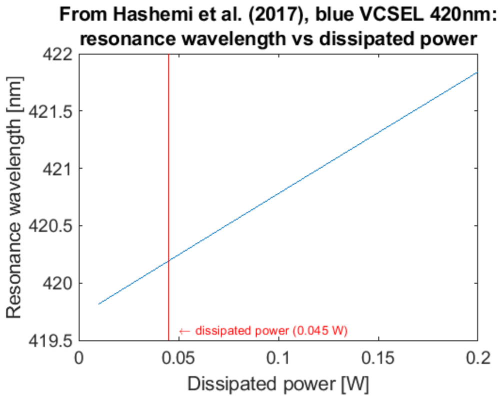

Figure 3.3: Resonance wavelength as a function of the dissipated power in the active region for the blue VCSEL structure with hybrid DBR configuration [48].

### 3.3.2 UVC-VCSELs

The temperature-induced resonance wavelength shift is now studied for the UVC VCSEL structure analysed in section 2.2. The TMM is implemented for two lengths of the cavity: $2.5\lambda$ and $10\lambda$.

A first simulation is run by keeping all the layers in the structure at a fixed temperature of 300 K. In this case, as initial guess wavelength the nominal lasing wavelength is taken, such that $\lambda_0$=275 nm.

Some considerations on the Matlab code must be done before proceeding with the analysis of the results. For longer cavities the spacing between the different longitudinal resonant modes in the cavity is smaller compared to the $2.5\lambda$ cavity. Thus, for a $10\lambda$ cavity the code is extremely sensitive to the choice of the initial guess wavelength. In fact, using $\lambda_0$ =275 nm leads to a resonance wavelength of 265.8916 nm, which corresponds to the $9.5\lambda$ resonance mode. This result is wrong, since the threshold gain of this second mode is higher than the one corresponding to the $10\lambda$ mode. In order to reduce the sensitivity of the code in all the simulations for long cavities the number of eigenvalues computed by the `eigs` command during the solving of the Helmholtz equation is set equal to 1 (i.e. `tmp.solutions=1`).

In order to have a more comprehensive understanding of the structure for longer cavities also the secondary resonance modes (i.e. $9.5\lambda$ and $10.5\lambda$) are studied in terms of resonance wavelength and threshold gain. The obtained values for a constant temperature of 300 K are reported in table 3.2. It can be observed that in the case of a $10\lambda$ cavity the threshold gain of the $9.5\lambda$ cavity mode is comparable with the lasing one. Since the lasing mode is the one characterized by the lowest threshold gain it is interesting to keep track of them in order to observe potential mode switching at higher temperatures.

| | $2.5\lambda$ cavity | $10\lambda$-cavity | | |
|---|---|---|---|---|
| | $\lambda_{2.5}$ | $\lambda_{9.5}$ | $\lambda_{10}$ | $\lambda_{10.5}$ |
| Resonance wavelength [nm] | 275.0431 | 285.1334 | 275.0092 | 265.8917 |
| Threshold gain in QWs [cm$^{-1}$] | 1377.8066 | 1724.4839 | 1378.2385 | 2904.4564 |

Table 3.2: Resonance wavelength and threshold gain of different longitudinal modes for two lengths of the cavity in the UVC VCSEL structure for a constant temperature along the optical axis of 300 K.

The simulations are now repeated by extracting the temperature profile along the optical axis of the VCSEL in COMSOL. The obtained curve is then approximated with a staircase profile in order to obtain the average temperature in each layer of the multi-stack. These values are then used in the TMM solver to update the refractive index of the different layers according to the respective thermo-optic coefficient.
In Figure 3.4 and Figure 3.5 the temperature profile for the UVC VCSEL with $2.5\lambda$ and $10\lambda$ is reported and superposed with the staircase approximation obtained by averaging the temperature profile in each layer of the stack.

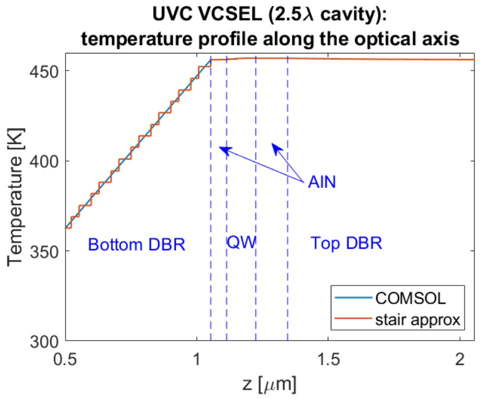

Figure 3.4: Temperature profile along the optical axis in the UVC VCSEL with a $2.5\lambda$ cavity and relative staircase approximation.

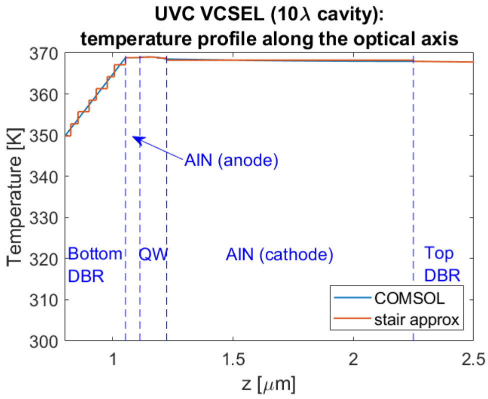

Figure 3.5: Temperature profile along the optical axis in the UVC VCSEL with a $10\lambda$ cavity and relative staircase approximation.

The results for the resonance wavelength and the threshold material gain are reported in Table 3.3. The wavelength shift with respect to the constant temperature profile or the $2.5\lambda$ cavity is 1.33 nm corresponding to a shift rate of approximately $6.1\times 10^{-3}$ nm/K. The corresponding resonance shift is smaller in the $10\lambda$ cavity since the temperature achieved in the active region is smaller, corresponding approximately to a shift rate of $3.2\times10^{-3}$ nm/K.

| | 2.5$\lambda$ cavity | 10$\lambda$-cavity | | |
|---|---|---|---|---|
| | $\lambda_{2.5}$ | $\lambda_{9.5}$ | $\lambda_{10}$ | $\lambda_{10.5}$ |
| Resonance wavelength [nm] | 276.0083 | 285.312 | 275.233 | 266.181 |
| Threshold gain in QWs [cm$^{-}$1] | 1373.1889 | 1735.7198 | 1378.1737 | 1735.7198 |

Table 3.3: Resonance wavelength and threshold gain of different longitudinal modes for two lengths of the cavity in the UVC VCSEL structure using a varying temperature profile extracted from the COMSOL simulations.

At this point a simulation for increasing dissipated power in the active region is performed. The results are plotted in Figure 3.6 and Figure 3.7 for the 2.5$\lambda$ and 10$\lambda$ cavity respectively. The resonance wavelength in the cavity is studied with increasing dissipated power in the cavity. The trend shows an initial quadratic dependence on the power, which then tends to a more linear behaviour for higher dissipated power. This trends reflects the variation of the thermo-optic coefficient with temperature. In fact, the variation in the coefficient is much more pronounced at lower temperatures showing an approximately linear behaviour at high temperatures.

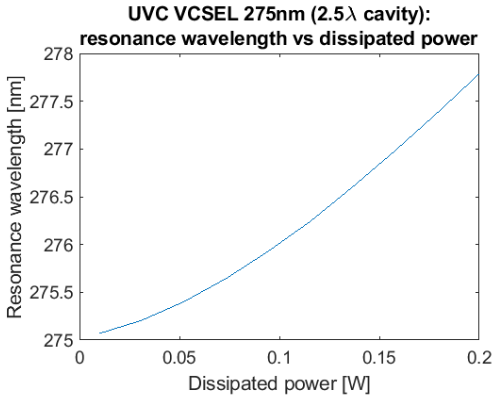

Figure 3.6: Resonance wavelength as a function of the dissipated power in the active region, for the UVC-emitting VCSEL with 2.5$\lambda$ cavity.

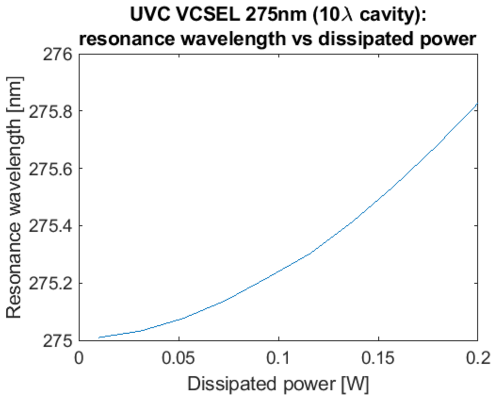

Figure 3.7: Resonance wavelength as a function of the dissipated power in the active region, for the UVC-emitting VCSEL with 10$\lambda$ cavity.

### 3.3.3 UVB VCSELs

The second device whose resonance frequency shift is investigated is the UVB VCSEL. The structure is the same implemented for the thermal simulation in COMSOL and the temperature profile is extracted and shown in Figure 3.8. The temperature profile along the optical axis is then used to update the refractive index of the corresponding layer according to the relative thermo-optic coefficient. The thermo-optic coefficient of the dielectric materials of the stack are kept fixed at $-5\times10^{-5}\mathrm{K}^{-1}$ assuming a negligible dependence with temperature. While the thermo-optic coefficient of the cavity layers are computed by applying the procedure described in Appendix A.

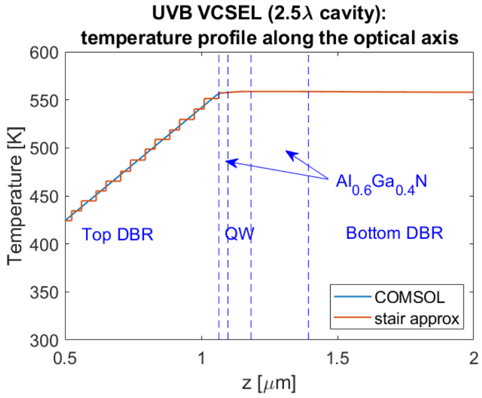

Figure 3.8: Temperature profile along the optical axis for the UVB VCSEL structure with a 2.5λ cavity.

The calculated resonance wavelength is simulated for constant temperature profile at 300 K and with varying temperature profile extracted from the COMSOL simulations. The results, in terms of resonance wavelength and threshold gain are reported in table 3.4.
The temperature-induced shift can be calculated as follows:

$$\frac{d\lambda}{dT} = \frac{1.5641\, nm}{258.67\, K} = 0.006\frac{nm}{K} \tag{3.12}$$

| | const $T = 300K$ | T profile from COMSOL |
|---|---|---|
| Resonance wavelength [nm] | 318.8312 | 320.3953 |
| Threshold gain in QWs | 871.0097 | 877.4599 |

Table 3.4: Resonance wavelength and threshold gain for the UVB-emitting VCSEL structure for a constant temperature along the optical axis of 300 K and for the temperature profile extracted by COMSOL.

The resonance wavelength shift is simulated for increasing dissipated power in the active region. The results are shown in Figure 3.9. Differently from the UVC case the trend of the resonance wavelength with increasing power density shows a saturation at high dissipated power. The result is not straightforward since the trend of the maximum temperature in the cavity with increasing dissipated power is linear. The saturation at high injected power is then related to the thermo-optic coefficient which appears to be almost constant at higher temperatures, so that the refractive index of the materials in the active region are approximately constant and that induces the saturation of the resonance wavelength.

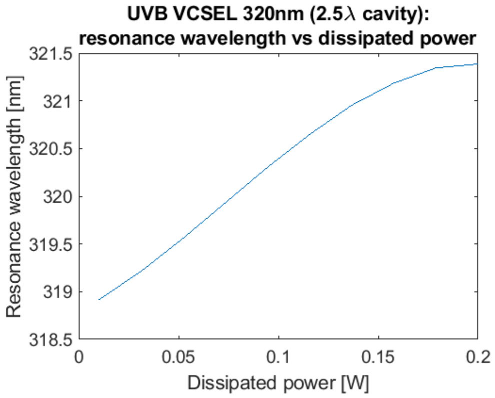

Figure 3.9: Resonance wavelength as a function of the dissipated power in the active region, for the UVB-emitting VCSEL with a 2.5$\lambda$ cavity.

# A | Thermal parameters of materials

In the following, a brief summary of the literature values for the parameters used in the simulations is reported. It is the result of the bibliographic research conducted before the beginning of the simulation activities aiming at defining a reasonable range of variation for the parameters of interest.

The main parameter which contributes to the thermal behaviour of the device is the thermal conductivity, which describes the capability of a material to conduct heat. In general, the thermal conductivity appears to be strongly dependent on the thickness of the layer and on the substrate onto which the film is deposited, dependency which is a direct reflection of the grain size or of the order of the crystal lattice. For that reason, the first section is devoted to the study of the thermal conductivity for AlGaN and $HfO_2$. The values for different substrates, deposition techniques and temperatures are investigated in order to assign a realistic value to model the thermal behaviour of the device under consideration.

The discussion then proceeds with a brief overview on the temperature dependence of some optical parameters, refractive index and thermo-optic coefficient, which are used in the optical simulations for the implementation of the TMM to study the resonance wavelength shift with temperature in Chapter 3.

## A.1 Thermal conductivity

The thermal conductivity is an intrinsic property characteristic of each material, defined as the proportionality constant between the heat flux and the temperature gradient in the material, according to the Fourier's law for heat conduction:

$$q = -\kappa \nabla T \tag{A.1}$$

where q is the heat flux density ($W/m^2$), $\nabla$T is the temperature gradient (K/m) and $\kappa$ is the thermal conductivity ($Wm^{-1}K^{-1}$).

The thermal conductivity of sputtered $SiO_2$ thin-films appears to be slightly reduced with respect to the bulk value (1.4 $Wm^{-1}K^{-1}$), so that a thermal conductivity of 1.4 $Wm^{-1}K^{-1}$ is assumed in all the simulations. On the contrary, the thermal conductivity of $HfO_2$ and $Al_xGa_{1-x}N$ have found to be strongly varying with thickness, deposition technique and substrate, such that a more accurate analysis on the range of variation is required.

### A.1.1 Hafnium dioxide ($HfO_2$)

Thermal conductivity of hafnium dioxide appears to be strongly dependent on the film thickness and on the substrate onto which the film is deposited. This dependency is a reflection of the dependency on the crystalline order of the dielectric film. The thinner the film is the smaller the grain size of the amorphous/polycrystalline film would be. Smaller grains results in more boundaries, so that the increasing scattering by phonons at grain boundaries causes a reduction in the thermal conductivity. The sensitivity on the substrates resides in the lattice mismatch between the film and the substrate. The more the mismatch the more strained the film would be upon deposition with a consequent increase of the scattering phenomena by the presence of defects, resulting in a strong reduction in the thermal conductivity of the layer.
In Table A.1 the thermal conductivity values for $HfO_2$ found in literature for different deposition techniques and different substrate are reported.
A proper choice for the thermal conductivity of $HfO_2$ is 1.2 $Wm^{-1}K^{-1}$. In fact, $HfO_2$ in the DBR of the VCSEL structures is deposited by sputtering on $SiO_2$. Both $SiO_2$ and $HfO_2$ are intrinsically amorphous materials so that no order is present.

| Ref. | thickness [$nm$] | deposition technique | $\kappa_{th}$ [$Wm^{-1}K^{-1}$] |
|---|---|---|---|
| [51] | bulk | NA | 1.63 |
| [52] | 10 | ALD | 1 ± 0.06 |
| [53] | 256 | e-beam evaporation | $\kappa_L = 0.08$ , $\kappa_V = 0.39$ |
| [38] | 0.257-0.495 | e-beam evaporation | $\kappa_V = 0.052$ |
| [54] | 200 | ALD | 4.1 ± 0.6 |
| [55] | 90 | RF magnetron sputtering | 2.54 ± 0.12 |
| [40] | 500-2000 | dc sputtering | ∼ 1.2 |
| [56] | 5.6<br>20 | ALD | 0.49<br>0.95 |
| [39] | 500-2000<br>bulk | thermal<br>evaporation | 0.07-0.02<br>17 |

Table A.1: Thermal conductivity values of $HfO_2$ thin film for different film thickness. NA= Not Applicable; NS=Non Specified

The highest values for thermal conductivity are registered for sputtered films, by either RF magnetron sputtering [55] or DC sputtering [40]. In fact, among all the different deposition techniques used for deposition of dielectric materials sputtering is the one that allows for the most ordered structure.
The lowest values are, on the contrary, reported for thermal [39] or e-beam evaporation [53]-[38].

### A.1.2 Thermal conductivity of $Al_xGa_{1-x}N$ for different alloy compositions

Aluminium gallium nitride (AlGaN) is a ternary alloy composed starting from nitride-based binary compounds (GaN and AlN). The major property of ternary and quaternary alloys is the possibility to tailor both optical and electrical properties by changing the composition of the compound.

Thermal conductivity of ternary alloys is strongly dependent on the composition. The two extreme values, corresponding to an Al composition of x=0 and x=1, assumes the values of the binary compounds by which the alloy is composed (GaN and AlN, respectively). Moving from the edges toward the center of the curve, the thermal conductivity is strongly reduced reaching a minimum in correspondence of an aluminium composition of approximately 0.6. The strong reduction in the parameter can be explained by the presence in the lattice of an increasing quantity of foreign atom with respect to the composition at the border, causing an increase in the scattering with a consequent reduction of the heat transport and thermal performance.

In figure A.1 the thermal conductivity as a function of the Al molar fraction is shown. The samples are 0.1 µm-thick $Al_xGa_{1-x}N$ films grown on c-plane sapphire by hydride vapour phase epitaxy [57].

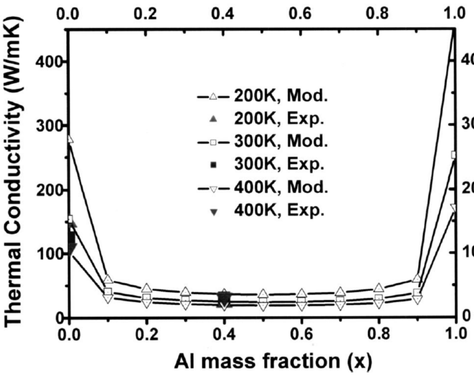

Figure A.1: Theoretical and experimental thermal conductivity of $Al_xGa_{1-x}N$ as a function of the Al molar fraction [57].

In figure A.2 the thermal conductivity of $Al_xGa_{1-x}N$ calculated with the virtual crystal model is represented [58]. Theoretical results are compared with experimental measurement performed by $3\omega$ technique. The thermal conductivity shows an abrupt reduction from an Al fraction of x=0 to x=0.1, followed by a gradual approach to the minimum, which occurs approximately at x=0.6. For Al fractions greater than 0.9 the thermal conductivity starts to increase again, approaching the bulk AlN value. The lowest values of thermal conductivity are observed for an Al molar fraction between 0.1 and 0.9, which is an indication of the increasing phonon scattering mechanism as the concentration of alien atoms in the host material increases.

*Sztein et al.* [59] calculated the thermal conductivity as the sum of two contributions: the electronic contribution is calculated by solving the Boltzmann Transport equation (BTE), while the phononic component is calculated using Callaway's model. Results are shown in

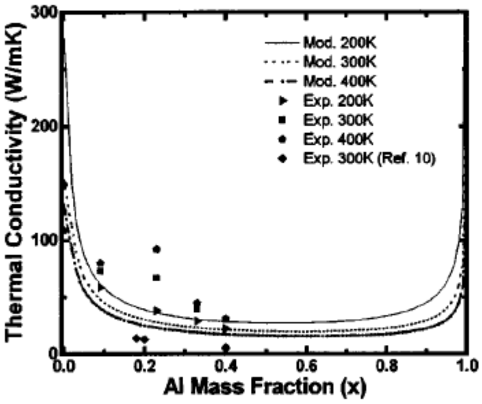

Figure A.2: Thermal conductivity of $Al_xGa_{1-x}N$ as a function of the Aluminum composition x from [58].

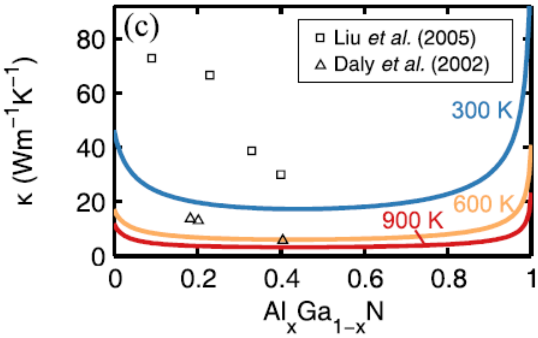

Figure A.3: Thermal conductivity of $Al_xGa_{1-x}N$ as a function of the Aluminum composition x from [59].

figure A.3, observing the typical behaviour of the thermal conductivity of AlGaN alloy. Simulations shows also a reduced thermal conductivity with increasing temperature, due mainly to an increase in the scattering by phonons.

In figure A.4 and A.5 the thermal conductivity as a function of the composition and of the temperature is shown for a sample of thickness 1.2 µm [59]. The minimum value is observed for an Aluminum composition around 0.5. While the experimental value for x=0.2 is approximately 14 $Wm^{-1}K^{-1}$.

In [61] the thermal behaviour of $Al_xGa_{1-x}$ N alloy samples grown by metalorganic vapor deposition on sapphire (0001) substrates is studied. The results are shown in figures A.6 and A.7, the results appears to be in accordance with the measured data obtained by *Koh et. al. (2016)* [60].

In figure A.8 the thermal conductivity of AlGaN as a function of the Aluminum composition is shown. The thermal conductivity of the alloy is modeled by a non-linear interpolation law starting from the thermal conductivity values of GaN ($\kappa_{GaN}$=130 $Wm^{-1}K^{-1}$) and AlN

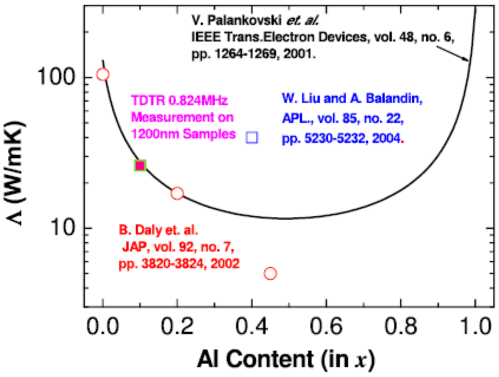

Figure A.4: Thermal conductivity of $Al_xGa_{1-x}N$ as a function of the Aluminum composition x from [60]. Also experimental results obtained by other groups are shown in figure.

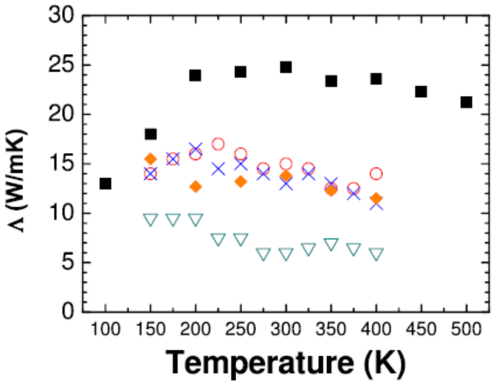

Figure A.5: Thermal conductivity of (■) 1.2 µm and 0.2 µm $Al_xGa_{1-x}N$ for different alloy compositions as a function of the temperature [60]. The other symbols correspond to the results for (×) $Al_{0.18}Ga_{0.82}N$, (○) $Al_{0.2}Ga_{0.8}N$ and (△) $Al_{0.44}Ga_{0.56}N$ obtained in [61].

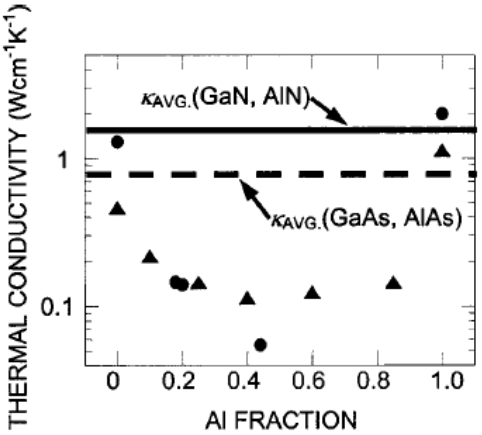

Figure A.6: Thermal conductivity of $Al_xGa_{1-x}N$ (○) as a function of the Aluminum composition x from [61]. Also the results of ref. [62] for $Al_xGa_{1-x}As$ are reported.

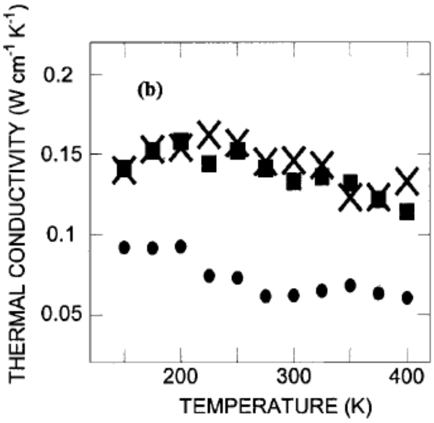

Figure A.7: Thermal conductivity of (×) $Al_{0.18}Ga_{0.82}N$, (■) $Al_{0.2}Ga_{0.8}N$ and (○) $Al_{0.44}Ga_{0.56}N$ as a function of the temperature [61].

($\kappa_{AlN}$=350 $Wm^{-1}K^{-1}$), according to the following formula [37]:

$$\kappa_x = \left( \frac{1-x}{\kappa_{GaN}} + \frac{x}{\kappa_{AlN}} + \frac{x(1-x)}{C_\kappa} \right) \tag{A.2}$$

where x is the Al composition and the parameter $C_\kappa$ describes the lattice disorder due to the random distribution of Ga and Al atoms in the lattice. This approach is also the one used to extract the thermal conductivity values in the thermal simulations performed in Chapter 2

In figure A.9 the thermal conductivity of $Al_xGa_{1-x}N$ calculated in [63] is shown. It is computed as the sum of two contributions: the lattice thermal conductivity is calculated by the virtual crystal model, while the electronic contribution results from the solution of

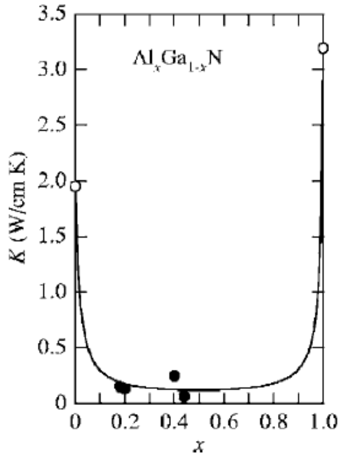

Figure A.8: Thermal conductivity of $Al_xGa_{1-x}N$ as a function of the Aluminum composition [37]. The experimental data are taken from [61] and [58].

the Boltzmann Transport Equation (BTE). The resulting curve presents a minimum at an Aluminum molar fraction x=0.4, corresponding to 60 $Wm^{-1}K^{-1}$.

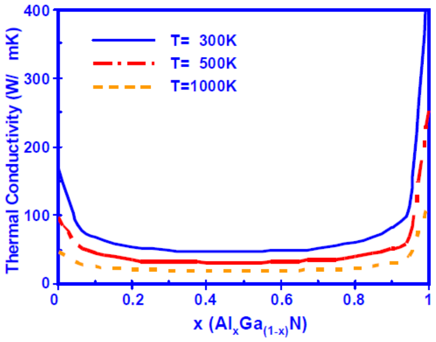

Figure A.9: Thermal conductivity as a function of Al mass fraction for $Al_xGa_{1-x}N$, in the temperature range of T=300-1000K [63].

In Table A.2 the maximum and minimum values found in literature for different $Al_xGa_{1-x}N$ composition are summarized, showing the wide range of variation of the alloy thermal conductivity.

| x | $\kappa_{th,min}$ [$Wm^{-1}K^{-1}$] | $\kappa_{th,max}$ [$Wm^{-1}K^{-1}$] |
|---|---|---|
| 0.2 | 17.62 | $> 60$ |
| 0.5 | 11.9904 | $\sim 60$ |
| 0.6 | 12.1639 | $\sim 60$ |

Table A.2: Maximum and minimum values of thermal conductivity for different compositions of AlGaN.

### A.1.3 Thermal conductivity of AlN

Alluminium nitride is a III-V semiconductive compound characterized by wide band-gap (~ 6.2 eV) and high thermal conductivity, characteristic which makes AlN a promising candidate as heat spreader material for electronic and opto-electronic applications. The nominal value of thermal conductivity for single crystal bulk AlN is of 350 $Wm^{-1}K^{-1}$, but this value is drastically reduced of more than one order of magnitude if the AlN is deposited in thin-films and it is strongly dependent on the film thickness and on the nature of the substrate. The most common deposition techniques for thin-films AlN are Molecular Beam Epitaxy, Chemical Vapour Deposition, Ion Beam Assisted Deposition, Ion Beam Sputtering and Magnetron Sputtering. Except from MBE and (metalorganic) CVD, all the other techniques do not have epitaxial growth. The obtained film are then polycrystalline, with lower crystalline quality with consequent reduced thermal and optical characteristics.

#### Epitaxial AlN

The thermal conductivity of epitaxial thin film is in general approximately one order of magnitude smaller than the nominal value for the crystalline bulk material (350 $Wm^{-1}K^{-1}$). In Table A.3 the literature values for epitaxially grown AlN thin-films are reported.
Very few articles have been found in literature for epitaxially grown AlN thin-films, and the values of thermal conductivity appears to be strongly dependent on the film thickness and on the substrate nature.

| Ref. | Thickness [$\mu$m] | $\kappa_{th}$ [W/m K] |
|---|---|---|
| [64] | 1 | 0.48-25.2 |
| [65] | 200 | 374 ± 9 |
| | 204 | 341 ± 6 |

Table A.3: Thermal conductivity of epitaxially grown AlN thin-films.

In [64] the thermal conductivity of AlN thin films on different subrates are measured by the thermal-wave mirage technique. The AlN films were grown by plasma source molecular beam epitaxy on Si(111), Si(100), $Al_2O_3(0001)$ and $Al_2O_3(1\bar{1}02)$, with a nominal thickness of 1 µm. The higher value of thermal conductivity was found to be 25 $Wm^{-1}K^{-1}$ for AlN films deposited on $Al_2O_3(1\bar{1}02)$. The results confirms that the thermal conductivity measurements are strongly correlated to the morphology of the thin films, which is dependent on the substrate onto which the film is deposited.
The higher thermal conductivity is referred to AlN deposited on $Al_2O_3(1\bar{1}02)$, which have a columnar structure consisting of high quality single crystals. The lower values is registered for AlN on Si(111), indicating that the microstructure of the thin film is not so favourable, result that is confirmed by X-ray spectroscopy data which presented a very broad peak and high background signal.

In [65] the thermal conductivity of AlN thin-films is measured by $3\omega$ measurements. The samples consist of single crystal AlN thin films grown by Physical Vapour Transport (PVT) and Hydride vapour Phase Epitaxy (HVPE). The maximum room-temperature thermal conductivity (374 $\mathrm{Wm^{-1}K^{-1}}$) is measured for a 200 µm thick sample deposited by PVT. These results are significantly higher than the previous one, confirming the higher crystal quality of thicker samples.

### A.1.4 Sputtered AlN

Sputtering is one of the most used deposition techniques for aluminum nitride thin-films. The thermal conductivity of AlN thin-films is strongly dependent on the thickness of the film: it decreases rapidly as the film thickness, and so the grain size, is reduced. The grain size is proportional to the film thickness if the process conditions are kept constant during the deposition. As a consequence, the scattering at grain boundaries is enhanced for thinner films, leading to a decrease in the thermal conductivity.
As the grain size reduces, the phonon scattering at grain boundaries increases, with a consequent reduction of the thermal conductivity.
The literature values for thermal conductivity of sputtered AlN thin films are summarized in Table A.4.

| Ref. | Thickness [nm] | $\kappa_{th}$ [$\mathrm{Wm^{-1}K^{-1}}$] |
|---|---|---|
| [66] | 200-2000 | 1.83 - 76.5 |
| [67] | 200-940 | 11.8-55.3 |
| [68] | 100-1050 | 1.7-4.5 |
| [69] | 300-1000 | 5.4-17.6 |
| [70] | 100-300 | 5.6-8.4 |

Table A.4: Literature values of thermal conductivity for sputtered AlN.

In [66] AlN thin-film are deposited on single-crystal (001) silicon substrates by RF reactive magnetron sputtering. The sample has a thickness variable up to 2000 nm to study the size effects and the thermal conductivity is measured by $3\omega$ measurements. The thermal conductivity appears to be strongly dependent on the film thickness. The results are reported in Table A.5.
The results shows that the thermal conductivity strongly increases with the film thickness and this dependence weakens gradually at bigger thicknesses. The increase in thermal conductivity with the film thickness is primarily due to the increase in the grain size.

In [67] the thermal conductivity of sputtered AlN thin-films deposited by reactive magnetron sputtering, with thickness 200 nm and 940 nm, is measured by the $3\omega$ technique. The lower boundary found for the two thickness is respectively 11.8 $\mathrm{Wm^{-1}K^{-1}}$ and 55.3 $\mathrm{Wm^{-1}K^{-1}}$. Also in this case, the dependence of the thermal conductivity on the thickness of the film is observable. The reduction in thermal conductivity of the film with decreasing thickness is due to the presence of an amorphous layer at the interface between AlN and Si, composed by small and randomly oriented grains.

In [68] the thermal conductivity of AlN thin-film in a thickness range between 100 nm and

| Film thickness | $\kappa_{th}$ [Wm$^{-1}$K$^{-1}$] |
|---|---|
| 200 | 1.83 |
| 500 | 32.3 |
| 1000 | 48.1 |
| 2000 | 76.5 |

Table A.5: Thermal conductivity of sputtered AlN thin-films for different film thicknesses [66].

1050 nm are measured. The samples are deposited by RF reactive sputtering on Si(111) substrates. The thermal conductivity measurements are performed at room temperature using the pulsed photothermal reflectance technique. The obtained thermal conductivity appears to be approximately of 1.5 Wm$^{-1}$K$^{-1}$ for thicknesses lower than 400 nm, and reaches a maximum of 3-5 Wm$^{-1}$K$^{-1}$ for film thicknesses around 800 nm - 1 µm.

In [69] the thermal conductivity of AlN thin-film deposited on silicon by RF reactive magnetron sputtering is measured by the $3\omega$ technique. The obtained thermal conductivity values ranges from 5.4 Wm$^{-1}$K$^{-1}$ for samples of thickness 300 nm and 17.6 Wm$^{-1}$K$^{-1}$ for 1000 nm thick films.

In [70] the thermal conductivity of submicron-thick AlN films are calculated by a modified ac-calorimetry technique. The samples are deposited on glass by magnetron sputtering with an inductively coupled plasma.

## A.2 Refractive index and thermo-optic coefficient

One of the main challenges in the simulation procedure is to find the values of the parameters for all the different compositions of AlGaN alloy. In fact while for the thermal conductivity and refractive index several studies have been performed, the thermo-optic coefficient of AlGaN at different composition have not been deeply investigated in literature. The main problem resides in the fact that the refractive index and so the thermo-optic coefficient are depending not only on the composition of the alloy and on the temperature, but also on the wavelength of the radiation propagating inside the medium. For that reason it is really hard to find values specific for all the cases investigated in this thesis. Thus, a more general way to define such strongly varying parameter must be introduced.
For that reason, in order to properly define the structure the model proposed by *Tisch et al. (2001)* [71] is implemented in matlab in order to extract the refractive index of the material for different composition, temperatures and wavelengths ($n\left(x,T,\lambda\right)$). From the calculated trend representing the refractive index as a function of temperature for a given wavelength, the thermo-optic coefficient at different temperatures is extracted by a simple mathematical differentiation procedure by calculating point by point the slope of the refractive index versus wavelength curve. In such way, the thermo-optic coefficient and the refractive index at different temperatures, Al composition and operating wavelength can be calculated as required.
The refractive index as a function of the photon energy, composition and temperature is derived in an analytical form by the following equation:

$$n\left(E,x,T\right)=\left[\frac{1}{2}\left(\epsilon_r\left(E,x,T\right)+\sqrt{\epsilon_r\left(E,x,T\right)^2+\epsilon_i\left(E,x,T\right)^2}\right)\right]^{1/2} \tag{A.3}$$

the dielectric function of $\mathrm{Al}_x\mathrm{Ga}_{1-x}\mathrm{N}$ below the band gap is computed by the analytical formula:

$$\epsilon\left(E,x,T\right)=C\left(x,T\right)+\frac{A\left(x,T\right)}{E_g^{3/2}\left(x,T\right)}\frac{2-\sqrt{1+y}-\sqrt{1-y}}{y^2} \tag{A.4}$$

with $y\left(E,x,T\right)=\left[E+i\Gamma\left(x,T\right)\right]$.
The model parameters $A\left(x,T\right)$, $C\left(x,T\right)$, $\Gamma\left(x,T\right)$ can be computed by simple analytical expressions:

$$\begin{aligned}
C\left(x,T\right) &= 2.49+2.27\times10^{-3}T-1.80\times10^{-6}T^2\\
&\quad-\left(0.74+4.61\times10^{-3}T-5.33\times10^{-6}T^2\right)x\\
A\left(x,T\right) &= [\ 79.30-8.37\times10^{-2}T+6.73\times10^{-5}T^2+\\
&\quad\left(18.99+0.13T-1.76\times10^{-4}T^2\right)x+37.51x^2\ ]\,eV^{1.5}\\
\Gamma\left(x,T\right) &= \left[-8.69+4.13\times10^{-2}T+\left(248.24-0.19T\right)x^2\right]\times10^{-3}eV
\end{aligned} \tag{A.5}$$

The dispersion of the refractive index is then computed by analytically differentiating the expression for the refractive index versus the energy, obtaining the following expression:

$$\begin{aligned}
\tfrac{dn}{dE}\left(E,x,T\right)= &\ \tfrac{1}{2n(E,x,T)}\tfrac{A(x,T)}{y^2E_g^{2.5}(x,T)}\left[\ \tfrac{1}{2\sqrt{1-y}}-\tfrac{1}{2\sqrt{2+y}}-\right.\\
&\left.+\tfrac{2}{y}\left(2-\sqrt{1-y}-\sqrt{1+y}\right)\ \right]
\end{aligned} \tag{A.6}$$

The results reported in [71] are reproduced with great agreement, so only the results for the composition and wavelength of interests are reported in the following.

### A.2.1 Results

The thermo-optic coefficient of AlGaN as a function of the temperature is studied. For the purpose of this thesis, the results are reported only for the AlGaN composition of interest in the case of a UVC-VCSEL. The treatment is straightforward for all the other compositions and radiation wavelength.

The VCSEL structure emitting at 275 nm is composed by an AlGaN cavity with the following molar fraction of aluminium: x=0.3 for the QWs, x=0.7 for the barriers, and x=1 (i.e. AlN) for the external layers of cavity.

In figures A.10-A.10 the refractive index as a function of the wavelength for an aluminum molar fraction of x=0.3, x=0.7 and x=1, respectively, is represented.

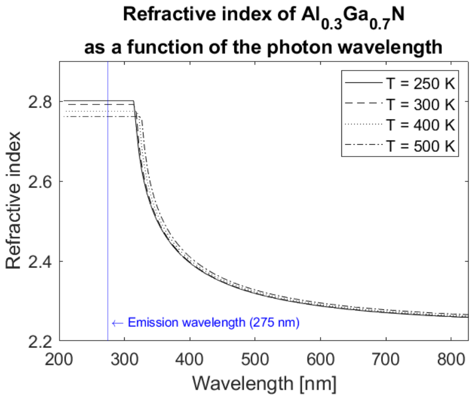

Figure A.10: Refractive index of $Al_xGa_{1-x}N$ for an aluminium molar fraction x=0.3. [71]

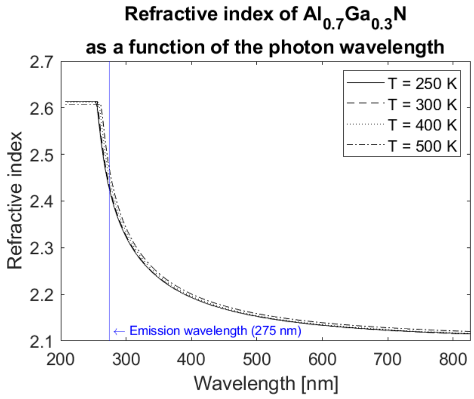

Figure A.11: Refractive index of $Al_xGa_{1-x}N$ for an aluminium molar fraction x=0.7. [71]

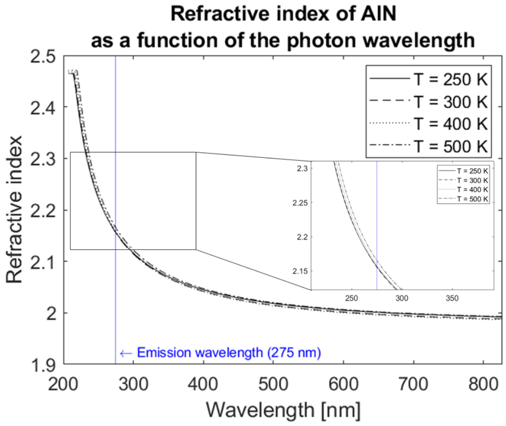

Figure A.12: Refractive index of $Al_xGa_{1-x}N$ for an aluminium molar fraction x=1.

At a wavelength of 275 nm, which corresponds to the resonance wavelength of the UVC-VCSEL design, the AlN is transparent while $Al_{0.3}Ga_{0.7}N$ is absorbing. The temperature behaviour of the refractive index for energies below and above the band-gap energy is opposite. Below the wavelength corresponding to the energy gap of the considered material the refractive index decreases with temperature (i.e. negative thermo-optic coefficient), while above the before mentioned wavelength the refractive index increases with increasing temperature (i.e. positive thermo-optic coefficient). Different is the behaviour for AlN in which there is an inversion of the curves corresponding to 250 K and 300 K, resulting in a change of sign of the thermo-optic coefficient around 270 K.

The corresponding thermo-optic coefficient as a function of the temperature is calculated for the wavelength of interest (i.e. 275 nm for the UVC-VCSELs). The obtained plot is shown in figure A.13. The above mentioned behaviour is confirmed by the calculation such that the thermo-optic coefficient of $Al_{0.3}Ga_{0.7}N$ is negative in the whole range of temperature studied, the parameter for $Al_{0.7}Ga_{0.3}N$ is always positive, while the thermo-optic coefficient for AlN changes sign around 270 K.

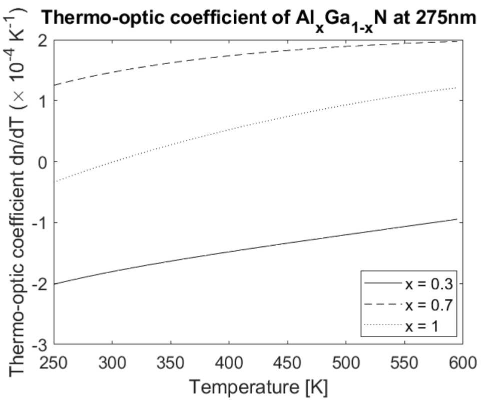

Figure A.13: Thermo-optic coefficient as a function of temperature for different AlGaN compositions, for an emission wavelength of 275 nm.

# Bibliography

[1] A. Jiménez, E. Calleja, E. Muñoz, M. Varela, C. Ballesteros, U. Jahn, K. Ploog, F. Omnés, and P. Gibart, "Correlation between transport, optical and structural properties in AlGaN/GaN heterostructures," *Materials Science and Engineering: B*, vol. 93, no. 1, pp. 64 – 67, 2002. [Online]. Available: http://www.sciencedirect.com/science/article/pii/S0921510702000351

[2] M. Kneissl, T. Kolbe, C. Chua, V. Kueller, N. Lobo, J. Stellmach, A. Knauer, H. Rodriguez, S. Einfeldt, Z. Yang, N. M. Johnson, and M. Weyers, "Advances in group III-nitride-based deep UV light-emitting diode technology," *Semiconductor Science and Technology*, vol. 26, no. 1, p. 014036, dec 2010. [Online]. Available: https://doi.org/10.1088%2F0268-1242%2F26%2F1%2F014036

[3] K. Ban, J. ichi Yamamoto, K. Takeda, K. Ide, M. Iwaya, T. Takeuchi, S. Kamiyama, I. Akasaki, and H. Amano, "Internal quantum efficiency of whole-composition-range AlGaN multiquantum wells," *Applied Physics Express*, vol. 4, no. 5, p. 052101, apr 2011. [Online]. Available: https://doi.org/10.1143%2Fapex.4.052101

[4] J. Piprek, R. Farrell, S. DenBaars, and S. Nakamura, "Effects of built-in polarization on InGaN-GaN vertical-cavity surface-emitting lasers," *IEEE Photonics Technology Letters*, vol. 18, no. 1, pp. 7–9, Jan 2006.

[5] U. Strauß, A. Avramescu, T. Lermer, D. Queren, A. Gomez-Iglesias, C. Eichler, J. Müller, G. Brüderl, and S. Lutgen, "Pros and cons of green InGaN laser on c-plane GaN," *physica status solidi (b)*, vol. 248, no. 3, pp. 652–657, 2011. [Online]. Available: https://onlinelibrary.wiley.com/doi/abs/10.1002/pssb.201046299

[6] V. Fiorentini, F. Bernardini, and O. Ambacher, "Evidence for nonlinear macroscopic polarization in III–V nitride alloy heterostructures," *Applied Physics Letters*, vol. 80, no. 7, pp. 1204–1206, 2002. [Online]. Available: https://doi.org/10.1063/1.1448668

[7] M. Crawford, "Chapter one - materials challenges of algan-based uv optoelectronic devices," in *III-Nitride Semiconductor Optoelectronics*, ser. Semiconductors and Semimetals, Z. Mi and C. Jagadish, Eds. Elsevier, 2017, vol. 96, pp. 3 – 44. [Online]. Available: http://www.sciencedirect.com/science/article/pii/S008087841630031X

[8] M. Kneissl, T.-Y. Seong, J. Han, and H. Amano, "The emergence and prospects of deep-ultraviolet light-emitting diode technologies," *Nature Photonics*, vol. 13, p. 233, 03 2019.

[9] T. Onishi, O. Imafuji, K. Nagamatsu, M. Kawaguchi, K. Yamanaka, and S. Takigawa, "Continuous Wave Operation of GaN Vertical Cavity Surface Emitting Lasers at Room

Temperature," *IEEE Journal of Quantum Electronics*, vol. 48, no. 9, pp. 1107–1112, Sep. 2012.

[10] Y. Liu, A. Saniul Haq, K. Mehta, T. Kao, S. Wang, H. Xie, S. Shen, P. Yoder, F. Ponce, T. Detchprohm, and R. Dupuis, "Optically pumped vertical-cavity surface-emitting laser at 374.9 nm with an electrically conducting n-type distributed bragg reflector," *Applied Physics Express*, vol. 9, no. 11, 11 2016.

[11] R. Chen, H. D. Sun, T. Wang, K. N. Hui, and H. W. Choi, "Optically pumped ultraviolet lasing from nitride nanopillars at room temperature," *Applied Physics Letters*, vol. 96, no. 24, p. 241101, 2010. [Online]. Available: https://doi.org/10.1063/1.3449576

[12] L. A. Coldren, S. W. Corzine, and M. L. Mašanović, *Diode Lasers and Integrated Photonic Circuits.* John Wiley & Sons, Ltd, 2012, ch. 1, pp. 1–44. [Online]. Available: https://onlinelibrary.wiley.com/doi/abs/10.1002/9781118148167.ch1

[13] J. Verma, A. Verma, V. Protasenko, S. Islam, and D. Jena, "Chapter 11 - nitride leds based on quantum wells and quantum dots," in *Nitride Semiconductor Light-Emitting Diodes (LEDs)*, J. Huang, H.-C. Kuo, and S.-C. Shen, Eds. Woodhead Publishing, 2014, pp. 368 – 408. [Online]. Available: http://www.sciencedirect.com/science/article/pii/B9780857095077500124

[14] R. Roedel, "Light emitting diodes," in *Encyclopedia of Materials: Science and Technology*, K. J. Buschow, R. W. Cahn, M. C. Flemings, B. Ilschner, E. J. Kramer, S. Mahajan, and P. Veyssière, Eds. Oxford: Elsevier, 2001, pp. 4476 – 4485. [Online]. Available: http://www.sciencedirect.com/science/article/pii/B0080431526007853

[15] S. Thomson, "Time-resolved electroluminescence spectroscopy of a white light emitting diode," 2018.

[16] G. Ghione, *Semiconductor Devices for High-Speed Optoelectronics.* Cambridge University Press, 2009.

[17] A. Bojarska, J. Goss, S. Stanczyk, I. Makarowa, D. Schiavon, R. Czernecki, T. Suski, and P. Perlin, "Role of the electron blocking layer in the graded-index separate confinement heterostructure nitride laser diodes," *Superlattices and Microstructures*, vol. 116, pp. 114 – 121, 2018. [Online]. Available: http://www.sciencedirect.com/science/article/pii/S0749603618302659

[18] C. Sheng Xia, Z. M. Simon Li, and Y. Sheng, "On the importance of AlGaN electron blocking layer design for GaN-based light-emitting diodes," *Applied Physics Letters*, vol. 103, no. 23, p. 233505, 2013. [Online]. Available: https://doi.org/10.1063/1.4839417

[19] L. A. Coldren, S. W. Corzine, and M. L. Mašanović, *Diode Lasers and Integrated Photonic Circuits.* John Wiley & Sons, Ltd, 2012, ch. 2, pp. 1–44. [Online]. Available: https://onlinelibrary.wiley.com/doi/abs/10.1002/9781118148167.ch1

[20] T. Fujii, Y. Gao, R. Sharma, E. L. Hu, S. P. DenBaars, and S. Nakamura, "Increase in the extraction efficiency of GaN-based light-emitting diodes via surface roughening," *Applied Physics Letters*, vol. 84, no. 6, pp. 855–857, 2004. [Online]. Available: https://doi.org/10.1063/1.1645992

[21] L. Li, T. Zhai, H. Zeng, X. Fang, Y. Bando, and D. Golberg, “Polystyrene sphere-assisted one-dimensional nanostructure arrays: synthesis and applications,” *J. Mater. Chem.*, vol. 21, pp. 40–56, 2011. [Online]. Available: http://dx.doi.org/10.1039/C0JM02230F

[22] R. Michalzik, “Vcsel fundamentals,” *VCSELs, Springer Series in Optical Sciences, Volume 166. ISBN 978-3-642-24985-3. Springer-Verlag Berlin Heidelberg, 2013, p. 19*, vol. 166, pp. 19–, 10 2013.

[23] S. W. Corzine, R. H. Yan, and L. A. Coldren, “A tanh substitution technique for the analysis of abrupt and graded interface multilayer dielectric stacks,” *IEEE Journal of Quantum Electronics*, vol. 27, no. 9, pp. 2086–2090, Sep. 1991.

[24] S. W. Corzine, R. S. Geels, J. W. Scott, R. . Yan, and L. A. Coldren, “Design of fabry-perot surface-emitting lasers with a periodic gain structure,” *IEEE Journal of Quantum Electronics*, vol. 25, no. 6, pp. 1513–1524, June 1989.

[25] A. Tibaldi, F. Bertazzi, M. Goano, R. Michalzik, and P. Debernardi, “Venus: A vertical-cavity surface-emitting laser electro-opto-thermal numerical simulator,” *IEEE Journal of Selected Topics in Quantum Electronics*, vol. 25, no. 6, pp. 1–12, Nov 2019.

[26] F. Jasim, K. Omar, and Z. Hassan, “Temperature effect on VCSEL output performance,” *Optoelectronics and Advanced Materials, Rapid Communications*, vol. 3, no. 11, pp. 1136–1138, 2009, cited By 3. [Online]. Available: https://www.scopus.com/inward/record.uri?eid=2-s2.0-77951985246&partnerID=40&md5=b4c7170d8926b58ab25cb4b5d80b2492

[27] M. Kuramoto, S. Kobayashi, T. Akagi, K. Tazawa, K. Tanaka, T. Saito, and T. Takeuchi, “High-Power GaN-Based Vertical-Cavity Surface-Emitting Lasers with AlInN/GaN Distributed Bragg Reflectors,” *Applied Sciences*, vol. 9, no. 3, 2019. [Online]. Available: https://www.mdpi.com/2076-3417/9/3/416

[28] S. Mishkat-Ul-Masabih, J. Leonard, D. Cohen, S. Nakamura, and D. Feezell, “Techniques to reduce thermal resistance in flip-chip GaN-based VCSELs,” *physica status solidi (a)*, vol. 214, no. 8, p. 1600819, 2017. [Online]. Available: https://onlinelibrary.wiley.com/doi/abs/10.1002/pssa.201600819

[29] N. Lobo Ploch, H. Rodriguez, C. Stolmacker, M. Hoppe, M. Lapeyrade, J. Stellmach, F. Mehnke, T. Wernicke, A. Knauer, V. Kueller, M. Weyers, S. Einfeldt, and M. Kneissl, “Effective thermal management in ultraviolet light-emitting diodes with micro-led arrays,” *IEEE Transactions on Electron Devices*, vol. 60, no. 2, pp. 782–786, Feb 2013.

[30] A. Chitnis, V. Adivarahan, J. P. Zhang, S. Wu, J. Sun, R. Pachipulusu, V. Mandavilli, M. Gaevski, M. Shatalov, and M. Asif Khan, “High DC power 325 nm emission deep UV LEDs over sapphire,” *Electronics Letters*, vol. 38, no. 25, pp. 1709–1711, Dec 2002.

[31] T. Honda, T. Kobayashi, S. Egawa, M. Sawada, K. Sugimoto, and T. Baba, “Thermal effects on light-emission properties of gan leds grown by metal-organic vapor phase epitaxy,” *Journal of Crystal Growth*, vol. 300, no. 1, pp. 90 – 93, 2007, first International Symposium on Growth of Nitrides. [Online]. Available: http://www.sciencedirect.com/science/article/pii/S0022024806011961

[32] A. Shikanai, T. Azuhata, T. Sota, S. Chichibu, A. Kuramata, K. Horino, and S. Nakamura, “Biaxial strain dependence of exciton resonance energies in wurtzite

gan," *Journal of Applied Physics*, vol. 81, no. 1, pp. 417–424, 1997. [Online]. Available: https://doi.org/10.1063/1.364074

[33] A. Yasan, R. McClintock, K. Mayes, D. Shiell, L. Gautero, S. R. Darvish, P. Kung, and M. Razeghi, "4.5 mW operation of AlGaN-based 267 nm deep-ultraviolet light-emitting diodes," *Applied Physics Letters*, vol. 83, no. 23, pp. 4701–4703, 2003. [Online]. Available: https://doi.org/10.1063/1.1633019

[34] M. Osinski and W. Nakwaski, "Effective thermal conductivity analysis of 1.55 $\mu$m InGaAsP/InP vertical-cavity top-surface-emitting microlasers," *Electronics Letters*, vol. 29, no. 11, pp. 1015–1016, May 1993.

[35] D. L. Boiko, G. Guerrero, and E. Kapon, "Thermoelectrical model for vertical cavity surface emitting lasers and arrays," *Journal of Applied Physics*, vol. 100, no. 10, p. 103102, 2006. [Online]. Available: https://doi.org/10.1063/1.2386941

[36] C. A. Forman, S. Lee, E. C. Young, J. A. Kearns, D. A. Cohen, J. T. Leonard, T. Margalith, S. P. DenBaars, and S. Nakamura, "Continuous-wave operation of m-plane GaN-based vertical-cavity surface-emitting lasers with a tunnel junction intracavity contact," *Applied Physics Letters*, vol. 112, no. 11, p. 111106, 2018. [Online]. Available: https://doi.org/10.1063/1.5007746

[37] S. Adachi, "Lattice thermal conductivity of group-IV and III–V semiconductor alloys," *Journal of Applied Physics*, vol. 102, no. 6, p. 063502, 2007. [Online]. Available: https://doi.org/10.1063/1.2779259

[38] J. C. Lambropoulos, M. R. Jolly, C. A. Amsden, S. E. Gilman, M. J. Sinicropi, D. Diakomihalis, and S. D. Jacobs, "Thermal conductivity of dielectric thin films," *Journal of Applied Physics*, vol. 66, no. 9, pp. 4230–4242, 1989. [Online]. Available: https://doi.org/10.1063/1.343963

[39] M. Grilli, D. Ristau, M. Dieckmann, and U. Willamowski, "Thermal conductivity of e-beam coatings," *Applied Physics A*, vol. 71, no. 1, pp. 71–76, Jul 2000. [Online]. Available: https://doi.org/10.1007/PL00021094

[40] S. Lee, D. Cahill, and T. Allen, "Thermal conductivity of sputtered oxide films," *Physical Review B*, vol. 52, no. 1, pp. 253–257, 1 1995.

[41] T. Detchprohm, Y.-S. Liu, K. Mehta, S. Wang, H. Xie, T.-T. Kao, S.-C. Shen, P. Yoder, F. Ponce, and R. Dupuis, "Sub 250 nm deep-UV AlGaN/AlN distributed Bragg reflectors," *Applied Physics Letters*, vol. 110, no. 1, 2017, cited By 9. [Online]. Available: https://www.scopus.com/inward/record.uri?eid=2-s2.0-85008712533&doi=10.1063%2f1.4973581&partnerID=40&md5=918249d2717e640fee43d65f35db55f4

[42] Y. Mei, R.-B. Xu, H. Xu, L.-Y. Ying, Z.-W. Zheng, B.-P. Zhang, M. Li, and J. Zhang, "A comparative study of thermal characteristics of GaN-based VCSELs with three different typical structures," *Semiconductor Science and Technology*, vol. 33, no. 1, 2018, cited By 2. [Online]. Available: https://www.scopus.com/inward/record.uri?eid=2-s2.0-85038619669&doi=10.1088%2f1361-6641%2faa90aa&partnerID=40&md5=f023125f49cbefc375a60499eaea68c7

[43] A. Franke, M. Hoffmann, R. Kirste, M. Bobea, J. Tweedie, F. Kaess, M. Gerhold, R. Collazo, and Z. Sitar, “High reflectivity III-nitride UV-C distributed Bragg reflectors for vertical cavity emitting lasers,” *Journal of Applied Physics*, vol. 120, no. 13, 2016, cited By 5. [Online]. Available: https://www.scopus.com/inward/record.uri?eid=2-s2.0-84990242744&doi=10.1063%2f1.4963831&partnerID=40&md5=f9d19980a22faac787822d286832e90d

[44] E. Wörner, C. Wild, W. Müller-Sebert, R. Locher, and P. Koidl, “Thermal conductivity of cvd diamond films: high-precision, temperature-resolved measurements,” *Diamond and Related Materials*, vol. 5, no. 6, pp. 688 – 692, 1996, proceedings of the 6th European Conference on Diamond, Diamond-like and Related Materials Part 2. [Online]. Available: http://www.sciencedirect.com/science/article/pii/0925963595003908

[45] R. Delmdahl, M. Kunzer, and U. Schwarz, “Thin film LEDs gaining ground,” *Laser Technik Journal*, vol. 8, no. 3, pp. 48–52, 2011. [Online]. Available: https://onlinelibrary.wiley.com/doi/abs/10.1002/latj.201190027

[46] S. Hwang, D. Morgan, A. Kesler, M. Lachab, B. Zhang, A. Heidari, H. Nazir, I. Ahmad, J. Dion, Q. Fareed, V. Adivarahan, M. Islam, and A. Khan, “276 nm substrate-free flip-chip AlGaN light-emitting diodes,” *Applied Physics Express*, vol. 4, no. 3, p. 032102, feb 2011. [Online]. Available: https://doi.org/10.1143%2Fapex.4.032102

[47] E. Hashemi, J. Bengtsson, J. Gustavsson, M. Stattin, G. Cosendey, N. Grandjean, and Å. Haglund, “Analysis of structurally sensitive loss in gan-based vcsel cavities and its effect on modal discrimination,” *Opt. Express*, vol. 22, no. 1, pp. 411–426, Jan 2014. [Online]. Available: http://www.opticsexpress.org/abstract.cfm?URI=oe-22-1-411

[48] E. Hashemi, J. Bengtsson, J. Gustavsson, M. Calciati, M. Goano, and Å. Haglund, “Thermal lensing effects on lateral leakage in GaN-based vertical-cavity surface-emitting laser cavities,” *Opt. Express*, vol. 25, no. 9, pp. 9556–9568, May 2017. [Online]. Available: http://www.opticsexpress.org/abstract.cfm?URI=oe-25-9-9556

[49] M. Kuramoto, S. Kobayashi, T. Akagi, K. Tazawa, K. Tanaka, T. Saito, and T. Takeuchi, “High-output-power and high-temperature operation of blue GaN-based vertical-cavity surface-emitting laser,” *Applied Physics Express*, vol. 11, no. 11, p. 112101, oct 2018. [Online]. Available: https://doi.org/10.7567%2Fapex.11.112101

[50] M. Kuramoto, S. Kobayashi, T. Akagi, K. Tazawa, K. Tanaka, K. Nakata, and T. Saito, “Watt-class blue vertical-cavity surface-emitting laser arrays,” *Applied Physics Express*, vol. 12, no. 9, p. 091004, aug 2019. [Online]. Available: https://doi.org/10.7567%2F1882-0786%2Fab3aa6

[51] D. E. Gray, *American Institute of Physics Handbook.* McGraw-Hill Book Company Inc., 1982.

[52] E. A. Scott, J. T. Gaskins, S. W. King, and P. E. Hopkins, “Thermal conductivity and thermal boundary resistance of atomic layer deposited high-k dielectric aluminum oxide, hafnium oxide, and titanium oxide thin films on silicon,” *APL Materials*, vol. 6, no. 5, p. 058302, 2018. [Online]. Available: https://doi.org/10.1063/1.5021044

[53] Z. Wu, P. Kuo, W. Lanhua, S. Gu, and R. Thomas, “Photothermal characterization of optical thin films,” *Thin Solid Films*, vol. 236, no. 1, pp. 191 – 198, 1993. [Online]. Available: http://www.sciencedirect.com/science/article/pii/004060909390668F

[54] J. T. Gaskins, P. E. Hopkins, D. R. Merrill, S. R. Bauers, E. Hadland, D. C. Johnson, D. Koh, J. H. Yum, S. Banerjee, B. J. Nordell, M. M. Paquette, A. N. Caruso, W. A. Lanford, P. Henry, L. Ross, H. Li, L. Li, M. French, A. M. Rudolph, and S. W. King, “Review—investigation and review of the thermal, mechanical, electrical, optical, and structural properties of atomic layer deposited high-k dielectrics: Beryllium oxide, aluminum oxide, hafnium oxide, and aluminum nitride,” *ECS Journal of Solid State Science and Technology*, vol. 6, no. 10, pp. N189–N208, 2017. [Online]. Available: http://jss.ecsdl.org/content/6/10/N189.abstract

[55] C. Ramana, M. Noor-A-Alam, J. Gengler, and J. G Jones, “Growth, structure, and thermal conductivity of yttria-stabilized hafnia thin films,” *ACS applied materials & interfaces*, vol. 4, pp. 200–4, 12 2011.

[56] M. A. Panzer, M. Shandalov, J. Rowlette, Y. Oshima, Y. Wei Chen, P. C. McIntyre, and K. Goodson, “Thermal properties of ultrathin hafnium oxide gate dielectric films,” *Electron Device Letters, IEEE*, vol. 30, pp. 1269 – 1271, 01 2010.

[57] W. Liu and A. A. Balandin, “Temperature dependence of thermal conductivity of $\mathrm{al}_x\mathrm{ga}_{1-x}\mathrm{n}$ thin films measured by the differential $3\omega$ technique,” *Applied Physics Letters*, vol. 85, no. 22, pp. 5230–5232, 2004. [Online]. Available: https://doi.org/10.1063/1.1829168

[58] W. Liu and A. A. Balandin, “Thermal conduction in $\mathrm{Al}_x\mathrm{Ga}_{1-x}\mathrm{N}$ alloys and thin films,” *Journal of Applied Physics*, vol. 97, no. 7, p. 073710, 2005. [Online]. Available: https://doi.org/10.1063/1.1868876

[59] A. Sztein, J. Haberstroh, J. E. Bowers, S. P. DenBaars, and S. Nakamura, “Calculated thermoelectric properties of $\mathrm{In}_x\mathrm{Ga}_{1-x}\mathrm{N}$, $\mathrm{In}_x\mathrm{Al}_{1-x}\mathrm{N}$, and $\mathrm{Al}_x\mathrm{Ga}_{1-x}\mathrm{N}$,” *Journal of Applied Physics*, vol. 113, no. 18, p. 183707, 2013. [Online]. Available: https://doi.org/10.1063/1.4804174

[60] Y. R. Koh, M. Shirazi-HD, B. Vermeersch, A. M. S. Mohammed, J. Shao, G. Pernot, J.-H. Bahk, M. J. Manfra, and A. Shakouri, “Quasi-ballistic thermal transport in $\mathrm{Al}_{0.1}\mathrm{Ga}_{0.9}\mathrm{N}$ thin film semiconductors,” *Applied Physics Letters*, vol. 109, no. 24, p. 243107, 2016. [Online]. Available: https://doi.org/10.1063/1.4972186

[61] B. C. Daly, H. J. Maris, A. V. Nurmikko, M. Kuball, and J. Han, “Optical pump-and-probe measurement of the thermal conductivity of nitride thin films,” *Journal of Applied Physics*, vol. 92, no. 7, pp. 3820–3824, 2002. [Online]. Available: https://doi.org/10.1063/1.1505995

[62] M. A. Afromowitz, “Thermal conductivity of $\mathrm{Ga}_{1-x}\mathrm{Al}_x\mathrm{As}$ alloys,” *Journal of Applied Physics*, vol. 44, no. 3, pp. 1292–1294, 1973. [Online]. Available: https://doi.org/10.1063/1.1662342

[63] H. Tong, H. Zhao, V. A. Handara, J. A. Herbsommer, and N. Tansu, “Analysis of Thermoelectric Characteristics of AlGaN and InGaN Semiconductors,” *Proc SPIE*, 02 2009.

[64] G. W. Auner, P.-K. Kuo, Y. S. Lu, and Z. Wu, "Characterization of aluminum nitride thin films grown by plasma source molecular-beam epitaxy," *Proc SPIE*, vol. 2428, pp. 362–369, 02 2009.

[65] R. Rounds, B. Sarkar, A. Klump, C. Hartmann, T. Nagashima, R. Kirste, A. Franke, M. Bickermann, Y. Kumagai, Z. Sitar, and R. Collazo, "Thermal conductivity of single-crystalline AlN," *Applied Physics Express*, vol. 11, no. 7, p. 071001, jun 2018. [Online]. Available: https://doi.org/10.%2Fapex.11.071001

[66] S. R. Choi, D. Kim, S.-H. Choa, S.-H. Lee, and J.-K. Kim, "Thermal Conductivity of AlN and SiC Thin Films," *International Journal of Thermophysics*, vol. 27, no. 3, pp. 896–905, May 2006. [Online]. Available: https://doi.org/10.1007/s10765-006-0062-1

[67] V. Moraes, H. Riedl, R. Rachbauer, S. Kolozsvári, M. Ikeda, L. Prochaska, S. Paschen, and P. H. Mayrhofer, "Thermal conductivity and mechanical properties of AlN-based thin films," *Journal of Applied Physics*, vol. 119, no. 22, p. 225304, 2016. [Online]. Available: https://doi.org/10.1063/1.4953358

[68] Y. Zhao, C. Zhu, S. Wang, J. Z. Tian, D. J. Yang, C. K. Chen, H. Cheng, and P. Hing, "Pulsed photothermal reflectance measurement of the thermal conductivity of sputtered aluminum nitride thin films," *Journal of Applied Physics*, vol. 96, no. 8, pp. 4563–4568, 2004. [Online]. Available: https://doi.org/10.1063/1.1785850

[69] M. Bogner, A. Hofer, G. Benstetter, H. Gruber, and R. Y. Fu, "Differential $3\omega$ method for measuring thermal conductivity of AlN and $Si_3N_4$ thin films," *Thin Solid Films*, vol. 591, pp. 267 – 270, 2015, selected papers from 16th International Conference on Thin Films, October 13-16, 2014, Dubrovnik, Croatia. [Online]. Available: http://www.sciencedirect.com/science/article/pii/S0040609015002461

[70] R. Kato, A. Maesono, and R. P. Tye, "Thermal Conductivity Measurement of Submicron-Thick Films Deposited on Substrates by Modified ac Calorimetry (Laser-Heating Ångstrom Method)," *International Journal of Thermophysics*, vol. 22, no. 2, pp. 617–629, Mar 2001. [Online]. Available: https://doi.org/10.1023/A:1010745603645

[71] U. Tisch, B. Meyler, O. Katz, E. Finkman, and J. Salzman, "Dependence of the refractive index of $Al_xGa_{1-x}N$ on temperature and composition at elevated temperatures," *Journal of Applied Physics*, vol. 89, no. 5, pp. 2676–2685, 2001. [Online]. Available: https://doi.org/10.1063/1.1341212